Part III.

Interdepartmental research activities – selected highlights

Fundamentals of sustainable hydrogen-based metallurgy

Y. Ma[1], I.R. Souza Filho[1], D. Vogel[2], M. Rohwerder[2], D. Ponge[1], H. Springer[1,3], S. Zaefferer[1], S. Nandy[1], S.-P. Tsai[1], M. Todorova[4], A. Kwiatkowski da Silva[1], S. Zhang[5], J.R. Mianroodia[1], B. Svendsen[3], Y. Bai[1], X. Zhou[1], C. Scheu[5], D. Raabe[1]

[1]MA, [2]GO, [3]RWTH Aachen, [4]CM, [5]NG

The massive CO_2 emissions associated with modern iron- and steelmaking have become one of the largest environmental burdens of our generation, and the international steel market is forecast to grow by at least 30–35 % during the next 30 years [1, 2]. Therefore, the institute conducts interdisciplinary and multiscale research on the physical and chemical foundations for improving the sustainability of steels, with a focus on reduced CO_2-intense production and low-energy synthesis. These goals can in principle be reached by combining several types of iron carriers, such as oxidic fines, lump ore, or scrap, with a variety of carbon-free reduction media, such as hydrogen or ammonia, in different types of furnaces.

The interplay of multiple mechanisms and influencing factors both, from the reactive metallurgy side and from the advanced processing side, requires the cooperation of several departments on this topic. This includes the design and operation of fully instrumented reactor set-ups in which the different feedstock materials can be charged, while the underlying redox reactions can be monitored through the spectroscopy of the intermediate and final reaction products.

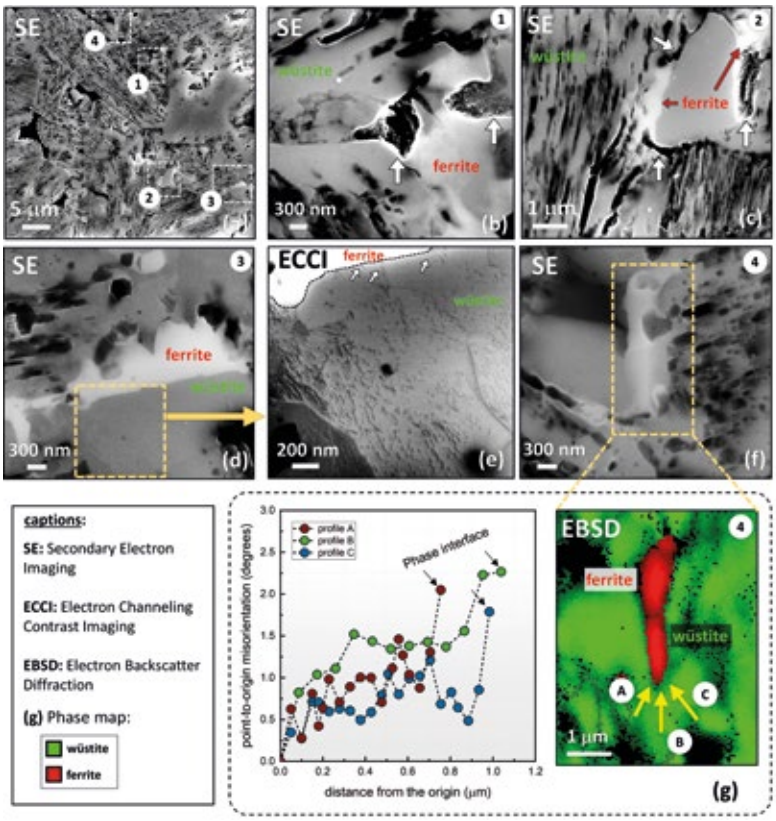

Fig. 1: *Correlative SE and ECCI analysis of a partially reduced pellet (10 min, 700 °C). (a) SE image of the map of the pellet microstructure. The white frames marked as 1, 2, and 3 highlight specific regions whose enlarged views are given in (b), (c), and (d), respectively. (e) ECCI image obtained from the area delimited by the yellow frame in (d). (f) SE image from the area labelled as 4 in (a). The arrows A, B, and C were used as a reference to obtain local orientation gradients. (g) EBSD phase map from the marked area. Point-to-origin local misorientation profiles along arrows A, B, and C in (f).*

The specific focus of this cross-departmental initiative is currently placed on hydrogen-based direct reduction [3] and hydrogen-based plasma smelting reduction of iron ores [4]. As raw materials, commercial pellets and ore fines are used, as well as well-defined oxide single crystals. The hydrogen-based direct reduction of iron oxides is a solid-gas reaction. The kinetics of this process is not well understood, particularly during the wüstite reduction step, which is nearly an order of magnitude slower than the hematite reduction.

The rate-limiting factors of this reaction are investigated and related to the microstructure and local chemistry of the ores, using a multiscale structure and composition analysis of iron reduced from hematite with pure molecular hydrogen reaching down to near-atomic scale [3]. During reduction, a complex pore- and microstructure evolves, due to oxygen loss and several non-volume-conserving phase transformations. The microstructure after reduction is an aggregate of nearly pure iron crystals, containing inherited and acquired pores and cracks (Fig. 1). We observe several types of lattice defects that accelerate mass transport as well as several chemical impurities (Na, Mg, Ti, V) within the Fe in the form of oxide islands that were not reduced.

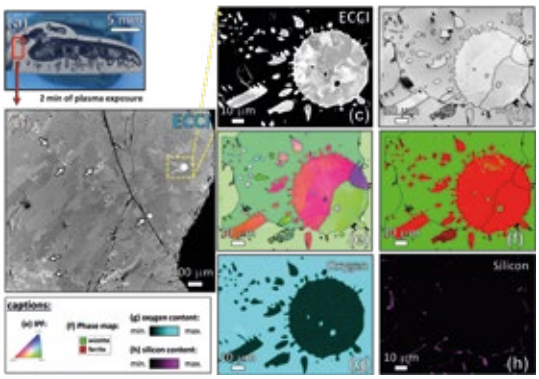

Fig. 2: *Microstructural characterization of a sample partially reduced for 2 min by hydrogen plasma. (a) Overview of the sample. The red frame shows the chosen area for the correlative EBSD-ECCI probing approach. (b) ECCI-image of the area delimited by the red frame in (a). The white arrows evidence the presence of small domains of iron. (c) ECCI-image showing an enlarged view of the region delimitated by the yellow frame in (a). The corresponding EBSD maps of the area displayed in (c) are as follows: (d) image quality (IQ) map; (e) inverse pole figure (IPF) map in which the crystallographic orientations are shown perpendicular to the normal direction of the sample, i.e. parallel to the solidification direction; (f) phase map where wüstite and ferrite are represented by green and red respectively; (g) oxygen distribution and (h) silicon distribution maps.*

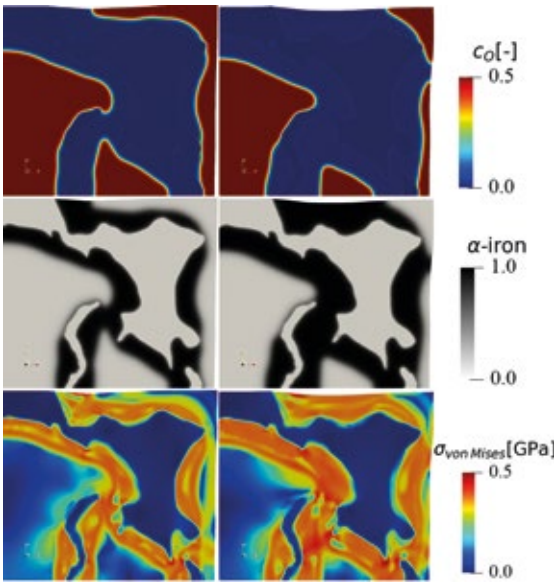

Fig. 3: *Results from the chemo-mechanically coupled phase-field simulations with an elasto-plastic material response for the case of wüstite reduction for 700 °C under hydrogen exposure as a function of reduction time. The images show contour plots of the oxygen concentration, the BCC iron phase order parameter, and the von Mises stress.*

Hydrogen-based plasma smelting reduction offers an attractive alternative to green steel production. Therefore, the basic mechanisms behind the reduction of hematite using hydrogen plasma are studied [4]. The reduction kinetics depends on the balance between the input mass and the arc power. For an optimized input mass-arc power ratio, the complete reduction was obtained within 15 min of exposure to the hydrogen plasma. In such a process, wüstite reduction is again the rate-limiting step. Nevertheless, its rates are comparable with those found in hydrogen-based direct reduction. The possible advantage of the reduction of ores through a reductant plasma in an electric arc lies in the fact that reduction and liquification are done in a single process step.

Micro- and nanoscale chemical and microstructure analysis revealed that the gangue elements partition to the remaining oxide regions (Fig. 2). Si-enrichment was observed in the interdendritic fayalite domains, at the wüstite/-iron interfaces, and in the primarily solidified oxide particles inside the iron. With proceeding reduction, however, such elements are gradually removed from the samples so that the final iron product is nearly free of gangue impurities. The studies provide microstructural and atomic-scale insights into the composition and phase transformations during hydrogen-based plasma smelting reduction, enabling better understanding of the underlying thermodynamics and kinetic barriers of this process, as a basis for the design of suited furnace concepts for CO_2-free ironmaking.

The hydrogen-based direct reduction of iron oxides is also investigated theoretically. A chemo-mechanically coupled phase-field model is currently under development, to explore the interplay between phase transformation, chemical reaction, component diffusion, elastoplastic deformation, and microstructure during the reduction of wüstite with hydrogen (Fig. 3).

The phase-field simulation is coupled to Gibbs free energy data that are fitted from corresponding thermodynamic databases. The simulation reveals the important role of elastic and plastic deformation during the reduction and allows first insights into the different mass transport pathways along the highly defected microstructure. The model also allows to better understand both, the main decelerating factors (oxide-core-metal-shell structures) and accelerating factors (delamination and fracture at the hetero-interfaces) determining the overall reduction kinetics.

References

1. IEA. Iron and Steel Technology: Towards More Sustainable Steelmaking (International Energy Agency, 2020).
2. Pei, M.; Petäjäniemi, M.; Regnell, A.; Wijk, O.: Metals 10 (2020) 972.
3. Kim, S.H.; Zhang, X.; Ma, Y.; Souza Filho, I.R.; Schweinar, K.; Angenendt, K.; Vogel, D.; Stephenson, L.T.; El-Zoka, A.A.; Mianroodi, J.R.; Rohwerder, M.; Gault, B.; Raabe, D.: Acta Mater. 212 (2021) 116933.
4. Souza Filho, I.R.; Ma, Y.; Kulse, M.; Ponge, D.; Gault, B.; Springer, H.; Raabe, D.: Acta Mater. 213 (2021) 116971.

Materials for electrocatalysis

C. Scheu[1], S. Zhang[1], R. Aymerich Armengol[1], J. Lim[1], A. Garzón Manjón[1], B. Gault[2], S.-H. Kim[2], A.A. El-Zoka[2], K. Schweinar[2], J. Neugebauer[4], O. Kasian[3], M. Rabe[3], K. Tschulik[5], M. Todorova[4]

[1]NG, [2]MA, [3]GO, [4]CM, [5]RUB

The world's transition to a more sustainable future requires innovative solutions for energy conversion and storage. Strategies to develop stable, active and durable catalytic materials are an essential part of this development. The continued and concerted effort of different groups at the MPIE to enhance our understanding of the fundamental processes governing the stability, activity and degradation of, e.g., electrolysers in realistic environments and under operando conditions, opens new routes towards designing efficient and long-lived catalysts. Three main directions were pursued within the last years: (i) exploiting metal dealloying to enhance catalytic activity, (ii) understanding the role of dopants, impurities and local inhomogeneities on catalytic activity and (iii) the study of oxides and oxidised compounds, which exhibit an enhanced stability in the conventionally harsh environments developing during catalytic reactions. In all of these, particular attention is paid to resolve the atomistic structure, as the gained insights have proven highly beneficial in explaining catalytic performance.

Our work demonstrated that electrochemical dealloying can greatly improve the catalytic activity of AgAu nanoparticles for the hydrogen evolution reaction [1]. By combining electrochemistry with identical location electron microscopy analyses and linking them to the electrocatalytic properties of the obtained nanocatalysts, they established guidelines for the selection of dealloying parameters to reach highly porous and active materials beyond the previous "trial and error" attempts. Using AgAu alloy nanoparticles and the hydrogen evolution reaction as a model system, the influence of cyclic voltammetry parameters on the catalytic activity upon electrochemical dealloying was investigated. Increasing cycle numbers initially result in a decreased Ag content and a sharp improvement in catalyst activity. Additional dealloying increased the nanoparticle porosity, while marginally altering their composition, due to surface motion of atoms. Since this is accompanied by particle aggregation, further cycling results in a decrease of catalytic activity. This transition between porosity formation and particle aggregation marks the optimum for nanocatalyst post-production. The gained insights will allow speeding up the development of new materials by electrochemical dealloying as an easy-to-control post-processing route to tune properties of existing nanoparticles, instead of having to alter usually delicate synthesis routes as a whole.

Chemical synthesis is a conventional route by which catalytic materials are produced and/or designed. Wet-chemical methods are however, more complex than expected and often reported. Careful analysis of samples we studied in the context of electrocatalysis, revealed the presence of impurities integrated within the structure during synthesis. The presence of traces of such spurious elements may enhance or detrimentally affect the properties of materials and thus, affect their performance. Identification and quantification of such impurities is however extremely challenging. To better tackle these issues, (scanning) transmission electron microscopy ((S)TEM), atom probe tomography (APT) and X-ray photoelectron spectroscopy (XPS) were combined to carefully analyse the structural features and chemical composition of MoS_2 sheets [2]. The obtained results showed that impurity elements from the precursor were incorporated into the nanosheets during synthesis, pointing towards the necessity to carefully control the synthesis environment to avoid contamination. These findings also suggest a strategy to optimize materials performance, which we now exploit for targeted materials design (see p. 198). One example is the intentional synthesis of Pd nanoparticles with different levels of B doping [3]. Analysis by STEM and APT, complemented by density functional theory calculations and cyclic voltammogram measurements, enable us to assess changes in the catalytic activity of the nanoparticles towards the hydrogen evolution and/or hydrogen oxidation reactions (HER, HOR) due to the presence of impurities, and their effect on the grain boundary cohesion and hence, material service lifetime.

Another example focuses on the role of Sn in enhancing the efficiency of hematite (α-Fe_2O_3) for water splitting [4]. Looking both at advantages and limitation of Sn-doping of hematite thin films photoanodes, the study reveals that Sn ions at the surface eliminate surface states, preventing hole trapping and thus, enhancing the catalytic activity towards the oxygen evolution reaction (OER) on the (0001) hematite surface. An aberration corrected STEM image, the corresponding elemental distribution obtained by electron energy loss spectroscopy (EELS) and APT of a sample where Sn is located only within the top few nanometre of the hematite film is given in Fig. 1. On the other hand, the homogeneous distribution of Sn throughout the thickness of a hematite film impairs crystallization, due to grain boundary segregation of Sn, leading to inferior performance.

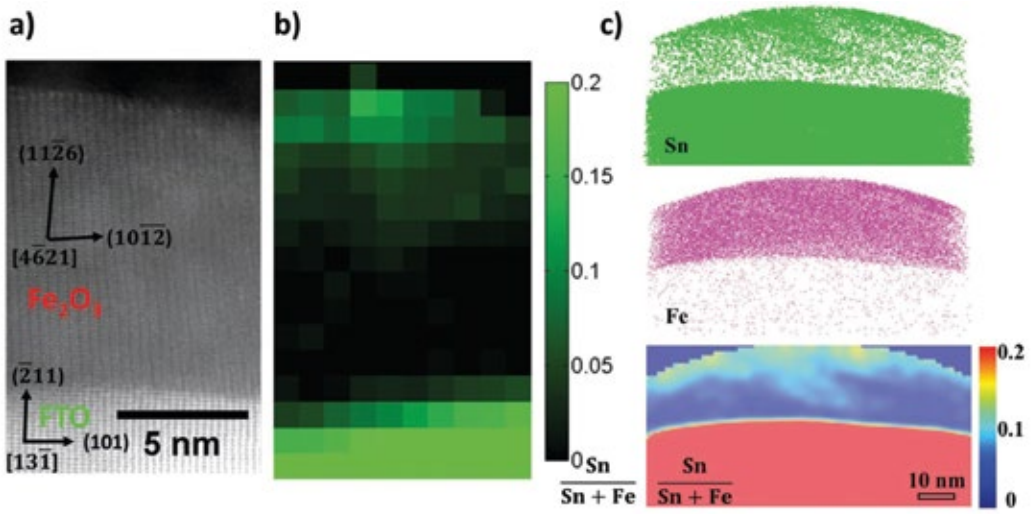

Fig. 1: *a) Atomic column resolved STEM image of a thin hematite film where Sn dopants are located only at the top surface and few nanometres below. b) EELS elemental map resembling the distribution of the Sn. c) APT reconstruction of the same sample showing the Sn and Fe distribution in 3D. Figure taken from [4].*

Next to high chemical activity towards a targeted catalytic reaction, the development of a sustainable energy economy requires longevity of the used catalytic materials. The latter is a particular obstacle, given the harsh electrochemical environments developing during reactions. Oxides show an enhanced stability in such conditions and may therefore, provide blue-prints for achieving long-term stability of catalytic materials. With this in mind, several of our studies focused on different aspects of the oxides using Ir and Ru, aiming to understand the connection between structure, stability and catalytic activity. These studies reveal the role of lattice oxygen atoms in rutile IrO_2 with respect to stability, surface hydrogenation and amorphization, and catalytic activity through a direct visualisation of the electrochemically active body of the catalyst [5, 6]. They also show that the local microstructure controls the growth rate of individual oxide grains and how crystalline defects act as diffusion pathways during oxidation in different $Ir_xRu_yO_2$ [7]. Other studies specifically target the effect different electrolytes have on the degradation, as exemplified by the example of the dissolution behaviour of the $BiVO_4$ photoanode [8]. Ongoing studies deal with $Fe_xMn_{1-x}O_2$ as electrocatalyst. With the help of Raman spectroscopy and TEM, the effect of the crystal structure as well as the morphology (nanosheets, nanocones and nanotubes) on the (photo) electrochemical performance are explored. Focus is placed on the stability of the nanostructures upon electrochemical cycling, which we will explore by identical location TEM experiments (IL-TEM).

References

1. Rurainsky, C.; Garzón Manjón, A.; Hiege, F; Chen, Y.-T.; Scheu, C.; Tschulik, K.: J. Mater. Chem. A 8 (2020) 19405.
2. Kim, S.-H.; Lim, J.; R. Sahu, Kasian, O.; Stephenson, L.T.; Scheu, C.; Gault, B.: Adv. Mater. 32 (2020) 1907235.
3. Kim, S.-H.; Yoo, S.-Y.; El-Zoka, A.A.; Lim, J.; Jeong, J.; Schweinar, K.; Kasian, O.; Stephenson, L.T.; Scheu, C.; Neugebauer, J.; Todorova, M.; Gault, B.: in preparation.
4. Hufnagel, A.G.; Hajiyani, H.; Zhang, S.; Li, T.; Kasian, O.; Gault, B.; Breitbach, B.; Bein, T.; Fattakhova-Rohlfing, D.; Scheu, C.; Pentcheva, R.: Adv. Funct. Mater. 28 (2018) 1804472.
5. Schweinar, K.; Gault, B.; Mouton, I.; Kasian, O.: J. Phys. Chem. Lett. 11 (2020), 5008.
6. Kasian, O.; Geiger, S.; Li, T.; Grote, J.-P.; Schweinar, K.; Zhang, S.; Scheu, C.; Raabe, D.; Cherevko, S.; Gault, B.; Mayrhofer, K.J.J.: Energy Environ. Sci. 12 (2019) 3548.
7. Schweinar, K.; Nicholls, R.L.; Rajamathi, C.R.; Zeller, P.; Amati, M.; Gregoratti, L.; Raabe, D.; Greiner, M.; Gault, B.; Kasian, O.: J. Mater. Chem. A. 8 (2020) 388.
8. Zhang, S.; Ahmet, I.; Kim, S.-H.; Kasian, O.; Mingers, A.M.; Schnell, P.; Kölbach, M.; Lim, J.; Fischer, A.; Mayrhofer, K.J.J., Cherevko, S.; Gault, B.; van de Krol, R.; Scheu, C.: ACS Appl. Energy Mater 3 (2020), 9523.

Fe–Al - Sustainable alloys for demanding applications

A. Gedsun[1], S. Antonov[2], F. Stein[1], M. Palm[1]

[1]SN, [2]MA

Iron aluminide (Fe–Al) alloys are materials based on the intermetallic phases Fe_3Al and FeAl [1, 2]. Due to their relatively high Al content they form Al_2O_3 scales in oxidising environments. Specifically α-Al_2O_3 scales, which are dense, thin and adherent, are very protective against degradation of Fe–Al in aggressive environments [3, 4]. Also due to their Al content, a passive hydroxide layer forms in humid air, which acts as a lubricant, thereby minimising friction and contributing to the excellent wear behaviour of these alloys.

The high Al content of more than 20 at.% also makes the alloys a light-weight material. The density of Fe-Al alloys is about 5.7–6.7 g/cm^3, i.e. only about 80 % of that of Cr-Ni-steels or about 70 % of Ni-base superalloys. As these are typical candidates that can be possibly replaced by Fe-Al, their substitution has a number of advantages [1, 2]

- For moving parts, e.g. turbine blades, fuel saving can be expected due to the lower weight of Fe–Al.
- Better corrosion and wear resistance of Fe–Al should result in less maintenance and longer lifetime.
- The excellent corrosion resistance may also enable higher operation temperatures, thereby further reducing energy consumption.
- For large industrial facilities, support structures could be much leaner, e.g. if for a steam cracker Fe–Al tubes would be employed.

However, for industries the comparative low price of Fe–Al is of foremost interest. Fe and Al are non-strategic elements, which are actually the two most abundant metals in the earth's crust, and Fe-Al needs comparatively little alloying for fine-tuning the properties. Consequently, there has been a large number of industrial projects within recent years, investigating various processing routes for Fe–Al and for a variety of applications [5]. It has been shown that Fe–Al can be processed on standard equipment, e.g. by induction melting in air, by sand, permanent mould or investment casting, by forging, or even by additive manufacturing [6].

"Process development for economic and efficient turbine parts made of iron aluminides (Fe–Al)" is one of these ongoing MPIE projects with partners from academia and companies of different industry branches. It builds up on previous projects, where Fe–Al–Ta alloys had already been qualified for such applications. The part where the MPIE is involved in the project now aims to elucidate whether Fe–Al–Nb could replace this more costly alloy [7].

Insufficient strength above 500 °C has for long time been an obstacle for a wider application of Fe–Al alloys [1, 2].

Specifically, at the MPIE a number of alloying strategies have been developed, which yielded Fe–Al alloys whose creep resistance matches or even surpasses that of advanced steels and of plain Ni-base alloys at 700 °C. One of these strategies relies on the formation of a metastable Heusler phase. The phase could either act as a strengthening phase by forming a fine-scaled, coherent microstructure with the matrix or through aimed transformation into the stable Laves phase. The basic mechanism of the latter transformation and how it can be influenced by doping, mechanical deformation or heat treatments are understood [8]. However, for a quantitative analysis of the transformation, specifically the chemical composition of the Heusler phase, but also their morphology and distribution within the matrix, have to be quantified. As the metastable precipitates are nanometre-sized, atom probe tomography (APT) is very well suited for their analysis.

APT provides three-dimensional chemical information at the sub-nanometre resolution [9], which allows us to study the formation of these fine $L2_1$ precipitates and their compositional evolution during heat treatments. Site specific samples can be extracted using a focused ion beam (FIB) system to pinpoint exact areas and phases of interest and compare different alloy systems [10].

Fig. 1 compares reconstructions of the $L2_1/DO_3$ microstructure of Fe–25.9Al–1.6Ta (in at.%) to Fe–24.4Al–2Nb–0.03B, showing unprecedented details of the fine rectangular arrays of precipitates that formed during annealing at 700 °C. Though it is known that Heusler phases of the type Fe_2AlX may have extended homogeneity ranges to leaner compositions of X than the stoichiometric 25 at.% X, the current results are quite surprising. When comparing the composition of these small precipitates, it becomes apparent that although the Al content is similar in the Heusler phase in both alloys and close to the stoichiometric value, the precipitates in the Fe–Al–Ta alloy are with about 19 at.% Ta closer to the stoichiometric composition compared to the Nb-lean precipitates, which only contain about 10 at.% Nb.

A time-temperature-transformation (TTT) diagram established from literature data and present work suggests that at a given temperature the metastable Heusler phase transforms more readily to the stable Laves phase in the Fe–Al–Nb system [7]. Before the APT investigations had been performed, it was inferred that the difference is due to the faster diffusion of Nb. The Heusler phase cannot transform directly into the Laves phase, but dissolves first in the Fe–Al matrix before nuclei of the Laves phase preferentially form on the grain boundaries [8].

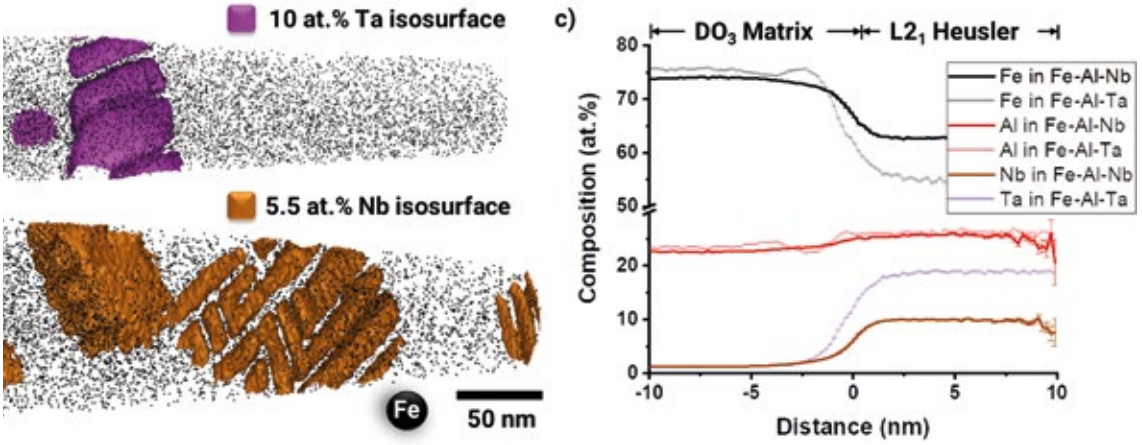

Fig. 1: *3D reconstructions of the a) Fe–Al–Ta alloy and b) Fe–Al–Nb alloy delineating precipitates with the respective isoconcentration surfaces, and c) compositional profiles across the precipitate/matrix interfaces for both alloys.*

The APT measurements now reveal that the difference between the Nb and Ta contents in the Heusler phase and the matrix is much larger in case of the Ta alloy, because the content of Nb or Ta in the Fe–Al matrix is 1.1 at.% in both alloys. Therefore, in addition to the slower diffusion kinetics it should also take more time for equilibrating the Ta-rich Heusler phase. Moreover, the precipitates in the Fe–Al–Ta alloy look more compact than the feathery appearance in the Fe–Al–Nb alloy (Fig. 1a, b). The latter results in a much larger surface area with the matrix, which could also contribute to a quicker dissolution. However, the current investigation gives no indication about coherency stresses between the precipitates and the matrix, which also have a stabilising effect for the metastable precipitates.

Further work will be carried out to gain insight on how the compositions of the Heusler phase vary with aging time and temperature, and what sort of compositional modulations contribute to the refinement of the subsequent Laves phase population. Knowledge on precipitate morphology and composition evolution will allow us to fine-tune the alloy chemistries and processing to achieve superior properties.

References

1. Palm, M.; Stein, F.; Dehm; G.: Annu. Rev. Mater. Res. 49 (2019) 297.
2. Palm, M.; Stein, F: Iron-Based Intermetallics, in Rana, R. (ed.) High-Performance Ferrous Alloys, Springer Nature Switzerland AG, Cham, Switzerland (2021) 423.
3. Peng, J.; Moszner, F.; Rechmann, J.; Vogel, D.; Palm, M.; Rohwerder, M.: Corros. Sci., 149 (2019) 123.
4. Zavašnik, J.; Peng, J.; Palm, M.; Corros. Sci.: 179 (2021) 109170.
5. Moszner, F.; Peng, J.; Suutala, J.; Jasnau, U.; Damani, M.; Palm, M.: Metals, 2019 (2019) 847.
6. Michalcová, A.; Senčekova, L.; Rolink, G.; Weisheit, A.; Pešička, J.; Stobik, M.; Palm, M.: Mater. Design 116 (2017) 481.
7. Gedsun, A.; Stein, F.; Palm, M.: MRS Adv. 6 (2021) 176.
8. Prokopčáková, P.; Švec, M.; Palm, M.: Int. J. Mater. Res.107 (2016) 396.
9. Antonov, S.; Isheim, D.; Seidman, D.; Sun, E.; Helmink, R.; Tin, S.: Superalloys 2016, 13 (2016) 199.
10. Antonov, S.; Isheim, D.; Seidman, D.; Tin, S.: Materialia 7 (2019) 100423.

Improving the performance of thermoelectric materials by microstructure design

T. Luo[1], L. Abdellaoui[2], H. Bishara[3], L. Gomell[1], R. Bueno Villoro[2], S. Zhang[2], C. Scheu[2], B. Gault[1]

[1]MA, [2]NG, [3]SN

Ecological concerns drive the exploration of "green" alternatives to generate electricity. One environmentally-friendly approach is to recycle waste heat by thermoelectric devices to realize the heat-to-electricity conversion. These devices are without moving parts, noise- and carbon-emission free, and can be miniaturized and combined with other energy conversion technologies such as direct solar thermal energy conversion. Their conversion efficiency is defined by a dimensionless figure of merit *ZT*, which relates the electrical conductivity σ, the Seebeck coefficient *S*, the temperature *T,* and the thermal conductivity κ as follows: $ZT = \frac{S^2 \sigma \cdot T}{\kappa}$. Substantial research & industrial efforts are pursued to optimize the thermoelectric performance by doping and isoelectronic alloying, i.e. tuning the alloy's composition. However, the role of microstructure, and the interaction of dopants with lattice imperfections, are rarely considered and studied, which limits the opportunity for science-driven optimization of the material.

We will showcase our approach here with results on Half-Heusler (HH) compounds, with a stoichiometry NbCoSn, that stand out as state-of-the-art thermoelectric materials for medium-to-high temperature applications. We studied Pt-doped NbCoSn as part of a collaboration with C. Felser (Max Planck Institute for Chemical Physics of Solids). Pt substitutes Co, thereby providing an additional electron, making it an effective dopant. Pt-doping leads to significant improvements in the electrical power factor and reduces lattice thermal conductivity, as reported for $NbCo_{1-x}Pt_xSn$ (*x*=0.00-0.15) [5]. Interestingly in this series, the sample with *x*=0.05 (annealed, NbCoSn-Pt-AN) exhibits a striking increase in electrical conductivity compared to *x*=0.06 (non-annealed, NbCoSn-Pt), as shown in Fig. 1(a).

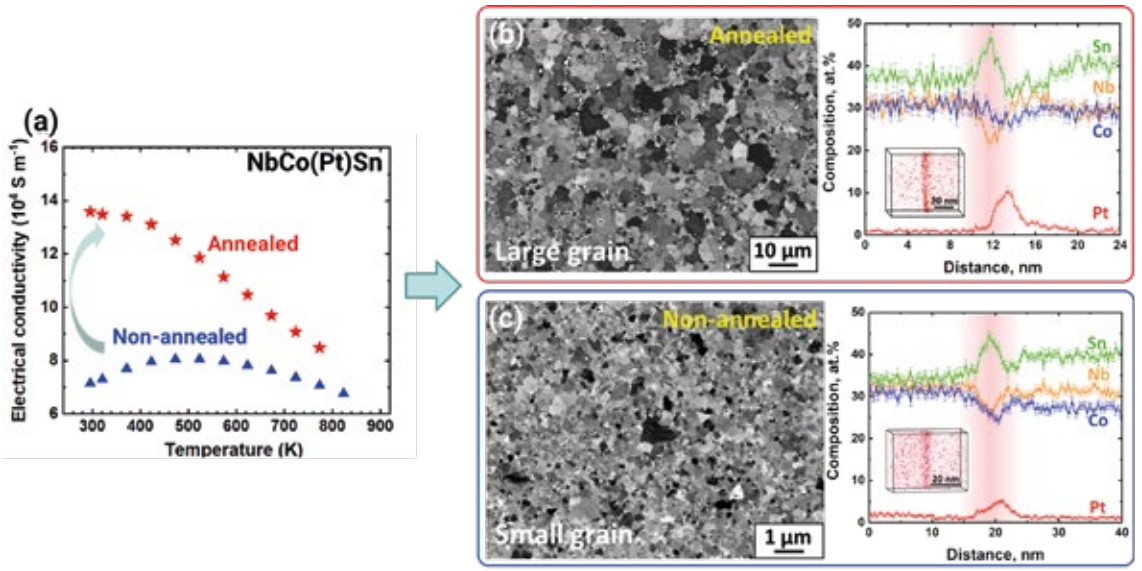

Fig.1: *Electrical conductivity of NbCo(Pt)Sn as a function of temperature: annealed vs. non-annealed sample. Grain size and grain boundary segregation for the (b) annealed and (c) non-annealed sample*

Our interdepartmental activities aim to address this knowledge gap by characterizing the multiscale complexity of the microstructure of a range of thermoelectric materials including half- and full-Heuslers [1, 2], $AgSbTe_2$ [3], and PbTe [4] and correlating it with their thermal and electrical conductivity. This will ultimately enable us to develop thermoelectric materials by microstructure design.

Grain size. The stored deformation energy induced by ball-milling drives grain growth during the post-sintering annealing. It leads to a tenfold increase in grain size (0.23 ± 0.12 µm to 2.38 ± 1.65 µm) and thus a largely reduced grain boundary (GB) area of NbCoSn-Pt-AN, as revealed

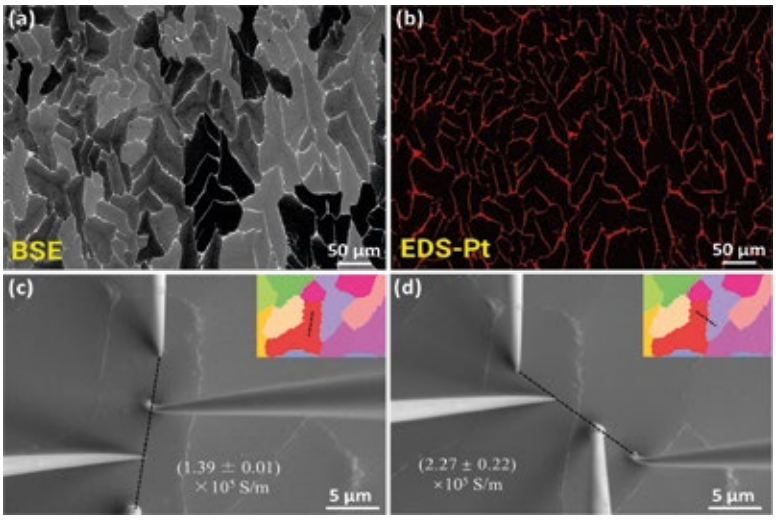

Fig. 2: *(a) Backscattered electron (BSE) image of the NbCo(Pt)Sn sample before ball milling. (b) The corresponding energy-dispersive X-ray spectroscopy (EDX) map of Pt. The white colour in the BSE image is due to the enrichment of Pt at grain boundaries. The position layout of the four needles used for the local measurement (c) within the grain interior, and (d) crossing a high angle grain boundary, which was assessed by electron-backscattered diffraction (inset).*

by backscattered electron imaging in a scanning electron microscope (SEM) (Fig. 1b and c). The difference in grain size between the two samples becomes the first key microstructural factor influencing the electrical conductivity through grain boundary scattering.

Grain boundary segregation. Atom probe tomography shows that the intragranular Pt-content is similar for both alloys, i.e. ~1.35 ± 0.09 at.% for NbCoSn-Pt and 1.27 ± 0.09 at.% for NbCoSn-Pt-AN. The improvement in electrical conductivity does hence not arise from the doping level, rather, from the microstructure evolution. Pt-segregation to GBs is found in both samples Fig.1 (b) and (c), with varying degree of Pt enrichment across different GBs, likely depending on their geometric characteristics.

Local electrical conductivity. To assess the impact of this GBs segregation of Pt on the electrical conductivity, we used an *in situ* four-point-probe technique within an SEM to measure the local electrical conductivity [6]. As the grain size must be sufficiently large to separate the four probes, we selected the NbCoSn-Pt (x=0.05) sample before ball milling with an average grain size of approx. 25 µm. The corresponding backscattered electron micrograph and compositional map from energy-dispersive X-ray spectroscopy for Pt are respectively shown in Fig. 2 (a) and (b), highlighting Pt enrichment and percolation along grain boundaries. The electrical conductivity was measured inside two adjacent grains and across the corresponding high angle grain boundary, as assessed by electron-backscattered diffraction (inset in Fig. 2c and d). One example of the position layout of the four probes is displayed in Fig. 2(c) for grain interior and Fig. 2(d) for a high angle grain boundary. The absolute value of the electrical conductivity is (1.39 ± 0.01) ×10^5 S/m for the grain interior, i.e. comparable with the value of NbCoSn-Pt-AN at room temperature. Across the GB, and despite possible space-charge effects, the conductivity increases almost twofold to (2.27 ± 0.22) ×10^5 S/m thanks to the enrichment of Pt at GBs. We therefore prove the beneficial effect of GB-segregation on the electrical conductivity. It is hence possible to use grain boundary engineering to manipulate the GB-transport properties, opening new possibilities for optimizing TE performance.

Generalization. The philosophy and approach that was discussed here was deployed to analyze several other materials, for instance, PbTe and AgSbTe2 (see p. 13), Ti(Co, Fe)Sb Half-Heusler with the collaboration with G. J. Snyder (Northwestern University, USA), and the Fe2AlV full-Heusler alloy that is being synthesized in-house. For the Fe2AlV, we also investigated the possibilities of using the selective-laser melting machine to manipulate the microstructure by surface-laser remelting [7], which can be seen as a precursor to additive manufacturing. We demonstrated an influence of grain boundary and structural defects on both electrical and thermal conductivities measured locally. We are also exploring the overlooked effect of impurity introduction during processing for instance.

References

1. Gomell, L.; Roscher, M.; Bishara, H.; Jägle, E.A.; Scheu, C.; Gault, B.: Scr. Mater. 193 (2021) 153.
2. Luo, T.; Serrano-Sánchez, F.; Bishara, H.; Zhang, S.; Bueno Villoro, R.; Kuo, J.J.; Felser, C.; Scheu, C.; Snyder, G.J.; Best, J.P.; Dehm, G.; Yu, Y.; Raabe, D.; Fu, C.; Gault, B.: Acta Mater. 217 (2021) 117147.
3. Abdellaoui, L.; Zhang, S.; Zaefferer, S.; Bueno-Villoro, R.; Baranovskiy, A.; Cojocaru-Mirédin, O.; Yu, Y.; Amouyal, Y.; Raabe, D.; Snyder, G.J.; Scheu, C.: Acta Mater. 178 (2019) 135.
4. Abdellaoui, L.; Chen, Z.; Yu, Y.; Luo, T.; Hanus, R.; Schwarz, T.; Bueno Villoro, R.; Cojocaru-Mirédin, O.; Snyder, G.J.; Raabe, D.; Pei, Y.; Scheu, C.; Zhang, S.: Adv. Funct. Mater. (2021) 2101214.
5. Serrano-Sánchez, F.; Luo, T.; Yu, J.; Xie, W.; Le, C.; Auffermann, G.; Weidenkaff, A.; Zhu, T.; Zhao, X.B.; Alonso, J.A.; Gault, B.; Felser, C.; Fu, C.: J. Mater. Chem. A 6 (2020) 4883.
6. Bishara, H.; Ghidelli, M.; Dehm, G.: ACS Appl. Electron. Mater. 2(7) (2020) 2049.
7. Gomell, L.; Haeger, T.; Roscher, M.; Bishara, H.; Heiderhoff, R.; Riedl, T.; Scheu, C.; Gault, B.: arXiv:2107.07327. (2021).

III-V Semiconductors and alloys at the nanoscale: materials design for novel optoelectronic and elastic properties

L. Lymperakis[1], S.-H. Yoo[1], J. Neugebauer[1], T. A. Nugraha[2], E. Scalise[2], S. Wippermann[2], Ch. Liebscher[3], Ch. Kirchlechner[3], G. Dehm[3]

[1]CM, [2]GO, [3]SN

Designing and controlling the nanoscale structure of semiconductors and alloys is a promising strategy in order to create materials with targeted optoelectronic and mechanical properties. In this context, III-V and III-N nanostructures are particularly attractive candidates for surmounting materials-related challenges in applications ranging from optoelectronics, power electronics and hydrogen diffusion barriers to hard and wear resistant coatings.

One possible route to create such nanostructured materials is to use colloidal nano-scale building blocks, e.g., nanocrystals, as "*artificial atoms*" and assemble them into **quantum dot (QD) solids** (Fig. 1). III-V semiconductor-based QDs, consisting of e.g., InP or InGaP nanocrystals, are among the most widely investigated materials systems due to their potentially superior optical properties and lower toxicity, compared to commercially available II-VI QD solids. Nevertheless, III-V systems still suffer from inferior colour purity due to broad emissivity and poor photoluminescence quantum yields. We recently demonstrated [1] that nanocrystal stoichiometry dispersion is a major source of trap states and largely responsible for the observed emission broadening in III-V QD solids. Whereas II-VI QD solids require only nanocrystal size control to achieve narrow emission, it is necessary to realize in addition nanocrystal stoichiometry control in the case of III-V QD solids.

Anomalously strong temperature-induced shifts of the electronic bandgaps are another important source of emission broadening. In order to reveal the origin of these anomalous shifts, we used so-called magic-sized nanoclusters as atomically precise model systems for nanocrystals with zero dispersion in both size and stoichiometry. Tantalizingly, approaches that are commonly employed to accurately predict temperature-dependent bandgaps in bulk materials have been known for more than a decade to yield qualitatively wrong results in the case of nanocrystals. We therefore developed a novel approach that allows us to accurately compute temperature-induced band gap shifts also for nanocrystals, using constrained *ab initio* molecular dynamics (AIMD) simulations on the excited state potential energy surface and atomistic thermodynamics, where the band gap is computed as the Gibbs free energy of exciton formation.
The key innovation of our approach in contrast to existing methods is to take into account the fully anharmonic exciton-phonon coupling [2].

We revealed [2] that the experimentally observed anomalous colour shifts with temperature are caused by excitonic bond-softening: in nanocrystals, the excitons are

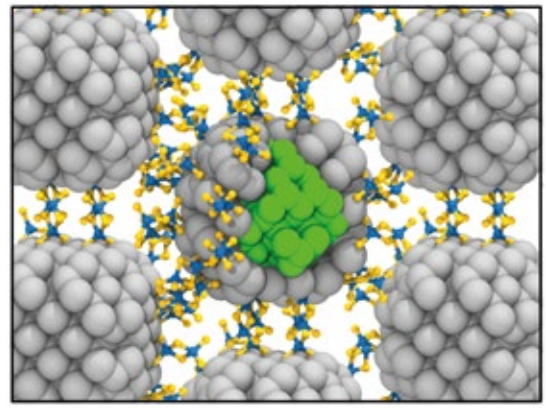

Fig. 1: *Schematic representation of a QD solid, consisting of core/shell nanocrystals assembled into a superlattice. Chalcogenidometallate complexes are used as surface-selective linkers and "conductive glue", connecting the nanocrystals both mechanically and electrically.*

distributed over only a small number of atoms due to the strong quantum confinement. In consequence, the occupation of antibonding states due to the presence of the excitons significantly weakens the interatomic bonds, leading to a pronounced exciton-induced red shift of the phonon density of states (PDOS). This shift is almost two orders of magnitudes larger than the corresponding one observed in bulk materials. The red-shifted PDOS in turn is responsible for the anomalous bandgap shift due to its impact on the Gibbs free energy of exciton formation. Our results underline the importance of explicitly considering exciton-electron-phonon coupling in nanostructures and suggest how to design systems with improved optical properties.

Moreover, the design of **heterostructures at the nanoscale**, such as multilayered structures consisting of CrN and AlN layers with a few nm thickness allows us to tune and tailor the mechanical properties for hard coating applications. In order to establish relations between the elastic properties, chemical composition and crystal structure, we investigated fast screening methods for fracture [3], but also applied novel scanning transmission electron microscopy-electron energy loss spectroscopy (STEM-EELS) methods to measure mechanical properties with nm high spatial resolution [4]. We analyzed AlN/CrN multilayers deposited epitaxially on MgO together with colleagues from Montanuniversität Leoben and TU Wien. The AlN layer thickness was increased from initially 1 nm to 10 nm, while the CrN layer thickness was kept

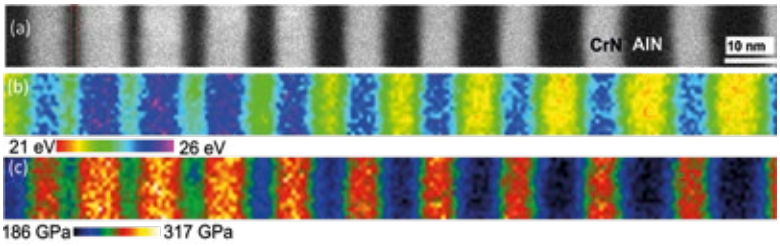

Fig 2: *a) STEM-HAADF (high-angle annular dark field) image of CrN (bright) and AlN (dark) layers grown on MgO, with AlN layer thickness increasing from 1 nm to 10 nm from left to right. (b) Corresponding low loss EELS plasmon maps and (c) bulk modulus based on an empirical relation between plasmon energy and bulk modulus. Taken from [4].*

constant at 4 nm (Fig. 2). Atomically resolved S/TEM reveals that AlN layers up to 4 nm grow in the metastable zincblende structure, while thicker AlN layers possess the room temperature stable wurtzite structure. The difference in crystal structure is also seen in the fine structure of the N-K edge in core loss EEL spectra as well as a shift in the plasmon peak positions for low loss EELS. The plasmon energy and the bulk modulus, which are related by an empirical relation established in literature were quantitatively extracted. Metastable cubic AlN, which allows for improved fracture toughness, was revealed to feature the highest bulk modulus values with 233±9 GPa in agreement with density functional theory (DFT) predictions [4].

Epitaxial strain is the origin of the long standing and highly debated issue of threading dislocations in III-Nitride materials. Nevertheless, the topic has recently been reinvigorated due to the detrimental effect they have on power electronic devices. An intriguing feature of these defects is that experimental evidence suggests that screw dislocations are associated with open core structures, thus forming **nanopipes (NPs)**. Although NPs exhibit large free surface areas which increase the energy, they can be energetically favourable if the surface energy is compensated by the core and strain energy of the material removed to create the NP.

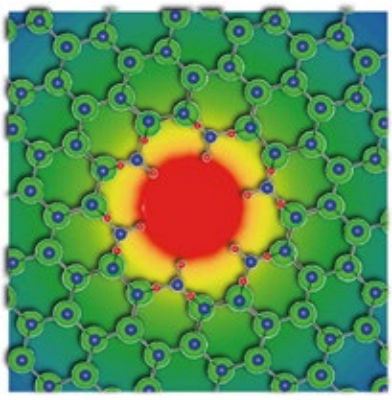

Fig. 3: *Schematic representation of the energy density associated with a full core c-type screw dislocation in GaN superimposed with the atomic structure of a hollow core defect. Hot/cold colours indicate higher/lower energy values, respectively. Green, blue and red balls indicate Ga, N, and H atoms, respectively.*

In a recent study we combined DFT calculations with elasticity theory and we investigated the mechanisms governing the formation and the properties of nanopipes. Based on these calculations we constructed a screw dislocations' phase diagram, which describes the energetically most favourable core structures as function of the species' chemical potentials. A general trend that emerges from this diagram is that nanopipes are energetically favourable under typical MOCVD or MOVPE growth conditions. Under these conditions, the cation and anion dangling bonds at the open core inner surfaces are passivated by NH_x molecules and H atoms, respectively (Fig. 3). This reduces considerably the surface energy and the formation of nanopipes with hexagonal cross section and equilibrium diameters ranging for ≈1 to ≈2 nm is energetically favourable. Nanopipes offer routes for efficient diffusion and the inner free surface sites for preferential incorporation of impurities. Indeed, our calculations indicate that both C and Mg dopants decorate the inner surface at concentrations (in at. %) at least one order of magnitude higher than in highly doped bulk semi-insulating layers [5].

The aforementioned examples from the fields of opto- and power electronics and hard coatings demonstrate that with our new methodological advances, both computational and experimental, it is now possible to reveal the complex interplay between the properties of materials at the nanoscale and their interaction with a complex growth environment. They also illustrate how our continued methodological developments guide novel applications design, and constitute an essential component in cutting-edge materials research and technology.

References

1. Rusishvili, M.; Wippermann, S.; Talapin, D.; Galli, G.: Chem. Mater. 32 (2020) 9798.
2. Muckel, F.; Lorenz, S.; Yang, J.; Nugraha, T. A.; Scalise, E.; Hyeon, T.; Wippermann, S.; Bacher, G.: Nature Comm. 11 (2020) 4127.
3. Völker, B.; Du, C.; Fager, H.; Rueß, H.; Soler, R.; Kirchlechner, C.; Dehm, G.; Schneider, J. M.: Surf. Coat. Technol. 390 (2020) 125645.
4. Zhang, Z.; Chen, Z.; Holec, D.; Liebscher, C. H.; Koutná, N.; Bartosik, M.; Zheng, Y.; Dehm, G.; Mayrhofer, P. H.: Acta Mater. 194 (2020) 343.
5. Koller, C.; Lymperakis, L.; Pogany, D.; Pobegen, G.; Ostermaier, C.: J. Appl. Phys. 130 (2021) 185702.
6. Yoo, S-H.; Lymperakis L.; Neugebauer J.: Phys. Rev. Mater. 5 (2021) 044605.

Defect phases – Thermodynamics and influence on material properties

T. Hickel[1], M. Todorova[1], L. Huber[1], C. Liebscher[2], S. Korte-Kerzel[3], C. Scheu[4], G. Dehm[2], D. Raabe[5], J. Neugebauer[1]

[1]CM, [2]SN, [3]RWTH Aachen University, [4]NG, [5]MA

To design novel alloys with tailored properties and microstructure, two materials science approaches have proven immensely successful: Firstly, thermodynamic and kinetic descriptions for tailoring and processing alloys to achieve a desired microstructure. Secondly, crystal defect manipulation to control strength, formability and corrosion resistance. However, to date, the two concepts remain essentially decoupled. A bridge between them is needed to achieve a single conceptual framework. A powerful concept to establish such a bridge are defect phase diagrams, which provide systematic tools to describe and analyse the possible chemical and structural states that specific defects can have as function of key state variables, such as chemical composition, temperature or strain.

Scientists from the RWTH Aachen University and MPIE established a large scale collaborative research centre (CRC) funded by the German Research Foundation (DFG) (see p. 76) aiming at a fundamentally new approach to achieve this goal. The key concept are defect phase diagrams, which describe the coexistence of and transitions between defect phases. The availability of such a framework will enable a paradigm shift in the description and design of future engineering materials [1].

Formally, a 'defect phase' is a structurally and chemically distinct atomic-scale defect configuration for which all physical properties can be expressed as smooth (continuous and infinitely differentiable) functions of intensive control variables such as temperature or chemical potential. A structure can only be considered a defect phase, if it is spatially confined at or next to the defect.

While the concept of defect phases has been theoretically postulated and discussed more than four decades ago, their actual observation became only possible recently with the availability of experimental techniques with atomic resolution such as aberration corrected transmission electron microscopy (TEM) and atom probe tomography (APT). For example, in a correlative study of both techniques, a local change of structure and chemistry next to dislocations in high-Mn austenitic steel and in Au-Pt alloys has been observed in the MA department [2, 3]. Nevertheless, using these highly advanced experimental techniques to systematically map defect phases (left side of Fig. 1) would be too time-consuming and due to a sensitive dependence on the thermodynamic state variables rather challenging. In the CRC we therefore aim at an alternative strategy to identify defect phases, namely guided probing. Here, physical properties of materials such as the elastic modulus or the corrosion behaviour are monitored in order to identify abrupt changes as function of the chemical potential of the involved species (right side of Fig. 1).

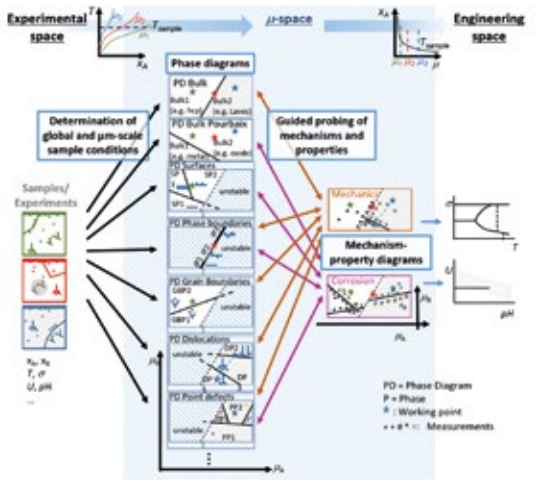

Fig. 1: *Modelling framework of defect phase diagrams. The experimental space visualizes the experimental degrees of freedom. The variety of phase diagrams for bulk and all kinds of defects is represented in the μ-space. The engineering space considers parameter dependent materials properties. Adopted from Ref. [1].*

Since the chemical composition at and around defects is intrinsically inhomogeneous, e.g., due to segregation, the natural state variable is not the concentration like for bulk phases, but the chemical potential. The constancy of the chemical potential throughout the sample in chemical equilibrium (μ-space in Fig. 1) allows one to plot the phase diagram of the bulk material and of the individual defects in the same coordinate system. This property provides a direct route to connect bulk properties with those of various defects that give rise to the complex microstructure and surfaces of materials. For the latter, the MPIE has a long-standing expertise in deriving surface phase diagrams, which is now being applied and extended within the framework of the CRC to study, e.g., the impact of alloying Mg with Ca and Al on surface structure and stoichiometry (Fig. 2). Similar defect phase diagrams can also be constructed for phase boundaries, grain boundaries, dislocations, or point defects.

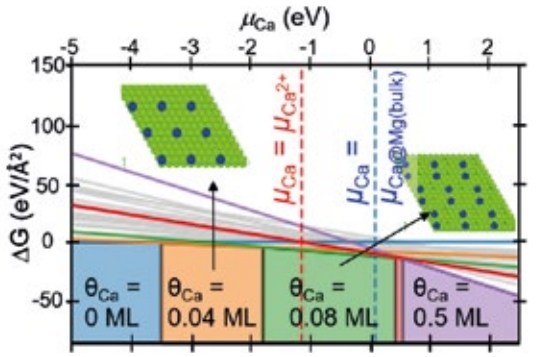

Fig. 2: *Calculated surface phase diagrams for Mg alloyed with Ca (top) and Al (bottom) in an electrochemical setup. The diagram shows as function of the Ca(Al) chemical potential the stable Ca(Al) rich phases and their compositions at Mg(0001)/water interfaces. Insets show top views of some of these structures. Dashed lines mark chemical potential conditions realized in selected measurements.*

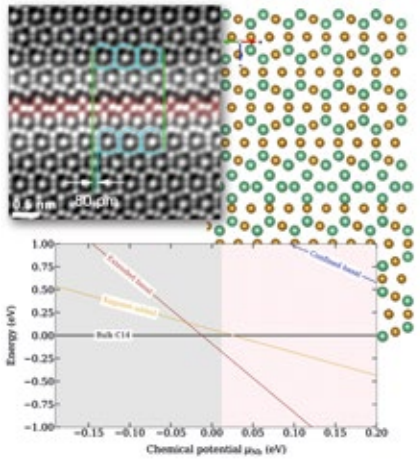

Fig. 3: *Stacking faults phases in the Nb-rich C14 Laves phase $NbFe_2$. Upper left: STEM image of an extended basal stacking fault. Upper right: Atomistic structure of the same defect as used for DFT calculations. Below: Defect phase diagram of several stacking faults (lines) as compared to the bulk phase diagram (shading). Adopted from Ref. [6].*

The rapid improvement of atomistic simulations revealed that defect phases are not rare exceptions, but should be a common feature in materials. For example, simulations in the CM department showed already in 2015 that dependent on the chemical potential of H in fcc Ni, the formation of a local hydride can be observed next to edge dislocations [4]. This is remarkable, because the hydride phase is not stable in the bulk at ambient conditions. Further extensive simulations have been performed in the CM department on grain boundaries, confirming the observation of defect phases in Al alloys by the SN department [5].

Recently, we have investigated stacking faults in the Nb-rich C14 Laves phase $NbFe_2$. The bulk phase diagram of Fe-Nb suggests a rather narrow solubility of Nb in this phase, due to the formation of the competing Nb_6Fe_7 μ-phase. Instead of this phase, however, a large number of various types of planar defects is observed in experiment [6]. The atomic configurations of these defects have been characterized by aberration-corrected scanning TEM in the SN department and density functional theory (DFT) calculations in the CM department (Fig. 3). These studies reveal that some of the stacking faults contain one layer of the characteristic Zr_4Al_3 type unit of the μ-phase (red shaded crosses in the TEM image), i.e., correspond to a defect phase that is stabilized by an excess Nb content. Nevertheless, the confinement and the stacking of atomic layers does not correspond to a bulk phase, but rather fulfil the definition of defect phases provided above.

Apart from the basal defect shown in the upper part of Fig. 3 a variety of different extended and confined stacking faults, that are lying parallel to the basal or pyramidal habit planes are observed. The DFT calculations have been used to determine the relative stability of these defect structures. In the lower part of Fig. 3 the formation energy of selected stacking faults is plotted as a function of the chemical potential. The shading in grey indicates the stability region of the C14 bulk phase. Slightly below the phase equilibrium of the μ-phase (vertical line at $\mu_{Nb} \approx 0.01$ eV), one can see the relative stability of the extended basal stacking observed in experiment. Other defect structures become lower in energy than the extended basal structure for certain chemical potentials, but do not lead to stable defect structures.

Based on these early successes, we envisage that defect phase diagrams will play the same role as their bulk counterparts. They will allow the selection of defects with a desired structural and chemical configuration, which in turn are the carriers of specific defect-property relations and, hence, enable the atomistically guided design of materials with tailored mechanical and corrosion properties.

References

1. Korte-Kerzel, S.; Hickel, T.; Huber, L.; Raabe, D.; Sandlöbes-Haut, S.; Todorova, M.; Neugebauer, J.: Int. Mater. Rev. (2021) DOI: 10.1080/09506608.2021.1930734.
2. Kuzmina M.; Herbig M.; Ponge D.; Sandlöbes, S.; Raabe, D.: Science 349 (2015) 1080.
3. Zhou X.; Mianroodi, J. R.; Da Silva, A. K.; Koenig, T.; Thompson, G. B.; Shanthraj, P.; Ponge, D.; Gault, B.; Svendsen, B.; Raabe, D.: Sci. Adv. 7 (2021) 1.
4. Leyson, G.; Grabowski, B.; Neugebauer, J.: Acta Mater. 89 (2015) 50.
5. Zhao, H.; Huber, L.; Lu, W.J.; Peter, N.J.; An, D.Y.; De Geuser, F.; Dehm, G.; Ponge, D.; Neugebauer, J.; Gault, B.; Raabe, D.: Phys. Rev. Lett. 124 (2020) 6.
6. Šlapákováa , M.; Zendegani, A.; Liebscher, C.H.; Hickel, T.; Neugebauer, J.; Hammerschmidt, T.; Ormeci , A.; Grin, J.; Dehm, G.; Kumar, K.S.; Stein, F.: Acta Mater. 183 (2020) 362.

Bidirectional transformation induced plasticity in dual-phase high entropy alloys

C. Liebscher[1], W. Lu[1,3], G. Dehm[1], F. Körmann[2], J. Neugebauer[2], D. Raabe[3], Z. Li[3]

[1]SN, [2]CM, [3]MA

Recently developed dual-phase high entropy alloys (HEAs) exhibit both an increase in strength and ductility upon grain refinement, overcoming the strength-ductility trade-off in conventional alloys [1]. Metastability engineering through compositional tuning in non-equimolar Fe-Mn-Co-Cr HEAs enabled the design of a dual-phase alloy composed of metastable face centered cubic (fcc) and hexagonal closed packed (hcp) phases. This microstructure emerges in a $Fe_{50}Mn_{30}Co_{10}Cr_{10}$ (at.%) alloy after cooling from the high temperature single phase region to room temperature through a partial martensitic transformation. Both fcc- and hcp-phases are single phase supersaturated solid solutions and the microstructural refinement associated with the martensitic transformation leads to an increase in ultimate tensile strength from ~650 MPa to ~850 MPa and total elongation from ~50% to ~75% when reducing the grain size from 45 µm to 4.5 µm [2].

We have used length scale bridging transmission electron microscopy (TEM) observations in combination with *in situ* straining in the scanning TEM (STEM) to unravel the underlying microstructural origin of this outstanding property combination in the dual-phase HEA ($Fe_{50}Mn_{30}Co_{10}Cr_{10}$ (at.%)). In the as-quenched condition, a hierarchical, nanolaminated structure is observed in both fcc (γ) and hcp (ε) phases. Upon bulk tensile straining, the microstructure dynamically refines and secondary strain-induced ε-nanolaminates form within the γ-block in the hcp ε-block, a high density of phase transformation induced γ-nanolaminates and -twins is developing. These static post-deformation observations suggest that both forward γ→ε and backward ε→γ transformations are the main carriers of plasticity in this metastable dual-phase high entropy alloy.

We also performed *in situ* straining in the STEM using a custom build Cu-straining support in a displacement controlled Gatan straining holder to probe the dynamic evolution of the hierarchical nanolaminated microstructure as shown in Fig. 1a. The pre-existing hcp ε-nanolaminates in the γ-block are observed to grow by the motion of their leading partial dislocation and their number density increases upon straining. Interestingly, we could observe the dynamic strain induced forward γ→ε and backward ε→γ transformation *in situ* in the region indicated by an

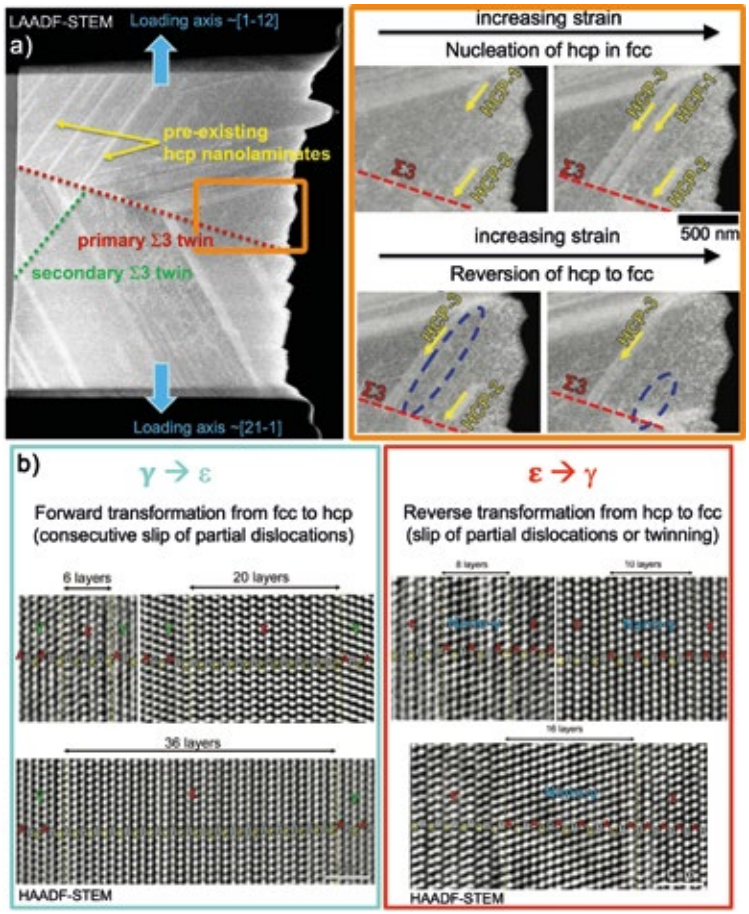

Fig. 1: *a) Low angle annular dark-field (LAADF) STEM image of the focused ion beam prepared straining sample form a fcc γ-block with pre-existing hcp ε-nanolaminates. Dynamic bidirectional forward γ→ε and backward ε→γ transformation upon straining. b) Atomic resolution STEM images of various configurations of ε-nanolaminates in a γ-block, respectively γ-nanotwins in a ε-block, after bulk tensile deformation.*

orange rectangle in Fig. 1a, referred to as "bidirectional transformation induced plasticity" (Bi-TRIP) effect.

In the early stages of straining, the nucleation of ε-plates (HCP-1-3) is observed (Fig. 1a), which continue to grow with increasing strain until their extension is blocked by the primary S3 twin boundary. By further straining, the HCP-1 and HCP-2 plates are reverted to fcc, as well as the HCP-3 plate at a later stage (not shown here). The trailing partial dislocation unzips the hcp nanolaminates, thus establishing the underlying mechanism for a novel reversable TRIP effect.

The key ingredients controlling this bidirectional transformation are the stacking fault energy, local temperature and stress-strain fields. The stacking fault energy is estimated to ~6.5 mJ/m^2 for this dual-phase HEA promoting the forward γ→ε transformation and building the basis for the reverse transformation, since local temperature or strain fluctuations can initiate the reversion by the motion of trailing partial dislocations. The reverse ε→γ transformation depends on local stress or temperature fluctuations during straining, since the hcp ε-phase is more stable than γ at room temperature. We observed that due to such fluctuations the partial dislocations moved in some cases back, thus reversing the initial phase transformation.

This concept was further extended in an interstitial HEA by deformation-driven bidirectional transformation. Controlled cold-rolling and tempering promote the formation of dual-phase nanostructures, nano-grains and -twins in a $Fe_{49.5}Mn_{30}Co_{10}Cr_{10}C_{0.5}$ (at.%) alloy resulting in an ultimate tensile strength of 1.05 GPa and a total elongation of 35 % [3]. The key design element is the tuning of the materials stacking fault energy close to its thermodynamic limit to trigger forward and reverse phase transformations upon loading. By joint activation of Bi-TRIP and twinning induced plasticity (TWIP) an excellent strength-ductility synergy can be achieved in tempered specimens with preceding-rolling reduction of 34 %.

Obtaining reliable values of stacking fault energies (SFEs) and hence relative stabilities of the fcc- and hcp-phases in these compositionally complex alloys also at non-zero temperatures is to date a big challenge. We have developed a set of density functional theory-based methods to compute the concentration dependence of SFEs [4] including magnetic and temperature effects [5]. To account for chemical disorder, different techniques are used such as the coherent potential approximation or special quasi random structures. Many of these alloys reveal complex antiferromagnetic interactions and it turned out that for achieving agreement with experimental data it is crucial to go beyond the assumption of idealized paramagnetic alloys with a careful treatment of magnetism and magnetic fluctuations [6].

References

1. Li, Z.; Pradeep, K.G.; Deng, Y.; Raabe, D.; Tasan, C.C.: Nature 534 (2016) 227.
2. Lu, W.; Liebscher, C.H.; Dehm, G.; Raabe, D.; Li, Z.: Adv. Mater. 30 (2018) 1804727.
3. Su, J.; Wu, X.; Raabe, D.; Li, Z.: Acta Mater. 167 (2019) 23-39.
4. Guo, W.; Su, J.; Lu, W.; Liebscher, C.H.; Kirchlechner, C.; Ikeda, Y.; Körmann, F.; Liu, X.; Xue, Y.; Dehm, G.: Acta Mater. 185 (2020) 45.
5. Li, Z.; Körmann, F.; Grabowski, B.; Neugebauer, J.; Raabe, D.: Acta Mat. 136 (2017) 262.
6. Wu, X; Li, Z.; Rao, Z.; Ikeda, Y.; Dutta, B.; Körmann, F.; Neugebauer, J.; Raabe, D.: Phys. Rev. Materials 4 (2020) 033601.

Interplay of chemistry and faceting at grain boundaries in a high strength Al alloy

H. Zhao[1], L. Huber[2], W. Lu[3], N. Peter[3], G. Dehm[3], D. Ponge[1], J. Neugebauer[2], B. Gault[1], D. Raabe[1]

[1]MA, [2]CM, [3]SN

Grain boundaries (GBs) are regions connecting adjacent crystals with different crystallographic orientations. GBs are a type of lattice imperfection, with their own structure and composition, and as such impact a material's mechanical and functional properties. Structural motifs and phases formed at chemically decorated GBs can be of a transient nature or are local thermodynamic structural-chemical equilibrium states. The boundary between two crystal grains can decompose into arrays of facets with distinct crystallographic characters. Faceting occurs to minimize the system's free energy, i.e., when the total interfacial energy of all facets is below that of the topologically shortest interface plane. Previously, the interplay of chemistry and faceting was revealed for specific GBs in well-defined bicrystals, which are realistically not encountered in engineering alloys. The majority of GBs in bulk metallic materials from conventional processing is of a more general type. Evidence for structural transitions in such boundaries in Al-alloys is scarce, and the interplay with chemistry is not well understood. Recently [1], we have revealed the subtle yet important interplay between the faceting of GBs and their chemical decoration with solutes in a high strength 7xxx Al alloy. We combined cutting-edge microscopy, microanalysis techniques, and atomistic simulations to demonstrate that facets exist in 7xxx Al alloy. A homogenized Al-6.22 %Zn-2.46 %Mg-2.13 %Cu (wt. %) was used for this study. The alloy was solution heat treated at 475 °C, followed by water quenching. The detailed process and precipitation behaviour during aging is described in [2]. The Σ5 grain boundary observed has a misorientation angle of 38° about a <001> common axis. Fig. 1(a) illustrates the Σ5 GB characterized by Z-contrast high-angle annular dark-field (HAADF) scanning transmission electron microscopy (STEM) performed along the common tilt <001> Al zone axis. The GB configuration contains two sets of alternating facets along the entire length, with each type highlighted by a coloured line. The orange segments are symmetric {120} facets, and the green segments are asymmetric {130} planes. Fig. 1(b) shows the energy dispersive spectroscopy (EDS) analysis from the faceted Σ5 GB. At this scale, we do not observe segregation at the {130} facets, while the {120} facets bear roughly 300 nm lathlike precipitates enriched with Mg and Cu. The HAADF-STEM image in Fig. 1(c) reveals that the precipitate has an orthorhombic structure, which matches the S phase (Al_2CuMg). The S phase is semi-coherent with the Al-matrix and has an orientation relationship of $<100>_S//<100>_{Al}$, and an interface of $\{001\}_S//\{120\}_{Al}$.

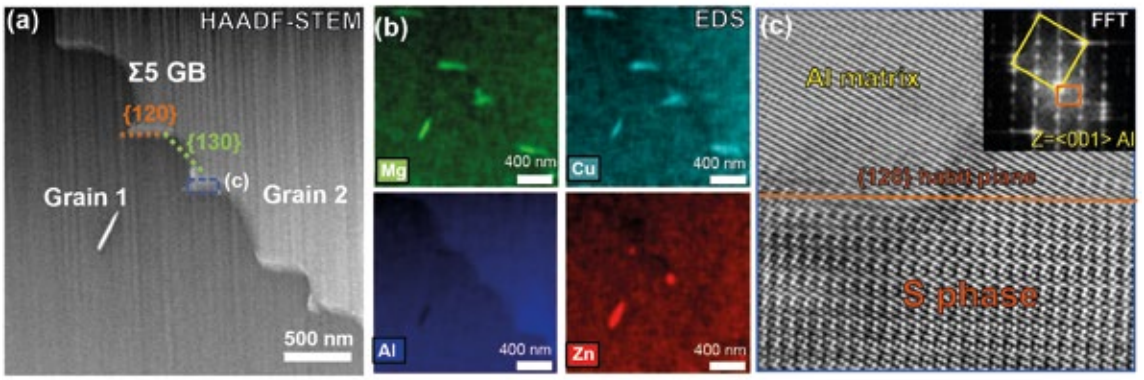

Fig. 1: *(a) HAADF-STEM image of a near Σ5 GB in the as-quenched Al-Zn-Mg-Cu alloy; (b) EDS maps of the faceted GB showing Mg and Cu enriched precipitates; (c) HAADF-STEM image of the precipitate highlighted by blue rectangle in (a), with inset of the corresponding Fast Fourier transform pattern. GB: grain boundary. Figure is from Ref. [1], published under a CC-Attribution 4.0 international license.*

polycrystalline samples, ranging in length from a few to hundreds of nanometres at GBs. We also evidenced that the local chemistry is strongly correlated with the facet character.

In the present report, we highlight one example of the near Σ5 coincident site lattice boundaries in a coarse grained

We performed complementary atom probe tomography (APT) analyses on the same Σ5 GB on another location, shown in Fig. 2. Two lathlike S phases enriched in Mg and Cu are visible in Fig. 2(a), highlighted by isosurfaces delineating regions containing more than 10 at. % Mg. A composition profile across the large precipitate was calculated along a 25 nm-diameter cylinder aligned with the

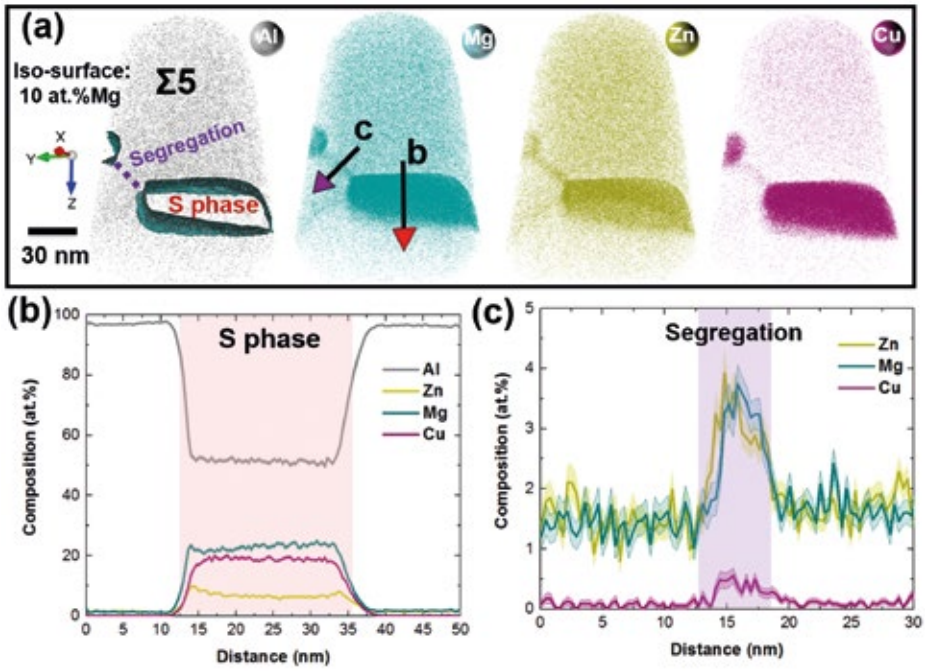

Fig. 2: *APT analysis of the same Σ5 GB with STEM analysis: (a) Atom maps of all elements; (b) Corresponding composition profile across the precipitate calculated along the red arrow; (c) Corresponding composition profile across the region between two precipitates calculated along the purple arrow. GB: grain boundary. Figure is from Ref. [1], published under a CC-Attribution 4.0 international license.*

red arrow in Fig. 2(b). It shows an average composition of 52 at. % Al, 23 at. % Mg, 18 at. % Cu, and 7 at. % Zn within the precipitate. This agrees with the stoichiometry of the S phase (Al_2CuMg). It is most likely that the 7 at. % Zn substitutes to Cu sites, as Cu and Zn are both undersized, and the combined compositions of Cu (18 at. %) and Zn (7 at. %) equals 25 at. %, as expected for the $Al_2Mg(Cu/Zn)$ stoichiometry. At this more detailed scale, we also observe Zn, Mg, and Cu enrichments along the {130} facet that connects the two precipitates and the corresponding composition profile is plotted in Fig. 2(c). The average composition in the enriched region are 3.1 at. % Zn, 3.1 at. % Mg and, 0.5 at. % Cu, which are enrichment factors of two in Zn and Mg and 3 in Cu compared to the abutting bulk solute composition. Combining the STEM and APT results, we conclude that the S phase nucleates on the {120} facets, whereas solutes segregate to the {130} facets of the faceted Σ5 GB.

We then used atomistic simulations to better understand the interplay of the chemistry and the structural faceting of the Σ5 GB. We examined the formation of a Mg-rich phase near the symmetric {120} and {130} 36.87° <001> Σ5 GBs by using the Variance Constrained Semi-Grand Canonical Molecular Dynamics/Monte Carlo (MD/MC) approach [3]. Both GBs experience various stages of segregation, from the initial decoration of the GB and adjacent planes, to the nucleation of a Mg-rich precipitate. However, the underlying energy landscape of the {120} boundary drives the precipitate to grow in perfect coherence with the decorated GB plane. In contrast, at the {130} boundary the precipitate retains double-Al-layer defects even after many MC swaps. These computational predictions rationalize that large Mg-rich phases form at each {120} facet, while the {130} facets experience only local segregation enrichment.

We also evidenced that the self-consistent co-evolution of facet structure and chemistry leads to the formation of periodic segregation patterns of 5 – 10 nm at Σ11, and Σ13a GBs [1]. Although the character of individual GB is often overlooked in the segregation study in engineering Al alloys, our study enriches the current understanding of the chemical-structural interactions. The solute segregation and heterogeneous precipitation at GBs have an impact on the corrosion properties of Al alloys. Within the same GB, the facets coupled with the anisotropic segregation and the precipitation behaviour will significantly influence the GB cohesion, intergranular fracture, and corrosion resistance of engineering Al alloys. Better predictions for the temporal evolution of the alloy's microstructure during aging and in service will require knowledge of the solute distribution within the microstructure, particularly at GBs.

References

1. Zhao, H.; Huber, L.; Lu, W.; Peter, N.; An, D.; De Geuser, F.; Dehm, G.; Ponge, D.; Neugebauer, J.; Gault, B.; Raabe, D.: Phys. Rev. Lett. 124 (2020) 106102.
2. Zhao, H.; De Geuser, F.; Kwiatkowski da Silva, A.; Szczepaniak, A.; Gault, B.; Ponge, D.; Raabe, D.: Acta Mater. 156 (2018) 318.
3. Sadigh, B.; Erhart, P.; Stukowski, A.; Caro, A.; Martinez, E.; Zepeda-Ruiz, L.: Phys. Rev. B 85 (2012) 184203.

Designing material properties by controlling impurity content in structural defects

S.-H. Yoo[1], S.-H. Kim[2], P. Chakraborty[1], A. A. El-Zoka[2], L. T. Stephenson[2], J. Lim[3], J. Neugebauer[1], T. Hickel[1], O. Kasian[4], C. Scheu[3], M. Todorova[1], B. Gault[2]

[1]CM, [2]MA, [3]NG, [4]GO

Controlling impurities in solid materials is a key to design materials' properties, putting doping at the core of modern materials technology. Increasing dopant concentration and reducing unwanted impurities in synthesised materials should make it possible to optimise the performance of target devices. This requires diverse research efforts, since establishing reliable design routes for materials containing desirable impurities requires a wide range of information ranging from atomistic insights to experimental validations. Several groups and departments at the MPIE joined forces to identify various mechanisms of impurities incorporation in solid materials by combining state-of-the-art experimental and theoretical approaches.

Given that our preliminary work showed that MNAs synthesized using $NaBH_4$ can no longer be considered pristine metallic nanostructures, we also measured the content of boron (B) incorporated in the Pd-MNAs from the $NaBH_4$ reductant and found it non-negligible. The B was found in the sub-surfaces region of the MNAs far from the surface [2]. Based on *ab initio* computed concentrations of B species on surfaces, the sub-surface layer and the bulk and taking into account the conditions during synthesis, the following scenario could be derived: B atoms adsorbed on the surface are kinetically frozen-in during the growth of MNAs by repeatedly overgrowing the top Pd surface layer by a subsequent Pd surface layer. Thus, the experimentally observed homogeneous B distribution is the consequence of non-equilibrium processes. As origin of this effect the substantially stronger binding energy of B in octahedral sites in the sub-surface region compared to surfaces [2] is identified. Such a strong binding energy of B in the sub-surface region is also found in Pd GBs [3]. Thus, B atoms are trapped in the sub-surface region of Pd-MNAs. Overall, the B content in Pd-MNAs is found to be tunable by the synthesis conditions, *i.e.*, the concentration of reductant and precursor. Hence, B can be used as a dopant to tune the properties of Pd-MNAs.

To rationalize the alkali incorporation into the Pd-MNAs, we carried out a concentration analysis based on state-of-the-art density functional theory (DFT) calculations [1]. Using chemical reservoirs to account for the experimental conditions (*i.e.*, concentrations of reductant and precursor), we determine the thermodynamic equilibrium concentrations of alkali atoms in various geometric positions on the Pd surface, in the Pd bulk or in Pd GBs using their respective *ab initio* calculated energies. The comparison between theoretically calculated and experimentally observed concentrations of Na and K reveals that the comparatively larger K atoms are kinetically trapped at GBs. The smaller Na atoms achieve, in contrast, thermodynamic equilibrium during the coalescence of two nanoparticles, *i.e.*, the joining of two surfaces, as illustrated in the left panel of Fig. 1. S.-H. Kim was awarded for this work the E.W. Müller Outstanding Emerging Scientist Award at the Atom Probe Tomography & Microscopy 2021 virtual conference.

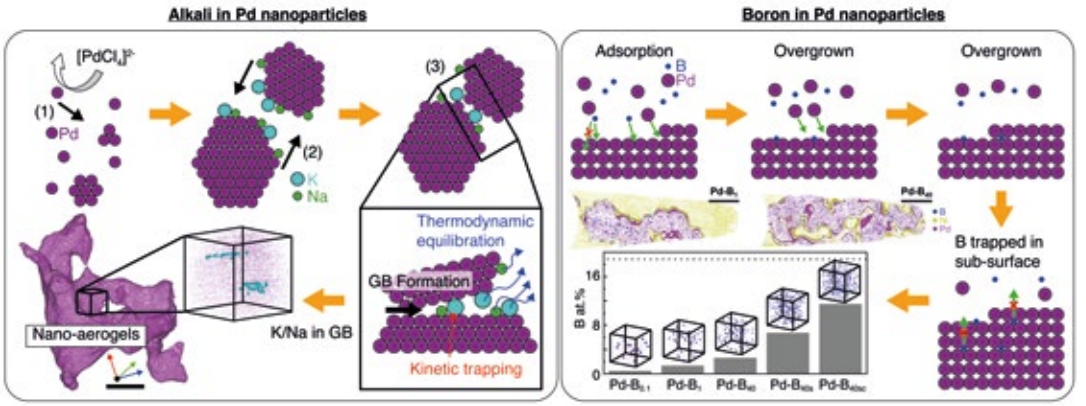

Fig. 1: *Schematic illustrations and experimental atom probe tomography (APT) validations of incorporations of impurities [alkali metals (left) and boron (right)] in Pd nanoparticles.*

Development for colloidal nanoparticles during the last 150 years allows materials scientists to synthesize nano-crystals, which are promising candidates for catalysis, by adding a reducing agent to a solution containing a metal precursor. Due to its excellent reducing properties, $NaBH_4$ is commonly used in the wet-chemical synthesis route for metal nanoparticles, since it can agglomerate to form a metallic nano-aerogel (MNA). These MNAs are often perceived as being purely metallic and free of any impurities. Yet, we directly observed the incorporation of alkali atoms (*i.e.*, Na, K) at the grain boundaries (GB) in Pd-MNAs.

to on surface binding sites was identified: The sub-surface sites are at least 1 eV/B atom more favourable.

Having unravelled these incorporation mechanisms and considering that the Pd nanoparticles are promising materials of platinum-free catalysts for various catalytic reactions (*e.g.* the hydrogen oxidation reaction), we utilise our findings to suggest design routes for Pd-B nano-catalysts with different concentrations of B, by controlling the synthesis conditions, as shown in the right panel of Fig. 1.

It becomes quite obvious that an accurate determination of the impurity content in a sample is critical to understanding its properties. An omnipresent element, particular in an electrochemical environment, is hydrogen. This element is well known to affect materials properties. A well-known adverse phenomenon is H-embrittlement. Atom probe tomography (APT) is considered as one promising measurement technique to determine H contents in materials, due to its high spatial resolution and chemical sensitivity. However, there is a consensus that H-related species (*e.g.*, H^+, H_2^+ and H_3^+) are always produced under high-fields at the specimen's surface during APT measurements. The origin of H impurities is the subject of a long-standing debate. This indetermination limits our ability to precisely quantify H concentration in materials by APT. Advancing our understanding of the behaviour of H in the conditions of an APT experiment is hence absolutely essential. It will help elucidating numerous open questions in physics, chemistry, and materials science regarding H-involving mechanisms, including hydrogen trapping or grain boundary segregation of H in the context of hydrogen embrittlement.

To solve this long-standing debate of the APT community, we perform APT analysis on two very different metals - sodium (Na) and platinum (Pt). The sample preparation of alkali metals is challenging compared to transition metals, as their reactivity in contact with moisture and air leads to severe oxidation. So far, this has hindered the characterization of alkali by APT. Here, we used the specific setup of the Laplace Project to prepare and transfer specimens [3, see also p. xxx]. The mass spectrum of the first ever reported analysis of pure Na metal, interestingly, shows no H-related species. This contrasts with Pt that shows high H peaks, typical of the APT analysis of many metals, as shown in the middle inset of Fig. 2.

This result is counterintuitive: residual H_2 molecules in an APT vacuum chamber could be expected to ionize and dissociate due to the intense electric field and/or laser pulse near the apex and thus be detected regardless of the analysed material. To elucidate this phenomenon, we used calculations to carry out a thermodynamic analysis of Na and Pt surfaces in a H_2 gas environment and understand the stability of the metal surfaces under the given experimental conditions of pressure and temperature (shown in the right panel of Fig. 2). Our analysis indicates that Na surfaces have higher resistances to surface contamination with H compared to Pt surfaces, which can explain the absence of H-related peaks observed in the APT experiments of Na. Combining the theoretical analysis and considering different conditions encountered during APT experiments, specifically, specimen-preparation, transport and APT-operating conditions, we propose that the origin of H detected in APT measurements is primarily due to H contamination of the specimen's surface occurring during specimen preparation and transport or adsorption of residual background H_2 gas, as illustrated in the left panel of Fig. 2, and not ionisation of residual hydrogen in the chamber.

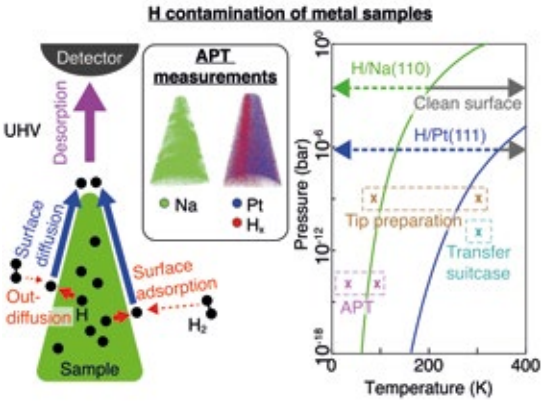

Fig. 2: *Schematic representation illustrating mechanisms of H contamination of transition metal samples (left). Experimental APT validations (in an inset) and theoretical analysis (right) to explain the experimental conditions of H contaminations.*

Our studies combining theoretical calculations, advanced characterization and catalytic activity measurements, have established the strength of 'impurity engineering' as a nanomaterial design strategy. Our collaborative activities focused on understanding the fundamental mechanisms of impurity incorporations into solid nanomaterials, which provides us with novel synthesis routes for tailoring properties of metallic structures by controlling the contents of impurities. Ongoing research [2] involving in addition the GO department will provide explicit insights into how controlling impurities in metallic nano-catalysts affects their catalytic performance for the hydrogen oxidation reaction (see p. 184).

References

1. Kim, S.-H.; Yoo, S.-H.; Chakraborty, P.; Jeong, J.; Lim, J.; El-Zoka, A.A.; Stephenson, L.T.; Hickel, T.; Neugebauer, J.; Scheu, C.; Todorova, M.; Gault, B.: J. Am. Chem. Soc. doi.org/10.1021/jacs.1c11680 (2022).
2. Kim, S.-H.; Yoo, S.-H.; El-Zoka, A.A.; Lim, J.; Jeong, J.; Schweinar, K.; Kasian, O.; Stephenson, L.T.; Scheu, C.; Neugebauer, J.; Todorova, M.; Gault, B.: in preparation.
3. Stephenson, L.T.; Szczepaniak, A.; Mouton, I.; Rusitzka, K.A.K.; Breen, A.J.; Tezins, U.; Sturm, A.; Vogel, D. ; Chang, Y.; Kontis, P.; Rosenthal, A.; Shepard, J.D.; Maier, U.; Kelly, T.F.; Raabe, D. ; Gault, B.: PLoS One 13 (2018) 1.
4. Yoo, S.-H.; Kim, S.-H.; Woods, E.; Gault, B.; Todorova, M.; Neugebauer, J.: arxiv.org/abs/2109.14981 (2021).

Hydrogen in iron alloys: from diffusion to mechanics

M.J. Duarte[1], B. Gault[2], T. Hickel[3], D. Ponge[2], J. Rao[1], M. Rohwerder[4], B. Sun[2], A. Tehranchi[3], C.-H. Wu[4], Y. Wu[2]

[1]SN, [2]MA, [3]CM, [4]GO

Hydrogen embrittles high-strength structural materials, and its consequences are particularly important in steels, which are widely used in the automotive, aeronautical, gas, oil and power generation industries. The harmful effects of hydrogen in steels have been known for more than a century and, despite of numerous studies, the underlying mechanisms are still not well understood. One of the reasons is the elusive behaviour of hydrogen: its small dimension and high mobility render difficulties to directly image it and track its effects. Another important reason lies in the existence of a large variety of lattice defects that can interact with hydrogen and the complex nature of such interactions. The study of hydrogen in iron alloys and steels is a topic shared by all departments at the MPIE and these cooperative research activities fall into the three most important categories in the hydrogen embrittlement research:

1. hydrogen trapping and transport in complex microstructures;
2. quantitative measurement of local mechanical response under defined hydrogen activity;
3. hydrogen embrittlement micromechanisms and hydrogen tolerant microstructure design.

Experiments and computational simulations are carried out in model alloys and more complex steels.

A particular challenge is the study of diffusible or lightly trapped hydrogen and its effects on the material properties. A representative case study is ferritic Fe-Cr model alloys. In the defect-free lattice they show a high hydrogen mobility and low solubility; however, the introduction of additional elements, dislocations or grain boundaries changes significantly the alloy interactions with hydrogen. The concentration of hydrogen preserved in Fe-Cr alloys with different Cr content, grain size, and dislocation densities was quantified by thermal desorption spectroscopy (TDS). The alloys with a higher Cr content, higher dislocation density or smaller grain size can retain higher amount of hydrogen upon the same hydrogen charging conditions. Permeation studies were also started by using the novel Kelvin probe-based potentiometric hydrogen electrode method. As chromium, dislocations and grain boundaries are all effective trapping sites for hydrogen, the time lag for hydrogen passing through the alloy, in first step experiments, was found to increase, indicating more trapped hydrogen, while the rate also decreased. Further research is required to verify a comparable hydrogen activity and the effect on the diffusion coefficient. The capacity for permeation measurements will be soon increased (see p. 59).

The diffusivity and amount of hydrogen in the alloys have strong consequences in the mechanical behaviour. The alloy properties will be also affected by the specific location of hydrogen, which is measured by atom probe tomography and Kelvin probe experiments. Nanoindentation studies using an innovative setup for back-side hydrogen charging during mechanical testing [1] show, for instance, a reduction of the pop-in load (Fig. 1, left) and a hardening effect with increased hydrogen ingress into the referred Fe-Cr alloys (see p. 170). The Young's modulus is not affected by the introduced hydrogen. The effect of hydrogen is yet more pronounced in the alloys with higher Cr content. In single crystal and dislocation-free Fe-Cr alloys a linear relationship between the increase in hardness and the hydrogen supply was established. This hardening effect can be attributed to an enhanced dislocation multiplication (reduction of the pop-in load), pinning on the dislocation motion and an increase in lattice friction due to hydrogen.

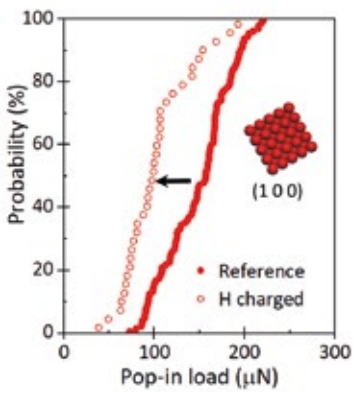

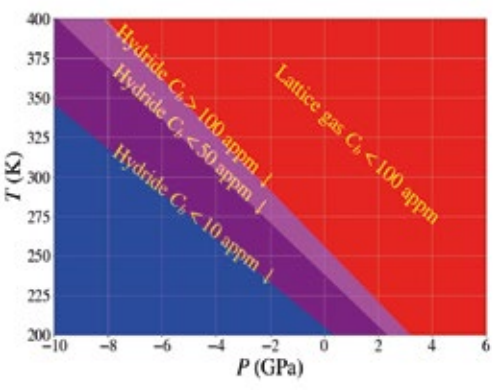

Fig. 1: *(Left) Probability plot of pop-in load during nanoindentation of Fe-20 wt.% Cr with and without hydrogen on a grain with (1 0 0) grain orientation. (Right) Pressure dependent phase diagram of the Fe_4CrH_5 hydride. C_b is the bulk concentration of hydrogen.*

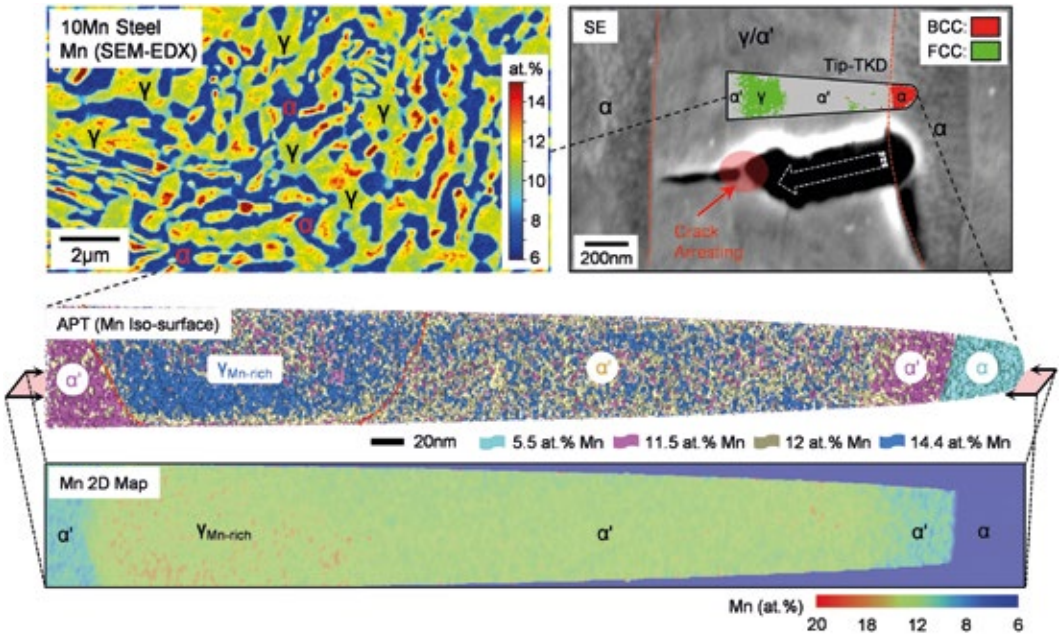

Fig. 2: *Chemically heterogeneous microstructure produced in a ferrite-austenite two phase medium Mn steel and the arresting of hydrogen-induced cracks by locally enriched Mn region which serves to locally stabilize austenite against martensite transformation.*

The reduction in the pop-in load due to the presence of hydrogen in metals is observed in the *in situ* nano-indentation experiments in various metals. The mechanism behind this reduction is not yet clear. In the case of the Fe-Cr alloys, using *ab initio* simulations, we observed attractive H-H interactions facilitating the formation of the nano-hydrides (NH). The magnitude of this attractive interaction is absent in pure Fe, but increases by increasing the Cr content. However, as it is depicted in the simulated phase diagram of Fe_4CrH_5 in Fig. 1 (right), the formation of this hydride at experimentally relevant T-C_b domain requires significant negative pressure. This tension can be attained in the vicinity of pre-existing dislocations. The formation of NHs helps homogeneous dislocation nucleation by inducing significant shear stress stemming from the misfit strain of the NH and the mismatch in its elastic moduli with respect to the metal. This finding enables us to predict the reduction in the pop-in load in Fe-Cr alloys.

In parallel to the research on the hydrogen diffusion and interaction with dislocations in model alloys, we also revealed hydrogen-induced damage mechanisms in the practically relevant transformation-induced plasticity (TRIP) steels. The deformation-driven martensitic transformation (i.e. the TRIP effect) strongly deteriorates the materials' resistance against hydrogen embrittlement, due to the high strength of the fresh martensite phase and the transformation-induced hydrogen redistribution [2]. We showed by slow strain rate tests, that the hydrogen embrittlement resistance can be significantly increased (by a factor of two) through adding stable austenite dispersed within an ultrafine grained microstructure. We exploited this microstructure design concept in a medium Mn steel (0.2C–10Mn–3Al–1Si in wt.%) and produced microscopically confined Mn heterogeneity throughout the microstructure (Fig. 2) [3]. The austenite is stabilized in the Mn enriched zone, which serves to stop hydrogen-induced cracks by blunting. On the other hand, the Mn-lean regions provide the required TRIP effect and thus a high strength-ductility combination. Such tailored microstructures with Mn heterogeneity were produced by a two-step annealing, which can be scalable to established and affordable industrial processing routes. Also, our new microstructure approach can be generalized to other types of high-strength steels with the same aim, namely, to lend their microstructures enhanced resistance against hydrogen embrittlement.

The studies of model iron alloys and complex steels lead to a better understanding of their interaction with hydrogen. This knowledge is essential in the design of hydrogen tolerant materials, required as structural alloys and for the growing use of hydrogen as energy source.

References

1. Duarte, M.J.; Fang, X.; Rao, J.; Krieger, W.; Brinckmann, S.; Dehm, G.: J. Mater. Sci. 56 (2021) 8732.
2. Sun, B.; Krieger, W.; Rohwerder, M.; Ponge, D.; Raabe, D.: Acta Mater. 183 (2020) 313.
3. Sun, B.; Lu, W.; Gault, B.; Ding, R.; Makeni, S. K.; Wan, D.; Wu, C.-H.; Chen, H.; Ponge, D.; Raabe, D.: Nature Mater. (2021) https://doi.org/10.1038/s41563-021-01050-y

Hydrogen interplay with defects in Al alloys

P. Chakraborty[1], H. Zhao[2], A. Tehranchi[1], B. Sun[2], D. Ponge[2], D. Raabe[2], T. Hickel[1], B. Gault[2]

[1]CM, [2]MA

The investigation of hydrogen in metallic alloys is a long standing key topic at the MPIE. While multiple insights on hydrogen embrittlement in steels has been gained over the last decades, similar phenomena in Al alloys have only recently come into focus, triggered by the ERC-funded SHINE project (see p. 50). Previously, Al alloys were often considered to be less affected by hydrogen embrittlement (HE), due to their superior corrosion resistance, the high activation energies for H incorporation and the low H solubility in the fcc matrix. This low solubility however can locally lead to large H concentrations at lattice defects and precipitates. Also, the increasing strength levels of modern Al alloys promote HE effects. For instance, in the high-strength 7xxx alloy series, where Zn, Mg, and Cu are main alloying elements, H-assisted crack initiation has become an issue of major concern. Three important key results connected to this phenomenon are highlighted in this report.

Competition of microstructure features in 7xxx Al alloys

The high strength of 7xxx Al alloys is achieved by its complex microstructure, containing not only grain boundaries (GBs), dislocations, micro-sized intermetallic phases but also a high dispersion of nanosized precipitates. For improving the materials' H-resilience to HE, it is important to determine for these features their respective potential for H trapping and crack initiation. Experimentally this is a highly challenging task, due to the requirement of combining highest spatial and chemical resolution with the probing sensitivity to detect individual hydrogen atoms.

The recent developments in cryo-atom probe tomography (APT) in the MA department, enabled by a completely controlled ultra-high vacuum (UVH) and cryogenic workflow consisting of charging, sample preparation and APT probing, using cryo-focused-ion beam techniques, makes it now possible to overcome this challenge. The charging of an Al-6.22Zn-2.46Mg-2.13Cu-0.155Zr (wt.%) was performed with deuterium (D), to distinguish it from residual hydrogen in the APT chamber [1]. The analysis of the data indicates a clear enrichment of D at the GB of the sample (Fig. 1b). The details of the complex GB is shown in Fig. 1c, which contains Al_3Zr dispersoids, 20-50 nm-sized (Mg, Zn)-rich precipitates, and also solutes. The compositional analysis shows that Al_3Zr-dispersoids at the GB (Fig. 1d) contain 11 at.% H and 0.6 at.% D. No enrichment in H and D(H_2^+) is shown in (Mg, Zn)-rich precipitates distributed at the GB (Fig. 3e). The locally increased content of D(H_2^+) implies that the Mg-decorated GB (i.e. devoid of precipitates) acts as a trap for H (Fig. 1f). A closer analysis is, however, required to explain why the experimentally observed crack initiates at GBs.

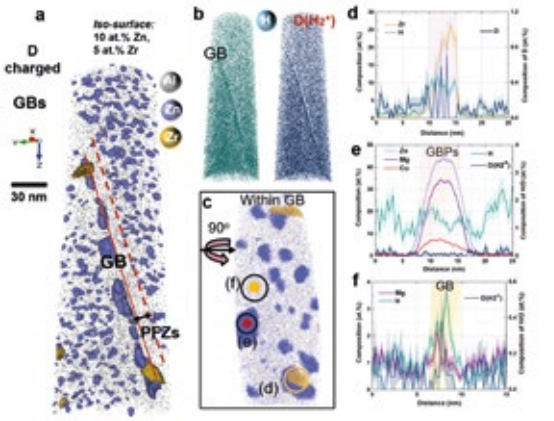

Fig. 1: *APT investigation of an Al-Zn-Mg-Cu tip that was charged with deuterium (D). The sample contains a grain boundary and a lot of Al_3Zr dispersoids, which are coarsened at the GB. Subfigure F displays a region of the GB without dispersoids. Adapted from [1].*

Therefore, density functional theory (DFT) calculations in the CM department have been used to achieve further insights into H segregation and HE. They indicate a much larger solubility of H in the dispersoids (provided Zr anti-sites are present) as compared to the GBs. It is, however, important to note that the absolute value of the embrittling energy, i.e., the H impact on the thermodynamic driving force for a decohesion of interfaces, shows a completely different trend. Despite the higher hydrogen concentration, the embrittling energy for the particles is very small. In contrast to this, the embrittling energy is larger for GBs (Fig. 2).

Effect of alloying elements on H embrittlement

The second interesting phenomenon concerns the impact of solutes on the embrittling energy. In Fig. 2 the effect of Mg is highlighted, because an enrichment of Mg next to GBs was also observed in APT (Fig. 1). The DFT calculations reveal hardly any change in the H segregation energy to the GB if Mg atoms are additionally present. However, the impact of even minor traces of solute Mg on the embrittling energy is still rather large. This is due to the highly attractive interaction of Mg and H at the new surfaces that form during crack initiation.

Due to these important atomistic observations the interaction of H with GBs in Al alloys has been studied more systematically. After extending the study to several types

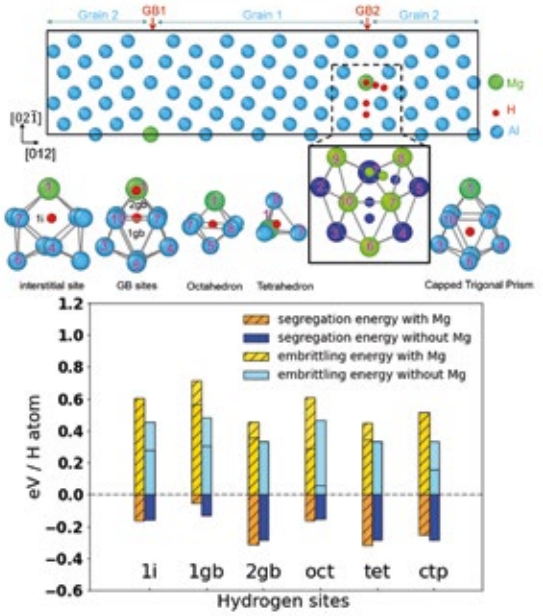

Fig. 2: *DFT calculations for the segregation and embrittling energy of H in a Σ5 (210) GB. The analysis has been performed for different interstitial sites in the GB, comparing a scenario with and without Mg atoms nearby the H sites. Adapted from [1].*

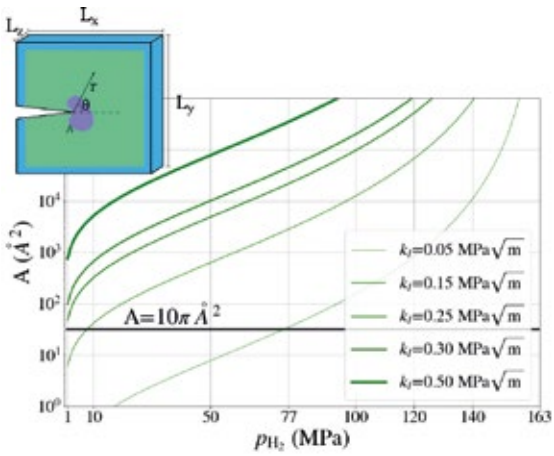

Fig. 3: *Distribution of the cross-sectional area of the hydrides formed around the crack tip at T = 300 K versus the H_2 pressure for different values of the cracks stress intensity factor. The schematic diagram for an Al alloy containing a local hydride (purple) next to a crack tip is also shown.*

of GBs, we were able to correlate the solution enthalpy to a relative change in the Voronoi volume and to generalize the finding to a model for the solution enthalpy. This will allow a prediction of the solution enthalpy even for GBs that are too complex to be treated by DFT calculations.

The extension to several alloying elements relevant for the 7xxx series of Al alloys reveals that the behaviour of Mg is not unique, but that solute Sc and Zr have a qualitatively similar and even larger impact on the H embrittlement. The solute atom Sn, however, turns out to be highly interesting, because it strongly binds with H in the GB, without increasing the embrittling tendency. Based on these insights, effective alloying strategies to improve the resistance to HE can be developed.

Impact of the microstructure on hydride formation

The difference described above between the hydrogen solubility in the bulk phase and in the vicinity of GBs already indicates a strong impact of the microstructure. If cracks form, this can go so far that hydride formation becomes possible. Due to the relevance for hydrogen storage applications, the Al hydride formation has, therefore, been further investigated as prototypical example of a metallic hydride former enhanced by defects.

To this end, DFT calculations have first been used to determine the formation enthalpy of the most common Al hydrides in their pure bulk phases as a function of the H chemical potential and a negative mechanical pressure in the system. The former can be modified by the external H_2 gas pressure, whereas the latter is subject to an external load. These calculations reveal that a negative pressure field of magnitude −4 GPa significantly reduces the formation energy of α-Alane hydride, but is negligible for the other hydride phases.

The presence of negative pressure fields at a crack tip is well-known. It is best described by the stress-intensity factor, which itself is proportional to an external load. Hence, by the application of a tensile strain to the sample, a control of the stress intensity factor and, therefore, of the formation of local hydrides becomes feasible. In order to demonstrate this effect, the formation energy of the Alane hydride is modified by including the interaction of its excess volume and the stress field of a tensile crack. The schematic diagram of the hydride and crack as well as the enhancement in formation of the hydride are illustrated in Fig. 3. In the absence of an external load, an unrealistically high hydrogen gas pressure of 163 MPa would be required in order to form a hydride phase. If a k-load of ≈0.15 MPa√m is applied, a hydride with a critical size for the cross-sectional area is already formed with a gas pressure of 10 MPa. The value should be compared with the critical k-load for dislocation emission next to cracks, which is about 0.3 MPa√m. The findings need to be critically balanced against the failure of the material due to brittle fracture and HE, but the potential of defects for the formation of metallic hydrides becomes evident from this study.

References

1. Zhao, H.; Chakraborty, P.; Ponge, D.; Hickel, T.; Sun, B.; Wu, C.-H.; Gault, B.; Raabe, D.: Nature (2021) accepted.

Near-atomic-scale analysis of hydrides

B. Gault[1], W. Lu[2], S. Zhang[3], C. Scheu[3], P. Chakraborty[4], T. Hickel[4], Y. Chang[1], I. Mouton[1], C. Liebscher[2], G. Dehm[2], D. Raabe[1]

[1]MA, [2]SN, [3]NG, [4]CM

Hydrides are hydrogen-containing stable phases. Most hydrides are mechanically brittle and their formation associated to hydrogen ingress in materials over the course of their service life is a major contributor to the 'hydrogen embrittlement' of entire classes of engineering alloys. Titanium and zirconium are known bulk hydride formers, and their alloys are often subject to hydride-related failure. The detailed study of their formation mechanisms remains highly challenging. Scanning and transmission-electron microscopy (S & TEM) and associated techniques require dedicated specimen preparation protocols for reliably revealing hydride formation, since hydrogen can be introduced into the specimen by the sample preparation alone. We have developed methodologies that enable to differentiate between hydrides formed in the sample during preparation vs. those stemming from the preceding environmental exposure by for example hydrogen charging. Although atom probe tomography (APT) is known to be capable of 3D compositional mapping with sub-nanometre resolution for a wide range of materials, there are very few studies of hydrides and solute hydrogen analysis remains an absolute frontier [1]. Here we set ourselves to investigating the detailed formation mechanisms of hydrides in some zirconium and titanium alloys.

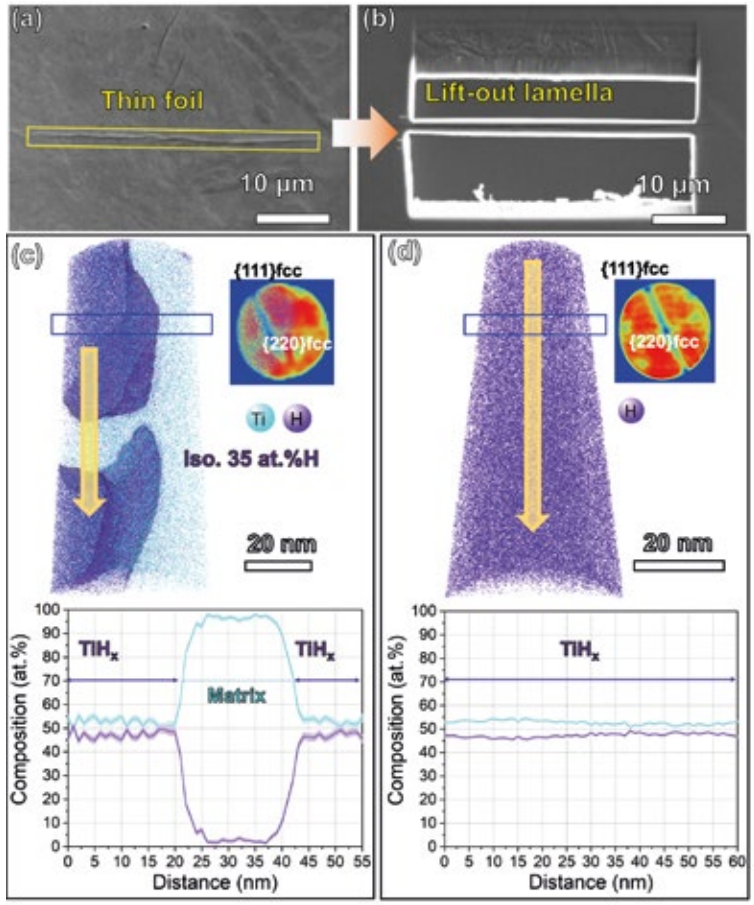

Fig. 1: *Semi-correlative APT analysis of fcc-hydrides in the electropolished TEM specimen. (a) and (b) are SEM images of the site-specific APT sample preparation of a lenticular hydride. (c) and (d) show 3D atom maps, detector histograms and 1D concentration profiles. The detector histograms and concentration profiles are extracted from the blue rectangle and yellow arrow, respectively. (c) Concentration profile across two matrix-hydride interfaces extracted across the yellow arrow. The ion detection map shows a {220}fcc pole. (d) 3D atom map and 1D concentration profile within the hydride.*

In titanium and its alloys, we first demonstrated the possibility to measure hydrogen content and partitioning between the different phases, and analyse hydrides by APT [2]. We discussed the importance of alloying to avoid hydride formation, too. However, the hydrogen-content was ill-controlled, coming from the specimen preparation, and we then demonstrated the importance of using cryogenic-temperature during the final stage of specimen preparation to avoid the introduction of spurious hydrogen and hydrides [3], as well as our capacity for forming and studying Ti-hydrides by APT [4]. Finally, we combined high-resolution TEM with electron-energy loss spectroscopy and APT (Fig. 1) to demonstrate that a phase that is sometimes identified as a face-centred cubic allotrope of Ti is, in fact, simply a hydride formed during the preparation of the specimens [5].

As part of the ERC Consolidator Grant Shine project (see p. 50), a collaboration was established with colleagues at Imperial College London (group of T.B. Britton, now at University of British Columbia). They used electrochemical charging of Zr-alloys to introduce high concentrations of hydrogen or deuterium, and by adjusting the cooling rate following a homogenisation heat treatment, provided samples with hydride at different stages of growth. The study of both hydrides and deuterides formed under similar conditions allowed us to optimise the analysis conditions and ensure reliable compositional analyses [6]. In slow cooled samples, we reported on the partitioning of Sn away from intergranular hydrides, with a strong pile-up at the interface, in the vicinity of which metastable interfacial hydride between the δ-hydride and the metallic matrix was detected [7]. We observed no redistribution of other major alloying elements (e.g. Fe) that appear mostly segregated to the GBs, but revealed that Sn is also found segregated to stacking faults forming ahead of the hydride growth front, because of the difference in lattice parameter between the hydride and the metallic matrix [8]. A follow-up study was performed on a fast-cooled sample, and demonstrated that the Sn partitioning already takes places from the early stage and that nucleation of hydrides can be aided by the presence of secondary-phase particles across the metallic matrix [9].

Importantly all these studies demonstrated the possibility of performing clean high-resolution imaging and quantification of hydrogen both as a solute and inside of different phases in these materials.

References

1. Breen, A.J.; Stephenson, L.T.; Sun, B.: Li, Y.; Kasian, O.; Raabe, D.; Herbig, M.; Gault, B.: Acta Mater. 188 (2018) 108.
2. Chang, Y.; Breen, A.J.; Tarzimoghadam, Z.; Kürnsteiner, P.; Gardner, H.; Ackerman, A.K.; Radecka, A.; Bagot, P.A.J.; Lu, W.; Jägle, E.A.; Herbig, M.; Stephenson, L.T.; Moody, M.P. Rugg, D.; Dye, D.; Ponge, D.; Raabe, D.; Gault, B.: Acta Mater. 150 (2018) 273.
3. Chang, Y.; Lu, W.; Guénolé, j.; Stephenson, L.T.; Szczpaniak, A.; Kontis, P.; Ackerman, A.K.; Dear, F. F.; Mouton, I.; Zhong, X.; Zhang, S.; Dye, D.; Liebscher, C.H.; Ponge, D.; Korte-Kerzel, S.; Raabe, D.; Gault B.: Nature Comm. 10(1) (2019) 942.
4. Chang, Y.; Mouton, I.; Stephenson, L.T.; Ashton, M.; Zhang, G.; Szczpaniak, A.; Lu, W.; Ponge, D.; Raabe, D.; Gault, B.: New J. Phys. 21 (2019) 053025.
5. Chang, Y.; Zhang, S.; Liebscher, C.H.; Dye, D.; Ponge, D.; Scheu, C.; Dehm, G.; Raabe, D.; Gault, B.; Lu, W.: Scripta Mater. 178 (2020) 39.
6. Mouton, I.; Breen, A.J.; Wang, S.; Chang, Y.; Szczepaniak, A.; Kontis, P.; Stephenson, L.T.; Raabe, D.; Herbig, M.; Gault, B.: Microsc. Microanal. 25(2) (2019) 481.
7. Breen, A. J..; Mouton, I.; Lu W; Wang, S.; Szczepaniak, A.; Kontis, P.; Stephenson, L.T.; Chang, Y.; Kwiatkowski da Silva, A.; Liebscher, C.H.; Raabe, D.; Britton, T.B.; Herbig, M.; Gault, B.: Scripta Mater. 156 (2018) 42.
8. Mouton, I.; Chang, Y.; Chakraborty, P.; Wang, S.; Stephenson, L.T.; Britton, T.B.; Gault, B.: Materialia 15 (2021) 101006.
9. Lu, W.; Kontis, P.; Wang, S.; Birch, R.; Wenman, M.; Gault, B.; Britton, T.B.: arXiv:2109.10955.

Mn segregation at Fe grain boundaries

O. Hegde[1], A. Kwiatkowski da Silva[2], D. Ponge[2], T. Hickel[1], J. Neugebauer[1]

[1]CM, [2]MA

Grain boundary segregation in metallic alloys can be connected with important phenomena [1] such as spinodal decomposition, heterogenous phase nucleation, suppressed coarsening, embrittlement and crack initiation. Due to their advanced mechanical behaviour, high- and medium Mn steels belong to the most important metallic alloys studied at the MPIE within the last decades. Due to the dual benefit of scientific novelty as well as industrial relevance, the observation of spinodal fluctuations at grain boundaries in Fe-Mn alloy by the MA department in 2018 [2] has initiated intensive research at the MPIE in the last years.

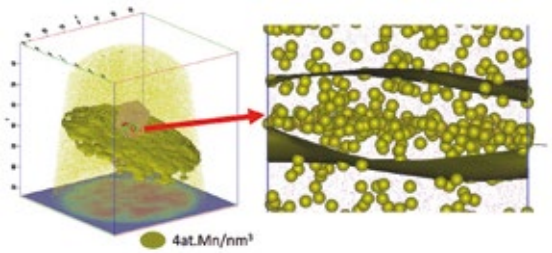

Fig. 1: *Detail of a monolayer of Mn atoms segregated at a GB in a Fe-4 at%Mn alloy aged during 2 months at 450 °C. Mn atoms are represented as yellow spheres and iron atoms as pink dots.*

Figure 1 shows such an atom probe tomography (APT) analysis of a grain boundary enriched with Mn in a Fe-4 at%Mn alloy. The segregation of the Mn atoms to the grain boundary (GB) is clearly highlight by the iso-concentration profile. In similar experiments with Fe-9 at.% Mn alloys [2] it was shown that the enrichment can yield the nucleation of an austenitic phase at the GB with a composition of 32 at.% Mn. Combining the chemical information with thermodynamic modelling, spinodal decompositions and the formation of defect phases (see p. 192) have been discussed in this context.

The underlying physical mechanisms are a result of highly interesting coupling phenomena: First of all, in order to achieve a grain boundary engineering, a series of thermal treatments need to be performed in experiments. This does not only yield the above-described chemical segregation. During this process, also the magnetic properties in the vicinity of the grain boundary can be altered. In high temperature heat treatments, the magnetic entropy supports the magnetically disordered state (or paramagnetic state) in the material. However, the link between magnetic states (particularly the paramagnetic state) and segregation is unexplored in the literature, due to the theoretical and computational complexities in handling magnetically disordered state in particular in the presence of the structural complexity imposed by grain boundaries. Here, some methodological achievements in this regard are highlighted.

Segregation in magnetically ordered and disordered states

First-principles density functional theory (DFT) based approaches are adopted to determine segregation profiles in the magnetically ordered ferromagnetic state and disordered paramagnetic states (see p. 71). Within the adiabatic approximation, since the magnetic degrees of freedom are much faster than the atomic ones, a spin-space average (SSA) based relaxation scheme [3] is developed to compute energies in the paramagnetic state. The segregation energies for Mn at different sites in the Σ5(310) grain boundary are presented in Fig. 2.

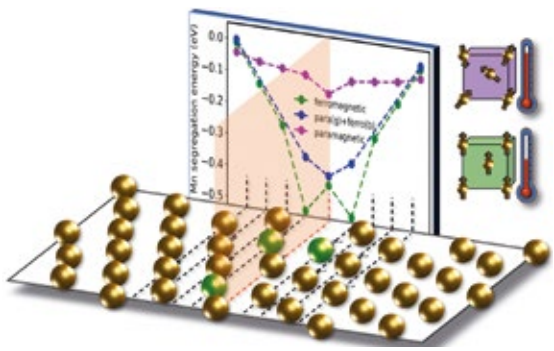

Fig. 2: *Schematic of the Σ5(310) grain boundary with dashed lines indicating layers next to the GB layer (red line). The diagram shows the segregation energies in the ferromagnetic and paramagnetic states. Green/golden balls indicate Mn/Fe atoms.*

The negative values of segregation energy in Fig. 2 indicate favourable segregation. The segregation drive is large in the ferromagnetic state. This is not only a thermodynamic observation, but also kinetic *ab initio* studies show a higher ratio of the Mn/Fe diffusion rate in the ferro- as compared to the paramagnetic state [4]. Further, the sites in the layer next to the grain boundary in the ferromagnetic state turn

out to be the most favourable. This is counter-intuitive, since one would expect the site in the grain boundary layer to be most favourable, because of the larger size of the Mn atoms. To explain this, we show magnetic interaction parameters and segregation energies of antiferromagnetic Fe atom in the ferromagnetic environment in Fig. 3.

Here, a larger value of magnetic interaction parameter at a particular site indicates that incorporation of an antiferromagnetic Fe atom at that site is more unfavourable. Clearly, the lowest value at site 2 confirms that the preference of Mn at this site is mainly due to its antiferromagnetic nature. The presence of an antiferromagnetic atom at this site reduces the magnetic repulsion between two otherwise closely situated ferromagnetic atoms.

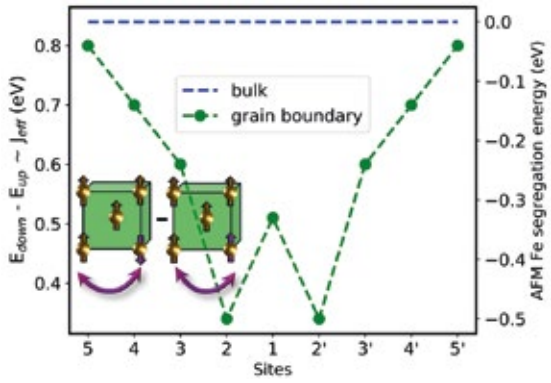

Fig. 3: *Magnetic interaction parameters at different sites of the grain boundary. The corresponding segregation energies of antiferromagnetic Fe atoms are shown in the second y-axis.*

At the same time, the result in Fig. 3 can also be interpreted as segregation profile for an antiferromagnetic Fe atom, with a segregation energy shown in the secondary *y*-axis. Interestingly, this profile is qualitatively and quantitatively very similar to that of the Mn segregation in Fig. 2. Finally, the absence of this feature in the paramagnetic state, where the magnetic moments are random by default and the Mn moment is not special, further confirms that the segregation of Mn at Fe grain boundaries is largely driven by magnetic interactions. Therefore, the segregation drive in the paramagnetic state is significantly smaller as compared to the ferromagnetic state.

Magnetic, chemical, and structural interplay at the grain boundary

While the impact of magnetic states on segregation profiles is discussed above, question arises as to whether the formation of grain boundary and Mn segregation could in turn affect the local magnetic state. Computing the magnetic transition temperature from the ferromagnetic to paramagnetic state, i.e., the Curie temperature, helps in

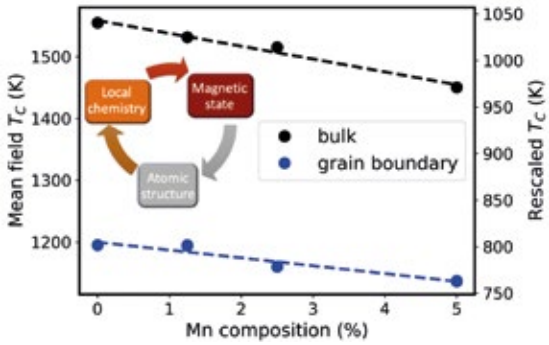

Fig. 4: *Mean field Curie temperatures for the grain boundary structure and the bulk bcc structure with respect to Mn concentration. The secondary y-axis shows the Curie temperatures rescaled to the experimental value.*

classifying the magnetic state at any given temperature. Therefore, Curie temperatures calculated for both the bulk and grain boundary as a function of Mn concentration are shown in Fig. 4. Since the mean-field definition overestimates the bulk bcc Fe Curie temperature, the rescaled values (by the corresponding factor) are shown in the secondary *y*-axis. The figure conveys two remarkable messages: (1) The Curie temperature substantially reduces by the presence of a grain boundary. (2) The accumulation of Mn at the grain boundary results in further reduction in the Curie temperature with a rate of 12 K/at.%. Due to both effects, there exists a temperature window where the grain boundary exhibits the paramagnetic state whereas the bulk is ferromagnetic. Thus, the figure reveals an impressive coupling of structure, chemistry, and magnetism at FeMn grain boundaries. The direct access to Curie temperature facilitates the determination of the magnetic state of the grain boundary at any given temperature, the knowledge of which can be used to derive the segregation energies and occupancies pertaining to that magnetic state at the given temperature. In this way, one can provide new opportunities for segregation engineering in experiments based on quantitative prediction from computations.

References

1. 1. Raabe, D.; Herbig, M.; Sandlöbes, S.; Li, Y.; Tytko, D.; Kuzmina, M.; Ponge, D.; Choi, P.-P.: Curr. Opin. Sol. Stat. Mater. Sci. 18 (2014) 253.
2. 2. Kwiatkowski da Silva, A.; Ponge, D.; Peng, Z.; Inden, G.; Lu, Y.; Breen, A.; Gault, B.; Raabe, D.: Nature Comm. 9 (2018) 1137.
3. 3 Hegde, O.; Grabowski, M.; Zhang, X.; Waseda, O.; Hickel, T.; Freysoldt, C.; Neugebauer, J.: Phys. Rev. B 102 (2020) 144101.
4. 4. Hegde, O.; Kulitckii, V.; Schneider, A.; Soisson, F.; Hickel, T.; Neugebauer, J.; Wilde, G.; Divinski, S.; Fu, C.-C.: Phys. Rev. B 104 (2021) 184107.

Interstitials in high entropy alloys

W. Lu[1,2], C. Liebscher[1], Y. Ikeda[3], F. Körmann[3], Z. Li[2], G. Dehm[1], J. Neugebauer[3], D. Raabe[2]

[1]SN, [2]MA, [3]CM

Interstitial alloying in high-entropy alloys (HEAs) is an important strategy for tuning and improving their mechanical properties. Strength can be increased due to interstitial solid-solution hardening, while interstitial alloying can simultaneously affect, e.g., stacking fault energies (SFEs) and thus trigger different deformation mechanisms. While this provides a variety of opportunities, it introduces at the same time a further degree of complexity. An understanding of the fundamental mechanisms on the atomic scale is therefore crucial.

For HEAs, each interstitial site displays a different local environment and thus a specific solution energy (Fig. 1). Resolving such complex local configuration dependencies is usually not accessible to experiments alone. We therefore investigated the impact of interstitials (C and N) on the equiatomic CrMnFeCoNi HEA based on first-principles calculations [1, 2]. Both, the face-centred cubic (fcc) and the hexagonal close-packed (hcp) phases of CrMnFeCoNi were modelled based on the supercell approach to evaluate SFEs. The solution energies of interstitial C and N atoms are computed for both phases. A large number of interstitial sites are investigated to elucidate the dependence on the local environments around the interstitial atoms. By scanning over various chemically different local environments, a highly realistic representation of the stability and the energetics of interstitials in CrMnFeCoNi could be obtained.

Interestingly, the distribution of the interstitial C solution energies (Fig. 1) shows a width of more than 1.5 eV, which is an order of magnitude larger than the thermal energy at relevant annealing temperatures (approximately 0.1 eV at 1000 K). This large variation of solution energies also indicates a strong dependence of them on the local environment of C. Utilizing different thermodynamic statistical treatments it is found that both, C and N, increase the SFEs [1, 2]. This is consistent with our experimental observations that interstitial C increases the stability of the fcc phase in a metastable non-equiatomic FeMnCoCrC alloy [3]. Our analysis of local correlations revealed further, that C in CrMnFeCoNi energetically prefers interstitial sites with lower local valence-electron concentration, suggesting segregation of C into Cr-rich environments, hence promoting Cr-rich carbides. Indeed, we experimentally found that Cr-rich $M_{23}C_6$ carbides can be found in the non-equiatomic FeMnCoCrC alloy after annealing [3]. Due to the slightly increased SFE and the trend to form Cr-rich carbides by introducing the interstitial element C, the non-equiatomic FeMnCoCrC alloy unifies all metallic strengthening mechanisms including precipitation strengthening, twinning- and transformation-induced plasticity, apart from the massive substitutional and interstitial solid solution strengthening, leading to twice the tensile strength compared to an interstitial-free HEA with similar composition, yet, at fully maintained ductility [3].

We have further extended the alloy design concept by interstitial alloying to nanostructure HEAs thereby increasing their strength and high temperature stability. This nanostructuring was explored in a model $Fe_{19.84}Mn_{19.84}Co_{19.84}Cr_{19.84}Ni_{19.84}C_{0.8}$ (at.%) iHEA processed by cold-rolling and subsequent annealing at 800 °C and 900 °C [4].

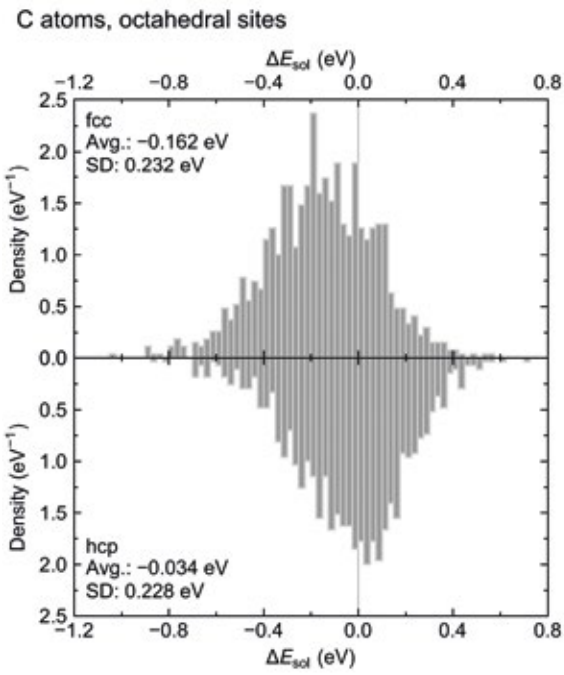

Fig. 1: *Distribution of computed solution energies of interstitial C atoms at the octahedral sites in CrMnFeCoNi. The upper and the lower panels show the results for the fcc and the hcp phases, respectively. The average (avg.) and the standard deviation (SD) of the solution energies are also shown in the panels, revealing that C increases the stacking fault energy (fcc – hcp stability).*

After the annealing treatment at 900 °C the microstructure of the iHEA is characterized by recrystallized and nano-twinned regions. A deep microstructural characterized by scanning / transmission electron microscopy (S/TEM) and atom probe tomography (APT) revealed that elongated $M_{23}C_6$-type nanocarbides (Fig. 2) are forming

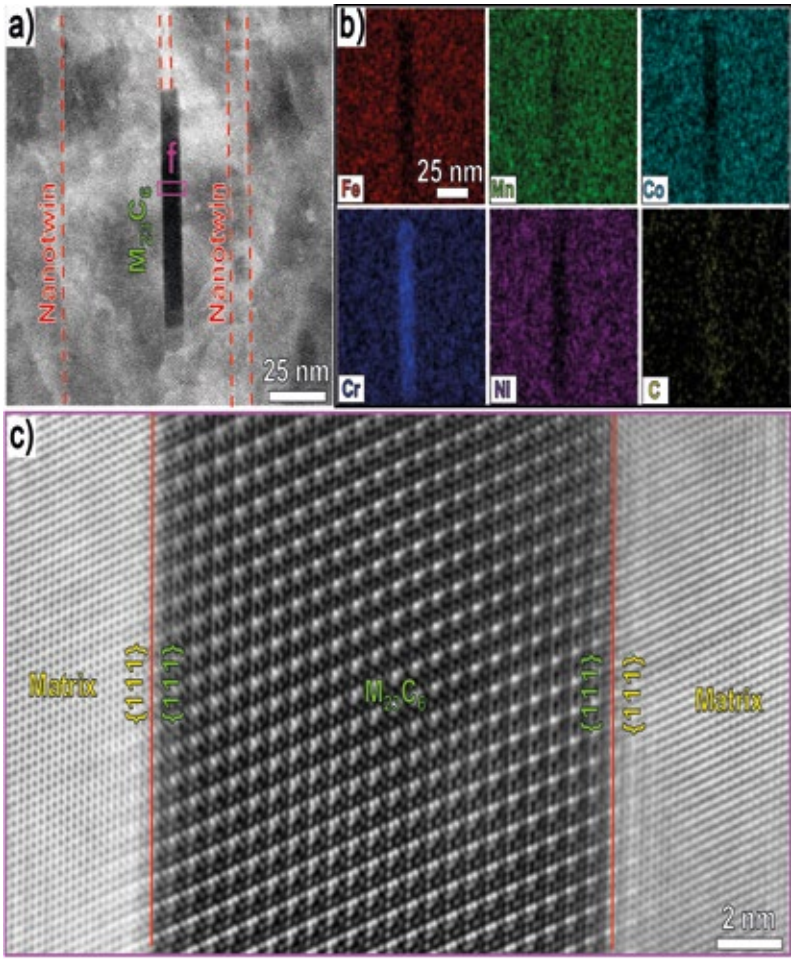

Fig. 2: *STEM analysis of elongated nanocarbides. (a) High-angle annuar dark-field imaging-STEM image of a nanocarbide that precipitated along nanotwin boundaries. (b) The corresponding STEM-EDS maps reveal a strong enrichment of Cr in the carbide. (c) Atomic structure of the elongated $M_{23}C_6$ (M: Fe, Mn, Co, Ni, Cr) by high-resolution STEM from the carbide shown in (a) revealing the orientation relationship between matrix and nanocarbide: $<110>_{matrix}$ //$<110>_{nanocarbide}$ and $\{111\}_{matrix}$//$\{111\}_{precipitate}$.*

along the nanotwins, stabilizing them even up to elevated temperatures of 800 °C. This heterogeneous microstructure leads to a significant increase in ultimate tensile strength of >1.2 GPa compared to an equiatomic FeMnCoCrNi HEA with ~700 MPa. It also provides outstanding high temperature mechanical properties resulting in yield strengths of ~650 MPa and ~300 MPa at 600 °C and 700 °C, respectively. The underlying mechanisms of the formation of the nanocarbides were explored by atomic resolution and *in situ* S/TEM. We found that nanoscale 9R structures are forming along the nanotwin boundaries before the annealing treatment. Their high dislocation content accelerates C diffusion and hence they serve as nucleation sites for the formation of the elongated $M_{23}C_6$-type nanocarbides. These nanophases stabilize the nanotwins enabling to overcome the trade-off between strength and thermal stability, thus qualifying these interstitially alloyed HEAs as promising pathway for the design of strong and ductile thermally stable bulk nanotwinned materials.

References

1. Ikeda, Y.; Tanak, I.; Neugebauer, J.; Körmann, F.: Phys. Rev. Mat. 3 (2019) 113603.
2. Ikeda, Y.; Körmann, F.: J. Phase Equilib. Diffus. 42 (2021) 551.
3. Li, Z.; Tasan, C. C.; Springer, H.; Gault, B.; Raabe, D.: Sci. Rep. 7 (2017) 40704.
4. Lu, W.; Liebscher, C.H.; Yan, F.; Fang, X.; Li, L.; Li, J.; Guo, W.; Dehm, G.; Raabe, D.; Li, Z.: Acta Mater. 185 (2020) 218.

Advanced compositionally complex alloys

W. Lu[1,2], C. Liebscher[1], G. Dehm[1], Y. Ma[2], Z. Li[2], C. Liu[2], G. Wu[2], Z. Rao[2], D. Ponge[2], B. Dutta[3], F. Körmann[3], J. Neugebauer[3], D. Raabe[2]

[1]SN, [2]MA, [3]CM

The exploration of high dimensional composition alloy spaces, where five or more alloying elements are added at near equal concentration, triggered the development of so-called high entropy (HEAs) or compositionally complex alloys (CCAs). This new design approach opened vast phase and composition spaces for the design of new materials with advanced mechanical and functional properties.

The development of alloys with tailorable strength and ductility was enabled by compositional tuning of FeMnCoCrNi alloys. By adjusting the Fe/Mn ratio it was possible to obtain single phase face centered cubic (fcc) alloys, which predominantly deform via nanotwining and dislocation plasticity, equipping them with an excellent strength-ductility synergy [1]. The key factor controlling the dominant deformation mechanism is rooted in the Mn content, which ultimately impacts the stacking fault energy as shown by density functional theory calculations. In dual-phase FeMnCoCr alloys a novel bidirectional transformation induced plasticity effect was observed, which explains the outstanding work-hardening capacity in these alloys [2]. To enhance the capabilities in mechanical properties to elevated temperatures, we also extended the alloy design concept to interstitial alloying (see p. 208) with C in FeMnCoCrNiC alloys [3]. In this way it was possible to stabilize nanotwinned regions by the precipitation of nano-carbides up to temperatures of 800 °C providing excellent mechanical properties for temperatures of up to 700 °C with a tensile yield strength of ~300 MPa.

Amorphous-crystalline nanocomposite structures have been found to promote an ultrahigh yield strength with large deformability. The alloy design concept was realized in a FeCoCrNiSiB high-entropy nanocomposite [4] and Cr-Co-Ni (crystalline, ~18 nm-thick)/TiZrNbHfCrCoNi (amorphous, ~12 nm-thick) laminate composite alloy [5], respectively. Furthermore, the laminate composite alloy exhibits ~200 K higher crystallization temperature (TX> 973 K) compared to that of the original TiZrNbHf-based amorphous phase. The elemental partitioning among adjacent amorphous and crystalline phases leads to their mutual thermodynamic and mechanical stabilization, opening up a new symbiotic approach for stable, strong and ductile materials. These design concepts were then adapted to develop wear-resistant metals, which achieve superior wear resistance via *in situ* formation of a strong and deformable oxide crystal-glass nanocomposite surface during wear in an oxidative environment – referred to as 'reactive wear protection' [6]. This reactive wear protection strategy offers a pathway for designing ultra-wear resistant alloys.

In an approach to also explore the potential of CCAs for magnetic applications we combined experimental investigations and theoretical calculations to unveil an abnormal magnetic behaviour caused by addition of the nonmagnetic element Cu in face-centred-cubic FeNiCoMn-based CCAs [7]. Interestingly, upon Cu addition, the CCAs show an increase of both Curie temperature and saturation magnetization in as-cast and homogenized states. Also, the saturation magnetization of the as-cast HEAs at room temperature increases by 77 % and 177 % at a Cu content of 11 and 20 at. %, respectively, compared to the initial, Cu-free as-cast equiatomic FeNiCoMn HEA. We found that the increase in saturation magnetization of the as-cast HEAs is associated with the formation of an Fe-Co rich phase. For the homogenized alloys, the magnetic state at room temperature transforms from a paramagnetic into a ferromagnetic one upon addition of 20 at.% Cu. Both, the increase of the saturation magnetization as well as the Curie temperature could not be adequately explained by the formation of Cu enriched zones according to our atom probe tomography (APT) analysis. Our *ab initio* calculations suggest that Cu plays a crucial role in the stabilization of a ferromagnetic ordering of Fe, and also reveal an increase of the Curie temperature caused by the Cu, a result which agrees well with the experimental findings. The underlying mechanism behind this phenomenon lies in a combined change in unit-cell volume and chemical composition and the related energetic stabilization of the magnetic ordering upon Cu alloying as revealed by our theoretical calculations. The possibility to improve the magnetic properties of HEAs by addition of nonmagnetic elements like Cu opens a great avenue to further exploring HEAs for magnetic applications.

An alternative route to improve the magnetic properties of multicomponent alloys has been to render a massive solid solution metastable and to trigger spinodal decomposition [8]. The motivation for starting from a HEA has been to provide the chemical degrees of freedom required to tailor spinodal behaviour using multiple components. The key idea is to form Fe-Co enriched regions which have an expanded volume (relative to a hypothetical unconstrained Fe-Co bulk), due to coherency constraints imposed by the surrounding HEA matrix. As demonstrated by our theory and experiments, this leads to improved magnetic properties of the decomposed alloy relative to the original solid solution matrix. In a pro-

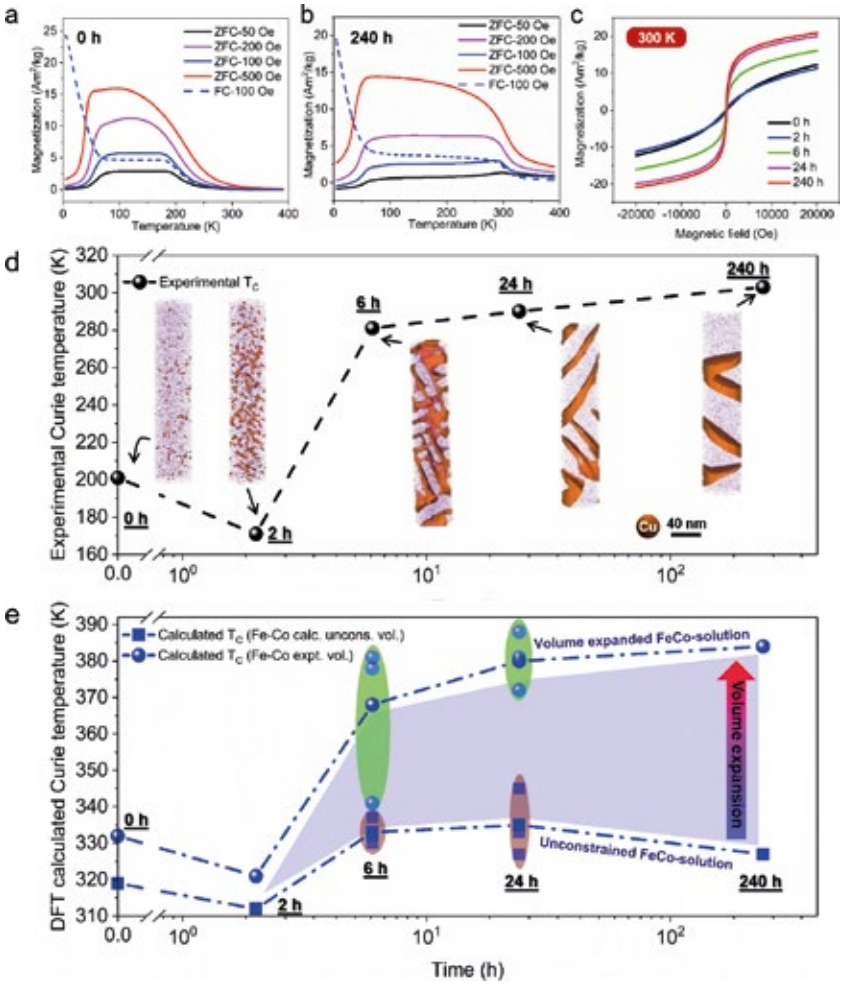

Fig. 1: *Magnetic properties of the FeCoNiMnCu HEA samples exposed to different processing conditions. a) Temperature dependence of magnetization of the homogenized and b) 600 °C/240 h annealed HEA samples. c) Hysteresis loops with different annealing time at 300 K. d) Experimental Curie temperatures as a function of annealing time. The morphological evolution of the alloy's nanostructure as a function of annealing time is shown in terms of APT reconstructions, showing also 50 at. % iso-composition surfaces of Cu. e) DFT calculated Curie temperatures as a function of annealing time. The blue shaded area indicates the impact of strain induced volume dilatation on the Curie temperature, i.e., the difference between the Curie temperature calculated for a hypothetical free-standing unconstrained single-phase bulk-like Fe-Co alloy and that for the experimentally measured strained volume of the same region in the HEA. Oval shapes indicate fluctuations due to scatter in local compositions (squares and circles) among different APT specimens.*

totype magnetic FeCoNiMnCu HEA, it is shown that the modulated structures, achieved by spinodal decomposition, lead to an increase of the Curie temperature by 48 % and a simultaneous increase of magnetization by 70 % at ambient temperature as compared to the homogenized single-phase reference alloy (Fig. 1). These findings open a pathway towards the development of advanced functional HEAs for magnetic applications.

References

1. Guo, W.; Su, J.; Lu, W.; Liebscher, C.H.; Kirchlechner, C.; Ikeda, Y.; Körmann, F.; Liu, X.; Xue, Y.; Dehm, G.: Acta Mater. 185 (2020) 45.
2. Lu, W.; Liebscher, C.H.; Dehm, G.; Raabe, D.; Li, Z.: Adv. Mater. 30 (2018) 1804727.
3. Lu, W.; Liebscher, C.H.; Yan, F.; Fang, X.; Li, L.; Li, J.; Guo, W.; Dehm, G.; Raabe, D.; Li, Z.: Acta Mater. 185 (2020) 218.
4. Wu, G.; Balachandran, S.; Gault, B.; Xia, W.; Liu, C.; Rao, Z.; Wei, Y.; Liu, S.; Lu, J.; Herbig, M.; Lu, W.; Dehm, G.; Li, Z.; Raabe, D.: Adv. Mater. 32 (2020) 2002619.
5. Wu, G.; Liu, C.; Brognara, A.; Ghidelli, M.; Bao, Y.; Liu, S.; Wu, X.; Xia, W.; Zhao, H.; Rao, J.; Ponge, D.; Devulapalli, V.; Lu, W.; Dehm, G.; Raabe, D.; Li, Z. Mater. Today 51 (2021) 6.
6. Liu, C.; Li, Z.; Lu, W.; Bao, Y.; Xia, W.; Wu, X.; Zhao, H.; Gault, B.; Liu, C.; Herbig, M.; Fischer, A.; Dehm, G.; Wu, G.; Raabe, D.: Nat. Commun. 12 (2021) 5518.
7. Rao, Z; Dutta, B.; Körmann, F.; Ponge, D.; Li, L.; He, J.; Stephenson, L.; Schäfer, L.; Skokov, K.; Gutfleisch, O.; Raabe, D.; Li, Z.: Phys. Rev. Mat. 4 (2020) 014402.
8. Rao, Z; Dutta, B.; Körmann, F.; Lu, W.; Zhou, X.; Liu, C.; da Silva, A.; Wiedwald, U.; Spasova, M.; Farle, M.; Ponge, D.; Gault; B. Neugebauer, J.; Raabe, D.; Li, Z.: Adv. Funct. Mat. 31 (2021) 2007668.

Developing high-strength and damage-tolerant crystalline thin-film materials

J.P. Best[1], C. Liu[2], G. Wu[2], Z. Li[2,3], C. Du[1], C. Scheu[4], D. Raabe[2], G. Dehm[1], J.M. Schneider[5]

[1]SN, [2]MA, [3]Central South University, P.R. China, [4]NG, [5]RWTH Aachen University

Wear-related energy loss and component damage, including friction and remanufacturing of components that failed by surface contacts, has an incredible cost. While high-strength materials generally have low wear rates, homogeneous deformation behaviour and the accommodation of plastic strain without cracking or localised brittle fracture are also crucial for wear-resistant metals. High-strength and tough coatings have a large role to play within this space, and in this interdepartmental project we have developed both techniques such as high-throughput tensile testing [1], and advanced materials systems such as MAX phase Cr_2AlC coatings [2] and novel interstitial solid solution strengthened thin films [3], to address this challenge.

Amorphous-crystalline nanocomposite thin-films have also been found to promote an ultrahigh yield strength with large deformability, as shown for the Fe-Co-Cr-Ni-Si-B system [4]. We also present a new strategy to develop thermally stable, high-strength and deformable crystal-glass nanocomposites (Fig. 1a-d) through a thermodynamically guided alloy design approach, which mimics the mutual stabilisation principle known from symbiotic ecosystems. We realised this in form of a model Cr-Co-Ni (crystalline, ~18 nm-thick)/Ti-Zr-Nb-Hf-Cr-Co-Ni (amorphous, ~12 nm-thick) laminate composite alloy [5]. The symbiotic alloy has an ultrahigh compressive yield strength of 3.6 GPa and large homogeneous deformation of ~15 % strain at ambient temperature, with ~200 K higher crystallisation temperature compared to the original TiZrNbHf-based amorphous phase. The elemental partitioning among adjacent amorphous and crystalline phases leads to their mutual thermodynamic and mechanical stabilisation, opening up a new symbiotic approach for stable, strong and ductile materials.

These design concepts were then adapted to develop wear-resistant metals, which achieve their superior properties via *in situ* formation of a strong and deformable oxide nanocomposite surface during wear in an oxidative environment. This was realised for a multi-component $(TiNbZr)_{75}Ag_{25}$ alloy, by blending a TiNbZr medium-entropy alloy with Ag [6]. A ball-on-disk sliding test at maximum contact stress of 1.0 GPa revealed an alloy with low friction coefficient in air. From this tribological contact, a ~400 nm thick nanocomposite layer is formed on the crystalline alloy surface, with ~10 nm-sized Ag nanocrystals embedded in the amorphous oxide matrix (Fig. 1e). Nanopillar compression tests of the friction-induced nanocomposite reveal a yield strength of 2.4 GPa and homogeneous deformation to 20 % strain [6]. This strong and deformable oxide nanocomposite surface promotes an ultralow wear rate of the $(TiNbZr)_{75}Ag_{25}$ alloy, compared to TiNbZr or $(TiNbZr)_{75}Ag_{25}$ alloy tested in Ar atmosphere, demonstrating a pathway for designing ultra-wear resistant alloys.

Thermal stability and oxidation resistance are also defining properties for advanced material systems, including coated components used in e.g. energy conversion applications. The MAB phase MoAlB is a promising candidate for such applications since the formation of a dense and adherent alumina scale has been reported for bulk samples. X-ray phase pure, orthorhombic MoAlB coatings were grown at 700 °C for the first time [7]. These coatings exhibit similar oxidation behaviour compared to bulk MoAlB since the oxide scale formed on MoAlB coatings after oxidation at 1200 °C for 30 min was similar to the one extrapolated for bulk MoAlB (Fig. 2), with improved oxidation kinetics than bulk Ti_2AlC. High-resolution transmission electron microscopy reveals an interplanar spacing which is in excellent agreement with the lattice parameter determined by X-ray diffraction and *ab initio* predictions [7] as well as literature reports. In selected area electron diffraction and compositional area fraction analysis, additional, yet unidentified, Al-rich and O-rich minority phases were observed [8]. These findings are significant because the formation of 2D MBenes (2D metal borides) was observed in the vicinity of the O-rich segregations [8]. In addition to exploring the direct synthesis of 2D MBenes by magnetron sputtering, current research focuses on improving the crystal quality [9] and purity of the MoAlB coatings and heterostructures (see p. 26).

References

1. Völker, B.; Du, C.; Fager, H.; Rueß, H.; Soler, R.; Kirchlechner, C.; Dehm, G.; Schneider, J.M.: Surf. Coat. Tech. 390 (2020) 125645.
2. Völker, B.; Stelzer, B.; Mráz, S.; Rueß, H.; Sahu, R.; Kirchlechner, C.; Dehm, G.; Schneider, J.M.: Mater. Des. 206 (2021) 109757.
3. Liu, C; Lu, W.; Xia, W.; Du, C.; Rao, Z.; Best, J.P.; Brinckmann, S.; Lu, J.; Gault, B.; Dehm, G.; Wu, G.; Li, Z.; Raabe, D.: Nature Comm. accepted.
4. Wu, G.; Balachandran, S.; Gault, B.; Xia, W.; Liu, C.; Rao, Z.; Wei, Y.; Liu, S.; Lu, J.; Herbig, M.; Lu, W.; Dehm, G.; Li, Z.; Raabe, D.: Adv. Mater. 32 (2020) 2002619.
5. Wu, G.; Liu, C.; Brognara, A.; Ghidelli, M.; Bao, Y.; Liu, S.; Wu, X.; Xia, W.; Zhao, H.; Rao, J.; Ponge, D.; Devulapalli, V.; Lu, W.; Dehm, G.; Raabe, D.; Li, Z. Mater. Today 51 (2021) 6.
6. Liu, C.; Li, Z.; Lu, W.; Bao, Y.; Xia, W.; Wu, X.; Zhao, H.; Gault, B.; Liu, C.; Herbig, M.; Fischer, A.; Dehm, G.; Wu, G.; Raabe, D.: Nat. Commun. 12 (2021) 5518.

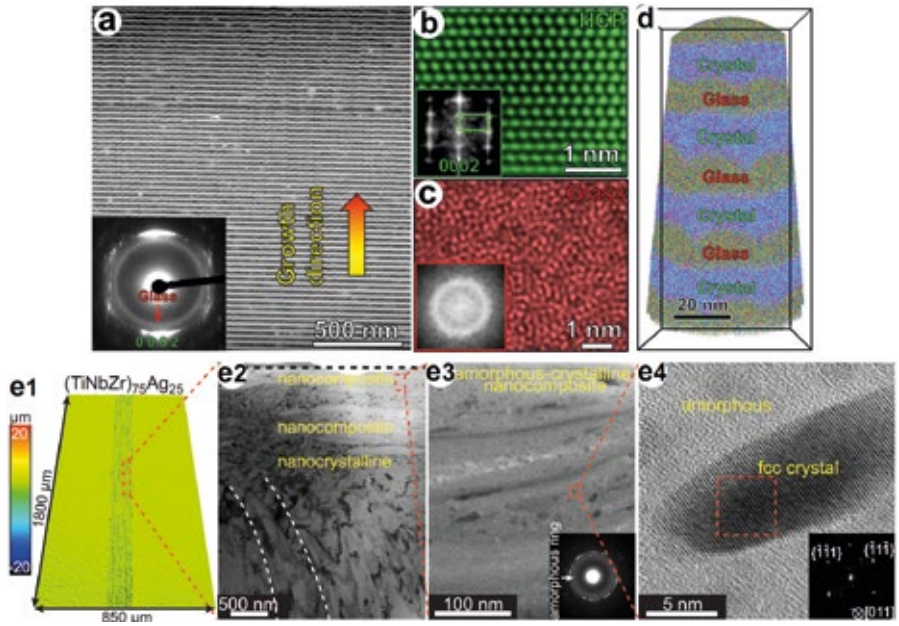

Fig. 1: *Microstructure and composition of the symbiotic alloy. High angle annular dark-field scanning transmission electron microscopy (STEM) image (a) with selected area electron diffraction (SAED) pattern (inset) shows an amorphous ring and diffraction pattern with a strong {0 0 0 2} texture. Side-view high-resolution STEM images showing hcp crystalline CrCoNi phase probed along the <1 1 -2 0> zone axis (b) and maze-like pattern of the amorphous phase (c). The corresponding fast Fourier transformation (FFT) insets show that the {0 0 0 2} plane is perpendicular to the growth direction and the glass phase presents a typical diffuse ring feature. 3D reconstruction of an atom probe tomography (APT) dataset, showing nano-laminated structure (d). 3D profile of $(TiNbZr)_{75}Ag_{25}$ wear surface is shown (e1) together with: TEM image presenting a ~400-nm-thick amorphous-crystalline nanocomposite on the surface (e2); Annular bright field (ABF)-STEM image displaying the structure of the nanocomposite (e3, inset SAED); Atom-resolved ABF-STEM image highlighting a fcc structured nanocrystal embedded in the amorphous matrix (e4, inset FFT).*

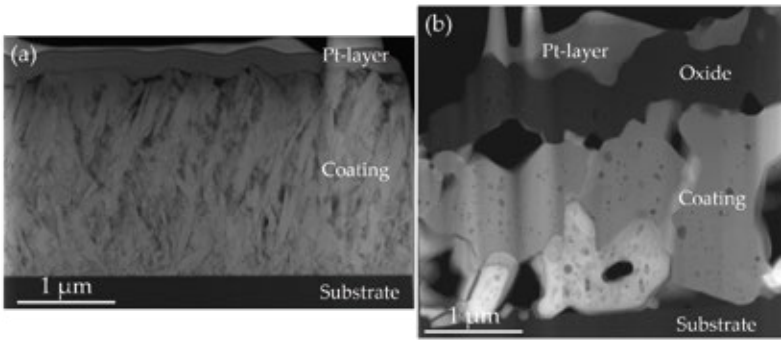

Fig. 2: *STEM images of close-to-stoichiometric MoAlB coating; (a) as-deposited, (b) after oxidation in ambient air at 1200 °C. The top layer corresponds to the Pt protection layer, which is deposited during the focussed ion beam (FIB) sample preparation, adapted from [7].*

7. Achenbach, J.-O.; Sahu, R.; Völker, B.; Hans, M.; Primetzhofer, D.; Miljanovic, D.J.; Scheu, C.; Schneider, J.M.: Coatings 9 (2019) 510.
8. Sahu, R.; Bogdanovski, D.; Achenbach, J.-O.; Zhang, S.; Hans, M.; Primetzhofer, D.; Schneider, J. M.; Scheu, C.: Nanoscale 13 (2021) 18077.
9. Evertz, S.; Pöllmann, P.; Holzapfel, D.M.; Mayer, E.; Schneider, J.M.: J. Eur. Ceram. Soc. 41 (2021) 6302.

Design of tough metallic glasses

S. Evertz[1], G. Wu[2], G. Dehm[1], C. Kirchlechner[1,3], M. Ghidelli[1,4], D. Raabe[2], J. M. Schneider[5]

[1]SN, [2]MA, [3]Karlsruhe Institute of Technology, [4]LSPM/CNRS Université Sorbonne Paris Nord, [5]RWTH Aachen University

The promising mechanical properties of metallic glasses (MG) such as high hardness, yield strength, and toughness [1] are desirable to exploit for structural applications. Monolithic MGs lack grains and grain boundaries; thus, the mechanical properties of MGs are depending on the chemistry as well as processing and testing conditions. However, despite the promising properties, catastrophic failure is often observed, especially under uniaxial tension.

While most investigations on the mechanical properties of MGs have focussed on the topology of the atomic motifs, attention must also be placed on the nature of the local chemical bonding, which is the basis of atomic cohesion and hence mechanical properties [2]. However, while elastic properties can be directly calculated from *ab initio* calculations, mechanical properties such as fracture toughness, which involves the rearrangement of atoms, need new predictors and their validation [2]. Here, we present a predictor for the fracture toughness of MGs based on the electronic structure.

The brittle to tough transition cannot be universally predicted based on the Poisson's ratio [2]. Instead, based on a comparison of the *ab initio* electronic structure and the fracture toughness of $Cu_{70}Zr_{30}$ and $Pd_{57}Al_{24}Y_8Cu_{11}$, we hypothesize that the fraction of hybridized bonds with respect to the overall bonds is a qualitative fingerprint of fracture toughness [3]: The lower the fraction of hybridized bonds, the higher the fracture toughness. Hence, the fraction of metallic bonds needs to be maximized to enhance fracture toughness [4]. Since the fraction of hybridized bonds can be obtained from *ab initio* calculations by calculating the crystal orbital overlap population (COOP) [5], the predictor for fracture toughness focuses on minimizing the COOP. For purely metallic bonding the electrons at the Fermi level E_f are delocalized. Hence, for an ideal MG in terms of toughness, COOP(E_f) = 0 [2, 4].

The experimental fracture toughness of MG scales with the COOP(E_f) (Fig. 1) [4]. Based on the fit of the data, the unknown fracture toughness of a $Pd_{57}Al_{24}Y_8Ni_{11}$ can be predicted to be 95 ± 20 MPa $m^{0.5}$ [4]. However, as indicated by the negative COOP(E_f) in Fig. 1a, not only the fraction of hybridized bonds is crucial, but also the anti-bonding bonding character at E_f, which leads to a higher energy in the system and promotes bond separation [4].

To critically appraise this new predictor for the fracture toughness of MGs, micro-mechanical bending tests on magnetron sputtered $Pd_{58}Al_{25}Y_5Ni_{12}$ thin films were performed. In these experiments, the cantilevers showed formation of multiple shear bands confined by the stress gradient (Fig. 1b), with no crack extension [4]. Hence, the fracture toughness exceeds the boundaries of micromechanical fracture experiments, which is consistent with the high toughness predicted for this material [4]. However, despite the large plasticity observed here in a complex stress state and with a small size, strain localization in uniaxial tension can still lead to catastrophic failure by strain localization.

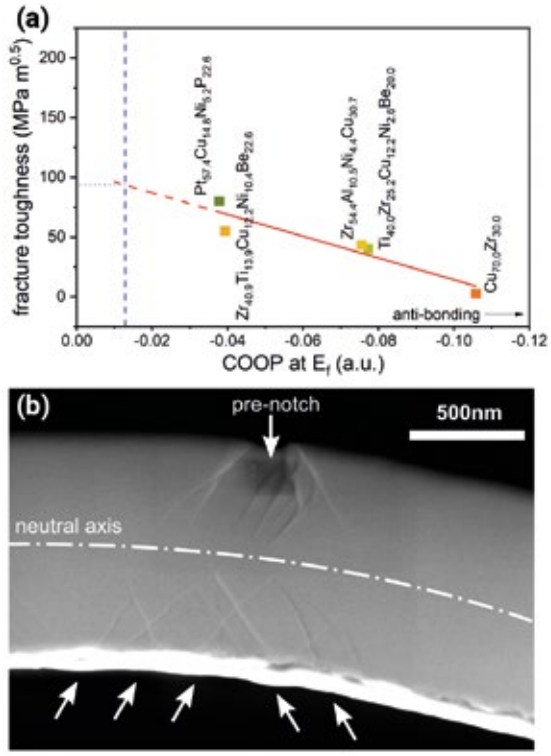

Fig. 1: *(a) Fracture toughness of five different MGs as a function of crystal orbital overlap population (COOP) at the Fermi level E_f. The red solid line is a linear fit of the data points. The dashed blue line indicates the COOP(E_f) of $Pd_{57}Al_{24}Y_8Ni_{11}$ and the dotted blue line indicates the predicted fracture toughness. (b) In-lens-SE micrograph of the notch region of a micro-cantilever after micro-bending to 4 µm deflection. Severe shear band formation is observed around the notch as well as on the compressive side of the cantilever (see arrows) [4].*

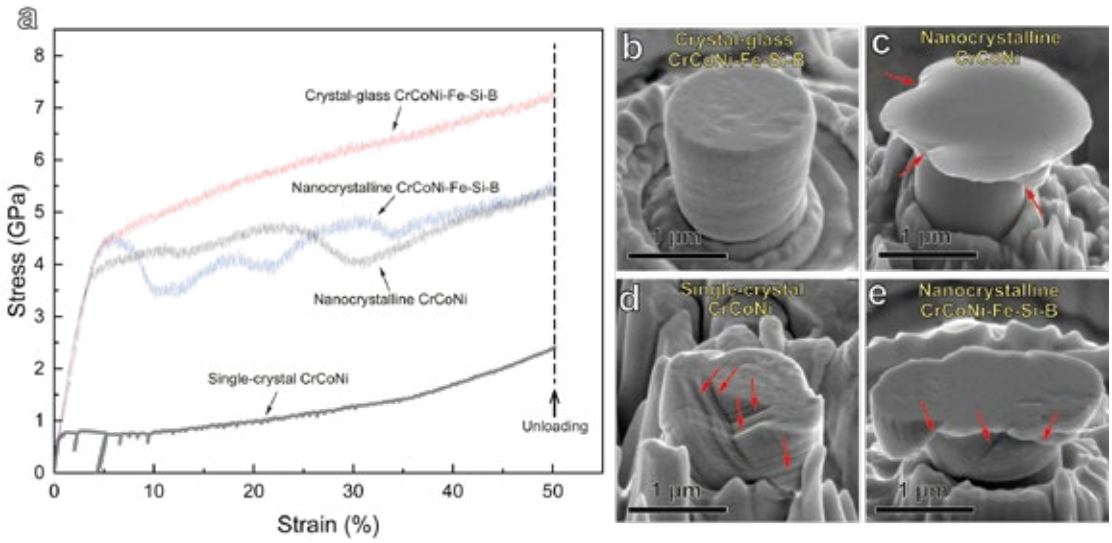

Fig. 2: *Mechanical properties of a CrCoNi-Fe-Si-B crystal–glass high-entropy nanocomposite. (a) Compressive engineering stress–strain curves of the crystal-glass CrCoNi-Fe-Si-B high-entropy nanocomposite, nanocrystalline CrCoNi-Fe-Si-B, nanocrystalline CrCoNi, and single-crystal CrCoNi pillar samples, each with the same diameter of 1 μm. (b)–(e) Scanning electron microscopy (SEM) images of the same samples after compression to an identical engineering strain of 50 %. Some of the shear bands in (c) and (e) and slip bands in (d) are indicated by red arrows.*

Glass-matrix composite materials can prevent strain localization by exploiting plasticity of MGs for spatially confined geometries. By combining MGs with e.g. nanocrystalline high-entropy alloys (HEAs), ductile materials with near-theoretical strength can be obtained [6].

By doping a magnetron sputtered Cr-Fe-Co-Ni HEA with the glass-forming elements B and Si, a nanocomposite structure composed of a ~1 nm-thick amorphous phase surrounding the 8 nm-thick crystalline HEA columnar grains was formed [6]. In micro-mechanical compression tests, the crystal-glass composite exhibits a yield strength of 4.1 GPa (Fig. 2), which is higher than that of the nanocrystalline reference alloy with a similar composition. Moreover, the crystal-glass high-entropy nanocomposite reveals homogeneous plastic deformation without formation of visible shear bands (Fig. 2) [6].

During plastic deformation of the crystal-glass nanocomposite, the nanograins are gradually subdivided, creating additional interfaces against dislocation motion [6]. The formation of additional interfaces compensates the work softening from de-twinning. Stress-concentrations by dislocation pile-ups at the grain boundaries are prevented by the absorption of dislocations in the amorphous phase. The interplay of continuous partial dislocation formation, movement, and annihilation promotes the homogeneous and compatible plastic deformation of the crystal-glass composite [6].

In conclusion, the here introduced predictor for fracture toughness based on the electronic structure obtained by *ab initio* calculations enables the identification of MG compositions with promising fracture toughness *in silico*. This offers a resource- and time-efficient navigation through the vast composition space of MGs. Combining the beneficial properties - high yield strength and toughness – with the high ductility of crystals, a new material class called crystal-glass high-entropy nanocomposite was developed. It reveals enhanced yield strength and ductility compared to the fully crystalline reference alloys. With both the prediction of fracture toughness and tuneable yield strength in these crystal-glass composites, a toolbox for tailoring mechanical properties of crystal-glass HEA composites has become available.

References

1. Ashby, M.; Greer, A. L.: Scr. Mater. 54 (2006) 321.
2. Evertz, S.; Schnabel, V.; Köhler, M.; Kirchlechner, I.; Kontis, P.; Chen, Y.-T.; Soler, R.; Nagamani Jaya, B.; Kirchlechner, C.; Music, D.; Gault, B.; Schneider, J. M.; Raabe, D.; Dehm, G.: Front. Mater. 7 (2020) 89.
3. Schnabel, V.; Nagamani Jaya, B.; Köhler, M.; Music, D.; Kirchlechner, C., Dehm, G.; Raabe, D.; Schneider, J. M.: Sci. Rep. 6 (2016) 36556.
4. Evertz, S.; Kirchlechner, I.; Soler, R.; Kirchlechner; C.; Kontis, P.; Bednarcik, J.; Gault, B.; Dehm, G.; Raabe, D.; Schneider, J. M.: Mater. Des. 186 (2020) 108327.
5. Hoffmann, R.: Angew. Chem. Int. Edit. 26 (1987) 846.
6. Wu, G.; Balachandran, S.; Gault, B.; Xia, W.; Liu, C.; Rao, Z.; Wei, Y.; Liu, S.; Lu, J.; Herbig, M.; Lu, W.; Dehm, G.; Li, Z.; Raabe, D.: Adv. Mater. 32 (2020) 202619.

Software development

J. Janssen[1], O. Waseda[1], T. Hickel[1],
J. Mianroodi[2], M. Kühbach[2], N. Cautaerts[3], J. Neugebauer[1]

[1]CM, [2]MA, [3]SN

Recent developments in experimental techniques and computer simulations provided the basis to achieve many of the breakthroughs in understanding materials down to the atomic scale. While extremely powerful, these techniques produce more and more complex data, forcing all departments to develop advanced data management and analysis tools as well as investing into software engineering expertise. As a consequence, a MPIE software task force has been established (see p. 70), where software engineering and simulation software expertise developed e.g. in the CM department is utilized. Here, we have selected a few examples to demonstrate how these developments help to propel science both in experiment and theory.

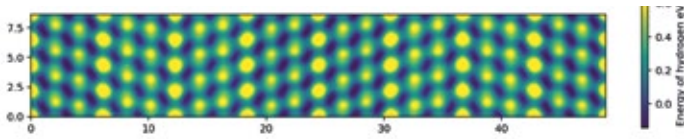

Fig. 1: *Free energy surface of H next to a Σ5 grain boundary in fcc Ni. The result has been achieved by developing a novel metadynamics schema with periodic collective coordinate within regular hackathons on hydrogen diffusion.*

An integrated development environment

On p. 72, pyiron has been introduced as an integrated platform for materials simulations and data management. At the same time, pyiron has also modified the culture of research in the CM department towards a stronger focus on software development. For the outer community, this is visible by a growing number of journal publications that are combined with executable code required for the physical analysis shown in the paper [1]. This code is provided within binder containers, such that the user can directly employ the simulations on cloud resources without the need of cumbersome installations on the local hardware. One example of this kind is the fully automated approach to calculate the melting temperature of elemental crystals [2]. The manuscript explains many of the technical challenges connected to the interface method, used for melting point calculations. The underlying complex simulation protocols are provided as pyiron notebooks, which allows a much more interactive access, reproduction and exploration of the underlying concepts than a written manuscript.

More significant for the research inside the CM department is, however, the cooperative development of new physical concepts in regular coding sessions. Several teams are currently meeting for several hours on a weekly basis, in order to test new physical ideas by directly implanting and executing them in pyiron notebooks. The physically intuitive structure of the pyiron environment allows such a research approach, without spending time on many command lines, taxonomy and syntax. For example, one group is exploring the physical nature of thermo desorption spectra (TDS) for hydrogen in metals. This involves the automatic detection of favourable sites for H incorporation into complex microstructure features (such as grain boundaries, Fig. 1), the analysis of possible jump processes between these sites and the evaluation of the H dynamics by kinetic Monte-Carlo simulations. Another group is connecting the workflows in pyiron notebooks with the semantic description of materials knowledge in ontologies, opening new routes of software development based on physical concepts rather than command lines.

Machine learning for solid mechanics

In the MA department, an artificial intelligence (AI)-based solution for predicting the stress field in inhomogeneous elasto-plastic materials was recently developed [3]. The training data for a convolutional neural network (CNN) were generated using DAMASK (Düsseldorf Advanced Material Simulation Kit) for modelling multi-physics crystal plasticity (see p. 73). Both, cases of materials with elastic and elasto-plastic behaviour, are considered in the training data. The trained CNN model is able to predict the von Mises stress fields (Fig. 2) orders of magnitude faster than conventional solvers. In the case of elasto-plastic material behaviour, conventional solvers rely on an iterative solution scheme for the nonlinear problem. The AI-based solver is able to predict the correct solution in one step forward evaluating of the CNN. This significantly reduces the implementation complexity and computation time. The augmentation of such a fast stress estimator with finite element-based solvers will open new avenues for the multi-scale simulation of materials.

Software tools for atom probe microscopists

In order to achieve scientific conclusions from atom probe tomography (APT), these data have to be processed into tomographic reconstructions, i.e. 3D models that specify the approximate original locations of the atoms in the field-evaporated specimen. Representing point clouds, these models are post-processed with methods from the field of spatial statistics, computational geometry, and AI resulting in quantified (micro)structural features or patterns that can be related to descriptors in physics-based models at the continuum scale such as dislocations, grain and phase boundaries, or precipitates.

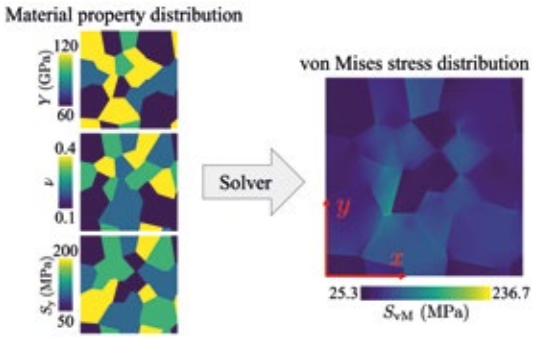

Fig. 2: *A typical mechanical solver relating the input material property distribution to an output von Mises stress distribution. For specific cases, the solver could be replaced by a convolutional neural network, which is orders of magnitude faster than the solver.*

It is important to quantify the eventual uncertainty and sensitivity of the descriptors as a function of the parameterization. To this end, though, the employed proprietary tools face substantial practical and methodological limitations with respect to the accessibility of intermediate (numerical and geometry) data and metadata they offer, the transparency of the algorithms, or the functionalities they provide to script and interface proprietary tools with open-source software of the atom probe community.

Involving APT domain specialists from the MA and computational materials scientists from the CM department, we implemented a toolbox of complementary open-source software for APT, which makes efficient algorithms of the spatial statistics, computational geometry, and crystallography community accessible to support scientists with quantifying the parameter sensitivity of APT-specific methods they use. Our tools exemplify how open-source software enables to build tools with programmatically customizable automation and high-throughput characterization capabilities, whose performance can be augmented by cluster computing. We show how to automate and make exactly reproducible the execution of microstructural feature characterization [4 - 6] for atom probe data.

Analysis tools for complex imaging and spectroscopy

One example of software development in the SN department is the creation of analysis workflows for data from transmission electron microscopes (TEM). Typically, most experimentalists use graphical user interface (GUI) based tools to process their data. Many of these tools are proprietary and licensed by the hardware manufacturer. The analysis options in this software are limited and rarely reproducible. In addition, with the advancement in detector technology and other instrumentation, the size and complexity of data is ever increasing. This calls for highly customizable analysis tools. This is also necessary for bridging the gap between the powerful machine learning and artificial intelligence libraries in the scientific python ecosystem and the workflow of the average experimentalist.

The experimental TEMMETA [7] library was built to address the most common analysis needs offered in software like ImageJ or Digital Micrograph, such as drawing line profiles, selecting subsets of the data, visualizing the data, and calculating strain fields from atomically resolved images. TEMMETA also has the feature of automatically storing information about each operation performed on data in a history attribute, thereby making it easier to reproduce the analysis. As development progressed, it became clear that the TEMMETA project had many of the same aims as the Hyperspy project, a library that has existed for a longer time and already has an established community of users and developers. Therefore, it was decided to integrate the novelties of the TEMMETA project into Hyperspy [8].

File parsers to a common representation are essential for bringing the full functionality of Hyperspy to any kind of microscopy data. The SN department is increasingly adopt-ing 4D-STEM as an advanced TEM based technique. It produces large and rich datasets of diffraction patterns collected on a grid of scan points. A typical workflow for these datasets relevant to metallurgists is analysing local crystal orientation via template matching. Existing proprietary software solutions could not handle the data from pixelated detectors, hence a custom built fast and scalable solution [9] was implemented in a package that builds on Hyperspy. This should make the transparent analysis of 4D-STEM datasets more accessible to researchers at the MPIE and all over the world.

References

1. https://pyiron.org/publications/
2. Zhu, L.-F.; Janssen, J.; Ishibashi, S.; Körmann, F.; Grabowski, B.; Neugebauer, J.: Comp. Mater. Sci. 187 (2021) 110065.
3. Mianroodi, J. R., H. Siboni, N. & Raabe, D.: npj Comput. Mater. 7 (2021) 99.
4. Kühbach, M.; Bajaj, P.; Zhao, H.; Celik, M.H.; Jägle, E.A.; Gault, B.: npj Comput. Mat. 7 (2021) 21.
5. Kühbach, M.; Kasemer, M.; Gault, B.; Breen, A.: J. Appl. Cryst. 54 (2021) 1490.
6. Kühbach, M.; London, A.J.; Wang, J.; Schreiber, D.K.; Mendez, M.F.; Ghamarian, I.; Bilal, H.; Ceguerra, A.V.: Microsc. Microanal. (2021). doi: 10.1017/S1431927621012241.
7. Cautaerts, N.; Janssen, J.: Zenodo: din14970/TEMMETA v0.0.6 (2021). doi.org/10.5281/zenodo.5205636.
8. de la Peña, F.; Prestat, E.; Fauske, V.T.; Burdet, P.; Furnival, T.; Jokubauskas, P.; Lähnemann, J.; Nord, M.; Ostasevicius, T.; MacArthur, K.E.; Johnstone, D.N.; Sarahan, M.; Taillon, J.; Aarholt, T.; pquinn-dls; Migunov, V.; Eljarrat, A.; Caron, J.; Poon, T.; Mazzucco, S.; Martineau, B.; actions-user; Somnath, S.; Slater, T.; Francis, C.; Tappy, N.; Walls, M.; Cautaerts, N.; Winkler, F.; Donval, G.: Zenodo: hyperspy v1.6.4 (2021). doi.org/10.5281/zenodo.5082777.
9. Cautaerts, N.; Crout, P.; Ånes, H. W.; Prestat, E.; Jeong, J.; Dehm, G.; Liebscher, C.H.: cond-mat arXiv:2111.07347

Integrated workflows for materials and data science

F. Roters[2], T. Hickel[1], L. Huber[1], J. Janssen[1], J. Neugebauer[1]

[1]CM, [2]MA

Integrated Computational Materials Engineering (ICME) is one of the emerging hot topics in Computational Materials Simulation during the last years. It aims at the integration of simulation tools at different length scales and along the processing chain to predict and optimize final component properties.

The realization of ICME concepts necessitates a workflow system, which on the one hand allows a flexible combination of different simulation tools and on the other hand enables the data exchange between these different tools. In addition, the workflow system should follow the FAIR (Findable, Accessible, Interoperable, and Re-usable) principle for sustainable materials development and offer a generic user interface to handle the different simulation tools.

pyiron (see p. 72, [1]) developed by the CM department is such a workflow platform. Originally designed for the integrated development and management of workflows on the atomistic scale, pyiron has been systematically extended during the last years to serve as a general workflow platform. In this process pyiron has been modularized. Besides the core module (pyiron_base) there exist three additional modules. pyiron_atomistic offers the original functionality on the atomistic scale; pyiron_continuum integrates continuum scale simulation tools like e.g. DAMASK (see p. 73, [2]) developed in the MA department; pyiron_experimental finally allows handling experimental data. The last module, which currently focuses on (scanning) transmission electron microscopy ((S)TEM) data, extends the application of ideas originally developed in computational materials simulation to experimental data and thus allows the creation of mixed experimental and simulation workflows following the FAIR principle.

In the early times of ICME coupling of different simulation tools was usually achieved on a one-to-one basis. This means the output of program 1 was converted to serve as input for program 2. One of the goals of the Federal Ministry of Education and Research (BMBF) initiative 'Material*Digital*' (see p. 80) is to overcome this direct coupling using ontology-based concepts. Here ontologies serve as an abstraction layer to define relations between data and concepts, which can be exploited for workflows and program interfaces. Such abstraction allows an exchange of different simulation tools that serve for a given workflow the same purpose. In this way workflows can be defined independently of the underlying simulation tools. Following a BMBF call in the framework of 'Material*Digital*', several academic projects have been initiated to define such workflows. The MPIE participates in the project 'Stahl*Digital*' together with the Fraunhofer Institute for Mechanics of Materials in Freiburg and the Institute for Applied Informatics (InfAI) at the University of Leipzig. The aim of 'Stahl*Digital*' is to define different workflows along the production chain and for the usage of steel sheets. These workflows will be based on ontologies, which describe both the material (two different steels) and the process chain (from hot rolling to crash performance) (Fig. 1).

Two different pre-existing workflow platforms will be extended for this purpose, namely SymPhoNy [3] developed by the Fraunhofer IWM and pyiron developed by the MPIE (Fig. 2). While SymPhoNy already allows the usage of ontologies for the workflow description, pyiron is currently extended accordingly.

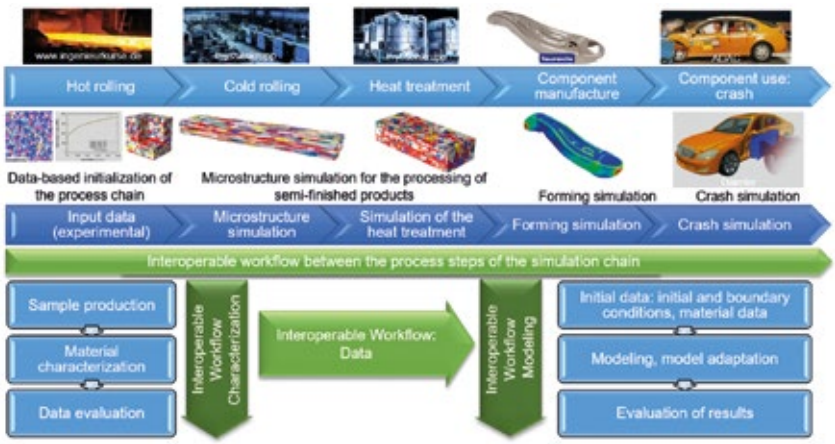

Fig. 1: *Workflows within the project 'StahlDigital'.*

In the following, we showcase two prototypical workflows as they can be easily defined and executed using pyiron:

1. A simulation workflow combining atomic scale simulation with continuum scale simulation.
2. A data-mining workflow evaluating simulation results.

pyiron workflows are developed as Jupyter notebooks [4], which ensures full reproducibility. In addi-

Fig. 2: *Workflow platforms used in 'StahlDigital'.*

tion, on top of the pyiron functionality any Python library can be easily included to perform special tasks.

Polycrystal elastic properties

Full field DAMASK simulations are well suited for the numerical homogenization of single crystal properties. However, often these single crystal properties are not known a priori. Here we are interested in the elastic properties of aluminium with different additions of magnesium. While the elastic constants of the pure materials are readily available in the literature, this is not true for the alloys. However, good interatomic potentials are available for the Al-Mg system. So, we can perform molecular dynamics simulations to determine the single crystal elastic constants. These are then passed into DAMASK, which is used to probe the elastic behaviour of a polycrystal under different loading conditions.

The full workflow consists of the following steps:

1. Minimize the structure for a pure Al cubic cell
2. Create special quasirandom structures (SQS) for different Mg concentrations
3. Select the interatomic potential
4. Run LAMMPS [5] simulations to determine elastic constants for each Mg concentration
5. Fit elastic constants as function of Mg concentrations (Fig. 3)
6. Create polycrystal volume element for DAMASK
7. Define loadcases for DAMASK
8. Inject elastic constants into DAMASK material file
9. Run DAMASK simulations
10. Determine homogenized elastic constants

Assessment of empirical potentials for fcc-Al

The idea behind this workflow is to compare various empirical potentials with respect to their performance for ground state properties of fcc-Al. The workflow consists of the following steps:

1. Get the list of available LAMMPS potentials
2. Create a Murnaghan job for each potential
3. Collect results in a table (Tab. 1)

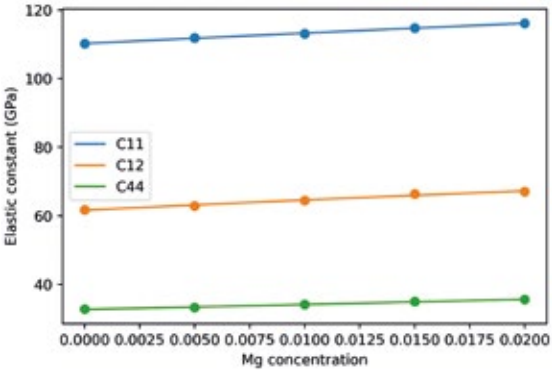

Fig. 3: *Single crystal elastic constants of an Al-Mg solid solution as function of Mg concentration.*

While both workflows seem to be not very complex, they potentially need to run a huge number of individual simulation jobs. In this case pyiron takes full care of distributing the individual jobs to computing nodes, collecting the results, and at the same time record important meta data about the jobs in a SQL data base.

	job_id	a_eq	bulk_modulus	potential
0	1	4.045415	89.015487	Al_Mg_Mendelev_eam
1	13	4.049946	80.836779	Zope_Ti_Al_2003_eam
2	25	4.049954	81.040445	Al_H_Ni_Angelo_eam
3	39	4.031246	78.213776	2000--Landa-A--Al-Pb--LAMMPS--ipr1

Tab. 1: *Screenshot of a table containing equilibrium lattice constant (a_eq) and bulk modulus of Al for different potentials.*

In summary, workflow management platforms like pyiron allow easy definition and execution of complex simulation projects following the FAIR principle. The connection to ontologies will make them even more flexible and easy to use.

References

1. Janssen, J.; Surendralal, S.; Lysogorskiy, Y.; Todorova, M.; Hickel, T.; Drautz, R.; Neugebauer, J.: Comput. Mater. Sci. 163 (2019) 24.
2. Roters, F.; Diehl, M.; Shanthraj, P.; Eisenlohr, P.; Reuber, C.; Wong, S.L.; Maiti, T.; Ebrahimi, A.; Hochrainer, T.; Fabritius, H.-O.; Nikolov, S.; Friák, M.; Fujitai, N.; Grilli, N.; Janssens, K.G.F.; Jia, N.; Kok, P.J.J.; Ma, D.; Meier, F.; Werner, E.; Stricker, M.; Weygand, D.; Raabe, D.: Comput. Mater. Sci. 158 (2019) 420.
3. https://www.simphony-project.eu/
4. https://jupyter.org/
5. Thompson, A. P.; Aktulga, H. M.; Berger, R.; Bolintineanu, D. S.; Brown, W. M.; Crozier, P. S.; in 't Veld, P. J.; Kohlmeyer, A.; Moore, S. G.; Nguyen, T. D.; Shan, V.; Stevens, M. J.; Tranchida, J.; Trott, C.; Plimpton, S. J.: Comp. Phys. Comm. 271 (2022) 10817.

Advancing atom probe towards true atomic-scale analytical tomography

B. Gault[1], C. Freysoldt[2], M. Kühbach[1], F. F. Morgado[1], L. Stevenson[1], D. Raabe[1]

[1]MA, [2]CM

Atom probe tomography (APT) is one of the MPIE's key experiments for understanding the interplay of chemical composition in very complex microstructures down to the level of individual atoms. In APT, a needle-shaped specimen (tip diameter ≈100nm) is prepared from the material of interest and subjected to a high voltage. Additional voltage or laser pulses trigger the evaporation of single ions from the tip. Accelerated by the voltage, the ions fly towards a position-sensitive channel-plate detector. The time-of-flight reveals the mass-to-charge ratio from which the elemental identity of each detected ion is deduced. Datasets of up to 10^9 ions are routinely acquired. From a data science perspective, APT datasets are a gold mine. APT data sets are huge, noisy, and full of more or less hidden patterns.

Data evaluation involves first building a virtual 3D point cloud in which the position of each ion prior to field evaporation is reconstructed. Beyond this first step, unbiased, quantitative analysis of the information encoded in the data remains challenging. A few examples: (1) elemental identities must be correctly assigned from a potentially complex mass spectrum that contains not only atomic ions, but also often metastable small molecular units; (2) the reconstructed positions are affected by uncertainties that blur out any underlying crystalline structure; (3) microstructural features must be extracted – what phases and crystal grains do exist? Where are their boundaries? How, where, and why do compositions change?

To standardize mass spectra analysis, in particular when it comes to identify the most likely ion when multiple candidates exist for the same mass-to-charge ratio, we demonstrated that deep neural networks can be trained to disentangle mass spectra [1]. This has the potential to enormously improve the reproducibility of mapping the mass-to-charge ratio to a set of chemical identity, compared to ranges defined by human inspection which could lead to composition significant variations between experts [2].

Current APT reconstructions are based on a geometrical projection algorithm from the detector position onto a spherical cap, which largely ignores the details of the underlying physics. In reality, trajectory aberrations occur due to the local environment prior to evaporation or mesoscopic field variations associated to surface roughness. The order of evaporation is not exclusively dictated by position, but possibly also by chemical identity and bonding environment, and affects the reconstruction process causing limitations of the spatial resolution. In order to quantify these effects, the group of C. Freysoldt has started systematic theoretical investigations of field evaporation mechanisms. In addition to confirming a material-dependent tendency for roll-over at steps on faceted surfaces, they were also able to demonstrate the crossover from a two-step to a one-step mechanism controlled by the field strength [3]. It was further shown that the surface mobility of hydrogen in presence of the field and the tendency for formation of H-containing ions depend primarily on the charge transfer of the adsorbed H.

Another topic of interest is to recover the crystalline lattice structure even when the positional uncertainty of the reconstruction prevents direct identification. The crystal orientation often gives rise to a systematic intensity pattern on the detector, which can be analysed by deep-learning [4]. Grain boundaries lead to a discontinuous pattern that can be identified and tracked automatically as the data set is sliced along the evaporation order, i.e. a proxy for the depth [5]. This approach allows for direct data filtering and quantification of chemical segregation to the boundary.

Crystallographic information of APT specimen is directly accessible by using field ion microscopy (FIM). FIM is a precursor technique in which an imaging gas is continuously ionized above the surface held below evaporation threshold. A new experimental approach was initiated at the MPIE in 2018 combining FIM with enabled mass spectrometry enabled by a correlative data analysis. We used this so-called analytical FIM to directly image solute segregation to dislocations [6] and to vacancies in Ni-based binary alloys [7]. These experimental investigations were paralleled by theoretical investigations to explain the chemical contrast observed in FIM by an electronic-structure effect.

At larger scales, the formation of phases with different chemical composition is of common interest. When formed at the nanoscale, there can be dozens or even hundreds of small precipitates in a single APT data set. While they are easily visualized by concentration iso-surfaces of key elements, this is impractical to perform quantitative analysis. Therefore, the Paraprobe toolset was developed [6]. It not only allows a scriptable, well-parallelized high-throughput analysis on high-performance computers without live interaction from a human scientist, but also provides standard aggregated (e.g. radial distribution functions) and iso-surface based segmentations in an open data format (based on HDF5) that can be further processed with standard data science and visualization tools.

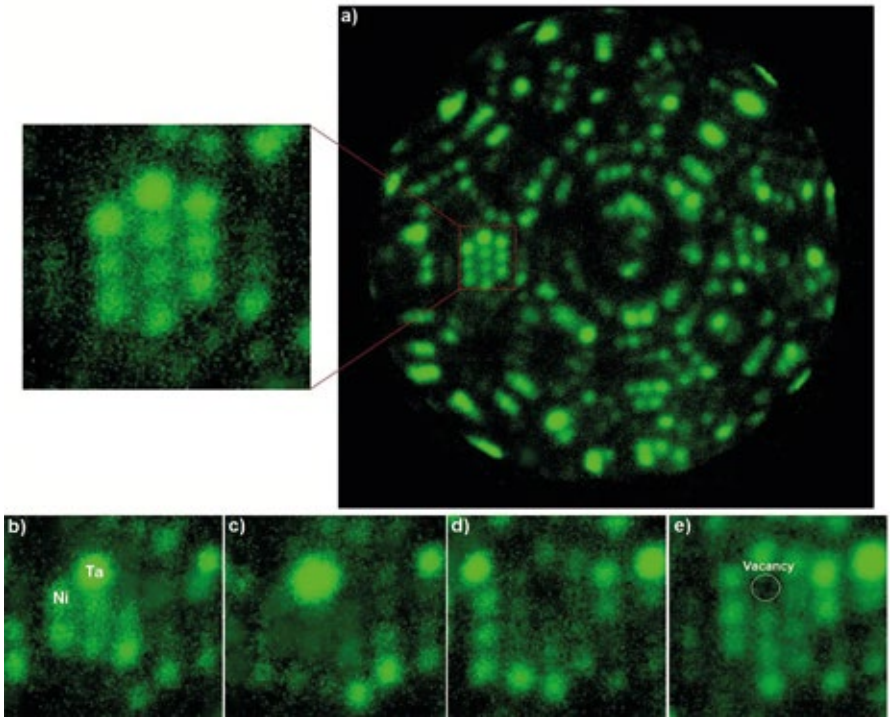

Fig. 1: *Field ion microscopy measurement of Ni-2 at.% Ta alloy. (a) Field ion micrograph zoomed on the (012) planes. (b)-(e) show consecutive atomic layers with identification of Ta, Ni atoms, and vacancy.*

More recently, we have explored alternative 3D phase segmentation algorithms. They start by mapping out the chemical composition of small voxels (10^2-10^3 atoms). Despite the large scatter, clustering in composition space allows to distinguish possible phases without prior information and derive classifiers from it. Next, a DBSCAN cluster analysis in the voxelized dataset labelled according to the composition classifier successfully provides a very fast and robust composition-based segmentation. These segments can then be further analysed based on their geometrical character (e.g. line-like, plate-like, ellipsoidal, etc.) and the application-oriented scientific questions.

References

1. Wei, Y.; Varanasi, R. S.; Schwarz, T.; Gomell, L.; Zhao, H.; Larson, D. J.; Sun, B.; Liu, G.; Chen, H.; Raabe, D.; Gault, B.: Patterns 2 (2021) 100192.
2. Haley, D.; Choi, P.; Raabe, D.: Ultramicroscopy 159 (2015) 338.
3. Ashton, M. W.; Mishra, A.; Neugebauer, J.; Freysoldt, C.: Phys. Rev. Lett. 124 (2020) 176801.
4. Wei, Y.; Gault, B.; Varanasi, R.S.; Raabe, D.; Herbig, N.; Breen, A.J.: Ultramicroscopy 194 (2018) 15.
5. Wei, Y.; Peng, Z.; Kühbach, M.; Breen, A. J.; Legros, M.; Larranaga, M.; Mompiou, F.; Gault, B.: PLoS One 19 (2019) 1.
6. Morgado, F. F.; Katnagallu, S.; Freysoldt, C.; Klaes, B.; Vurpillot, F.; Neugebauer, J.; Raabe, D.; Neumeier, S.; Gault, B.; Stephenson, L.: Scr. Mater. 203 (2021) 114036.
7. Kühbach, M. T.; Bajaj, P.; Zhao, H.; Çelik, M. H.; Jägle, E. A.; Gault, B.: npj Comp. Mat. 7 (2021) 21.

Big data and machine learning in electron microscopy

N. Cautaerts[1], C. Freysoldt[2], C. Liebscher[1], G. Dehm[1], J. Neugebauer[2]

[1]SN, [2]CM

Data-rich experiments such as scanning transmission electron microscopy (STEM) provide large amounts of multi-dimensional raw data that encodes, via correlations or hierarchical patterns, much of the underlying materials physics. With modern instrumentation, data generation tends to be faster than human analysis, and the full information content is rarely extracted. We therefore work on automatizing these processes as well as on applying data-centric methods to unravel hidden patterns. At the same time, we aim at exploiting the insights from information extraction to direct the data acquisition to the most relevant aspects, and thereby avoid collecting huge amounts of redundant data.

possible by commercial software. The development will also enable an on-the-fly data analysis in the future by utilizing GPU-accelerated processing.

STEM is also very powerful at revealing the atomic structure even of complex materials. Since under high-angle angular dark field (HAADF) conditions the collected electrons predominantly undergo scattering near the atomic nucleus, the image or atomic column intensity is proportional to their mean atomic number. When aligning the specimen along specific crystallographic directions it is possible to image a 2D projection of the crystal lattice, but also lattice defects such as phase or grain boundaries. Typically, the

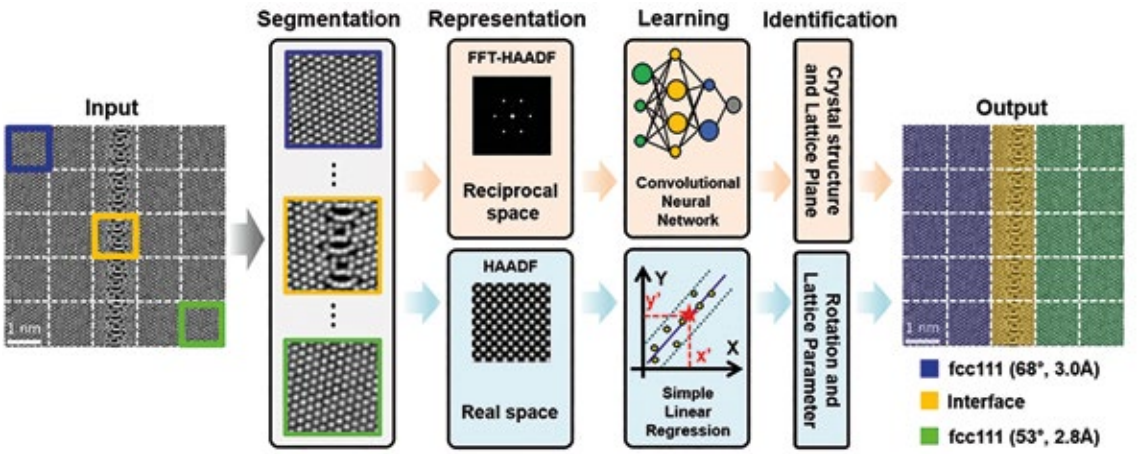

Fig. 1: *Schematic workflow of the classification procedure for experimental STEM images. Here, the input HAADF-STEM image contains two different crystalline regions and one grain boundary. The image is divided into 5 × 5 windows. Three different patches are indicated in the input image: patch (1,1) by the blue, patch (3,3) orange and window (5,5) by the green square. The classification map identifies both blue and green patches as fcc {111}. The orange patches correspond to the grain boundary region, respectively. Image by B.Yeo, L. Ghiringhell, Fritz Haber Institute Berlin.*

The advent of fast electron detectors enabled the collection of full diffraction patterns in each probe-position, while scanning the beam across the electron transparent sample. These 4D-STEM datasets contain rich information on local lattice orientation, symmetry and strain [2]. However, handling and analysing these large-scale datasets, which are typically >10 GB in size requires sophisticated data management infrastructure and algorithms. We are currently developing a flexible and open-source approach within the Python-based pyXem package to index the phase and crystal orientation in scanning nano-beam diffraction datasets [3], which is until now only

detection of nanoscale domains and interfaces in complex materials is executed by hand in an iterative manner relying on deep domain knowledge. We have developed a robust symmetry-based segmentation algorithm that solely considers lattice symmetries and hence does not require specific prior insights into the observed structures [4]. It is based on the idea that local symmetries create a self-similarity of the image that can be quantified via Pearson correlation coefficients of image patches. This quantification is very noise-tolerant, in particular if large patches are chosen. By collecting these values for a number of candidate symmetries (100-1000), a characteristic fingerprint of the

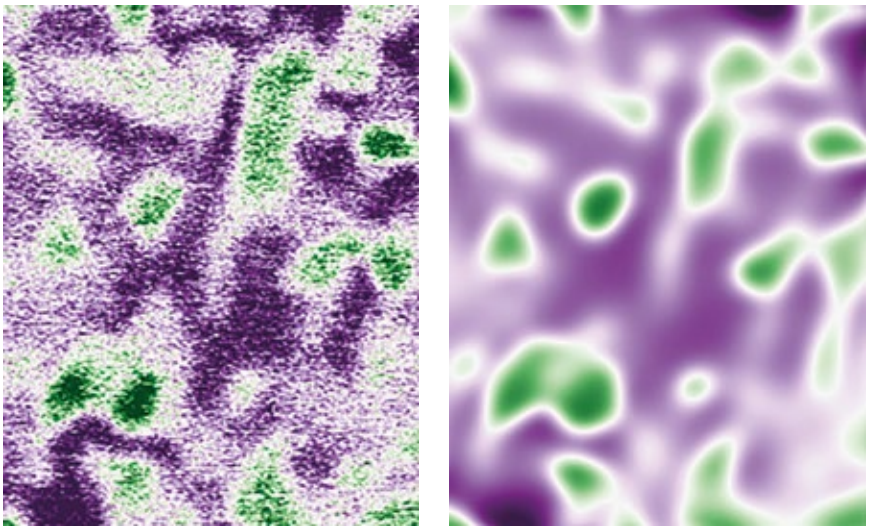

Fig. 2: *Left: Snapshot from in situ STEM-HAADF imaging of the dealloying of a TaTiZrHf high-entropy alloy. Right: snapshot from the phase-field informed neural network representation.*

local crystallographic patterns can be extracted that does not rely on identifying individual atomic columns. These fingerprints can then be taken from various places in the image and allow to filter out recurring patterns by principal component analysis and a subsequent clustering. From this abstract representation, the fingerprints can be classified, yielding a segmentation of the original image without prior training on expected phases. It therefore also works for complex atomic arrangements, e.g., topologically close-packed phases.

To classify and quantify regions autonomously in atomic resolution STEM images, we are currently developing a supervised deep learning approach in a BiGmax collaboration with L. M. Ghiringhelli (Fritz Haber Institute Berlin). The underlying backbone of the classification is a convolutional neural network (CNN), which is trained on simulated STEM images represented by their Fourier transforms. Here, we are considering the basic classes of face-centred cubic (fcc), body-centred cubic (bcc) and hexagonal close packed (hcp) crystal structure for low index orientations. To include uncertainty predictions in the classification, we use Bayesian learning for being able to identify crystal structures or defective regions that the CNN was not trained on. In a second step, the local crystal rotation and lattice parameters are determined by linear regression analysis, which is based on analysing the real space lattice symmetries. In the classification procedure, an experimental image is then subdivided in image patches and the neural network learns which training class is present, its local lattice rotation and lattice constants as shown in Fig. 1. This development is now extended towards a real-space classification procedure also taking into consideration the atomic column intensities to determine local compositional variations and defect structures.

At larger length scales, HAADF allows to monitor phase transformations at elevated temperatures. Such time-resolved measurements yield multiple frames that can be visualized as video sequences. Yet, the quantification of the phase transformation kinetics requires additional processing and simplification of the raw data. In particular, the quantification of intensity gradients is severely hindered by the presence of shot noise. For this, we have explored the use of physics-informed neural networks to map the noisy images to a phase-field model with known analytic structure. The basic idea is to train a smooth machine-learning model to reproduce the measured data, while at the same time requiring it to comply with the phase-field equations, using model parameters that are trained on the fly. It turns out that such an approach is very efficient to obtain a coarse-grained simplified representation of the underlying data. In addition, the neural network representation and the phase-field equations filter out high-frequency noise in space and time without blurring interfaces (Fig. 2). These initial findings have triggered a new collaboration with the MPI for Dynamics of Complex Technical Systems, funded by the BiGmax network (see p. 82).

References

1. https://nomad-coe.eu/home-coe
2. Cautaerts, N.; Rauch, E. F.; Jeong, J.; Dehm, G.; Liebscher, C. H.: Scr. Mater. 201 (2021) 113930.
3. Cautaerts, N.; Crout, P.; Ånes, H.W.; Prestat, E.; Jeong, J.; Dehm, G.; Liebscher, C.H.; arXiv:2111.07347 (2021).
4. Wang, N.; Freysoldt, C.; Zhang, S.; Liebscher, C. H.; Neugebauer, J.: Microsc. Microanal. 27 (2021) 1454.

A microscopic view of electrochemical interfaces: *ab initio* molecular dynamics at controlled electrode potential

S. Wippermann[1], F. Deißenbeck[1], S. Surendralal[2], M. Todorova[2], J. Neugebauer[2]

[1]GO, [2]CM

Ever since the discovery of electricity, chemical reactions occurring at the interface between a solid electrode and an aqueous solution have aroused great scientific interest, not least by the opportunity to influence and control the reactions by applying a voltage across the interface. Our current textbook knowledge is mostly based on mesoscopic concepts, i.e. effective models with empirical parameters, or focuses on individual reactions decoupled from the environment, presenting therefore a serious obstacle for predicting what happens at a particular interface under particular conditions. In particular the current transition of the world to a more sustainable future requires a truly microscopic understanding of the electrochemical interface and double-layer by incorporating insights from the atomistic and electronic scale. Methodological breakthroughs at the MPIE during the last few years in both *ab initio* theory and experiments now allow us to directly characterise the structure and dynamics of electrified solid/liquid interfaces with atomic resolution at short timescales.

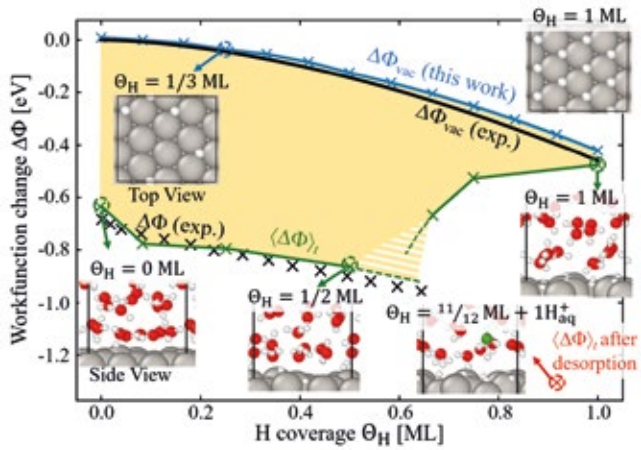

Fig. 1: *Work function (blue) and time-averaged electrode potential (green) as function of H coverage on Pt(111). For comparison, the experimentally measured work function (black line) and electrode potential (black crosses) are included. The critical H concentration is predicted to lie within the yellow hashed area, as as indicated by the extrapolated dashed green lines. Representative surface and interface structures at selected coverages are shown as insets.*

While the relation between the electrode potential and adsorbate coverage is accessible by experimental techniques such as cyclic voltammetry, understanding how exactly adsorbate interfacial structures influence the measured electrode potential evades direct experimental access. Consider the H-covered Pt(111)/H_2O interface, one of the best investigated "model" electrochemical systems due to its excellent catalytic performance for the hydrogen evolution reaction (HER). The onset of the HER coincides with the presence of a puzzling upper limit to the H adsorption at ≈ 0.66 ML (monolayer). A possible explanation is that water is not just a spectator but actively controls adsorption and chemical reactions at the metal-water interface.

To explore the impact of water on surface adsorption and the electrode potential, we perform a systematic comparison of the work function (electrode potential) of H-covered Pt(111) in vacuum (an aqueous environment) for coverages up to 1 monolayer employing density functional theory calculations [1]. Our calculations show an excellent agreement with experiment (Fig. 1) and allow us to directly explore how screening is realised at electrochemical interfaces. For the pristine Pt(111) interface we observe a large shift of the electrode potential with respect to the vacuum work function. This shift is caused by chemisorbed water molecules, which screen the interfacial dipole through charge transfer to the surface. Besides the Pt atom directly bonded to the H_2O molecule, this transfer involves several Pt atoms in its vicinity, effectively blocking neighbouring adsorption sites. Therefore, with the onset of H adsorption a competition arises between the water and hydrogen for the Pt atoms available for charge transfer. Increasing H coverage causes a monotonous loss of chemisorbed water, which is partially compensated by the charge transfer, due to H adsorption, but causes an increasing potential drop. Beyond a critical coverage of $\theta_H \approx 0.66$ ML this mechanism breaks down, because the increasing potential drop at the interface can no longer be screened by direct adsorption. Instead, the system responds by creating a large interfacial dipole through an electrochemical desorption reaction. This is achieved by deprotonation, where an H^+ ion forms in the vicinity of the interface, leaving its corresponding electron at the Pt(111) surface. The H^+ ion formation provides the necessary precursor state to enable the HER. Our findings directly link the existence of the breakdown in the electrode potential and the experimentally observed critical H adsorbate concentration at which hydrogen evolution starts.

In order to study electrochemical reactions -- such as, e.g., the HER -- in *ab initio* molecular dynamics simulations with explicit water, we build on our first principles electrochemical cell set-up introduced in the last reporting period [2], which allows us to actively control the local

surface charge in order to drive the system towards the targeted value for the electrode potential. While the surface charge is constant in the thermodynamic limit, the microscopic size of the interfacial region targeted by our simulations requires treating the local surface charge as a thermodynamic degree of freedom.

Changing the potential of a capacitive system, e.g. by controlling the surface charge in our electrochemical cell, is, however, a dissipative process. Energy is drained from molecular motions that are associated with a change in the electric dipole moment. This energy lost to potential control has to be compensated by corresponding thermal potential fluctuations, that exactly return the removed energy, on average, to those degrees of freedom where it was taken from. The physical system realises this by coupling to a fluctuating electric field created by temperature dependent charge fluctuations caused by the thermal motion of the electrons and ions.

To mimic this behaviour, our potentiostat must apply an electric field with an explicit finite temperature and hence become a thermopotentiostat. This can be achieved by adapting the fluctuation-dissipation theorem (FDT) to atoms exposed to an electric field. To this end, we used the FDT and the theory of stochastic differential equations in conjunction with Itō calculus. The derived direct expression for the electrode charge [2] is general, independent of the specific boundary conditions of the set-up and can be straightforwardly implemented in any molecular dynamics code, whether empirical or first principles. In fact, we have already implemented the thermopotentiostat in the VASP and lammps simulation packages (Fig. 2).

To demonstrate the performance of our thermopotentiostat approach we considered a topic that currently attracts a lot of attention. Recent experiments demonstrated that the presence of a solid-water interface appears to dramatically reduce the dielectric response of water from a highly polarizable medium down to a response that is close to the vacuum dielectric constant. We found that interfacial water forms stratified structures with a strongly modified dielectric behaviour, showing characteristic oscillations in the dielectric function close to interfaces and overscreening effects reminiscent of Friedel oscillations (see p. 125). As a consequence of the interfacial water's dielectric response, the potential drop between the electrode and the bulk water region occurs to a large degree directly at the interface, cf. blue line in Fig. 2. It is exactly within this region of interfacial water with modified properties where electrochemical reactions proceed.

Pioneered by Gerischer already 60 years ago, single-crystalline and atomically flat semiconductor surfaces interfaced with liquid water were popular model systems used to explore elementary electrochemical processes. The reaction mechanisms and their intermediate steps have been speculated about based on indirect evidence obtained from cyclic voltammetry and spectro-electrochemisty. We can now directly probe and predict the precise mechanistic details from first principles using our thermopotentiostat simulations. A corresponding snapshot for Ge(100) surfaces is shown in Fig. 2. Exceeding a potential drop of $\Phi_0 > 2$ V under anodic polarization, we observe that the reorientation of interfacial water is insufficient to screen the applied electric field. Instead, the interfacial dipole is screened by water dissociation, where H^+ is released into the solvent and OH^- groups adsorb on the surface (marked in orange). The subsequent discharge of the hydroxyl groups by the thermopotentiostat enables sustained reaction conditions for a continuous water splitting and electrooxidation of the surface.

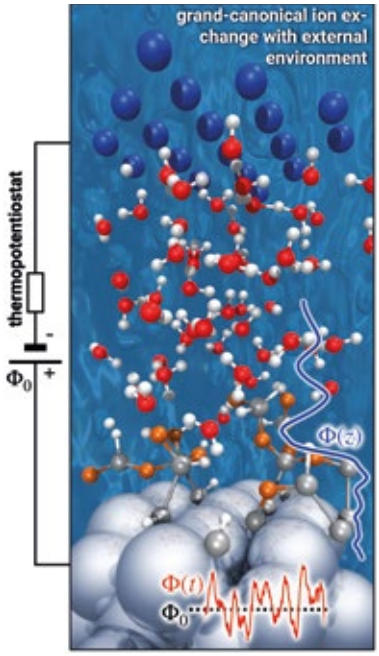

Fig. 2: *Electrochemical cell consisting of a Ge(100):H working electrode in contact with liquid water and a computational counter electrode (blue balls). Surface-adsorbed oxygen is marked in orange. In order to drive the system to the desired potential drop Φ_0 our thermopotentiostat algorithm controls the charge transferred between the two electrodes. Due to the microscopic size of the interfacial region targeted by our simulations, both the surface charge and the instantaneous potential $\Phi(t)$ are not constant but instead must be allowed to fluctuate. The time averaged potential Φ_z perpendicular to the interface is shown in blue.*

These examples demonstrate how our continuous methodological advances help to reveal the elementary processes at electrified solid/liquid interfaces, enables us to show how idealised textbook models can be actually observed and revised, and thus achieve a truly microscopic understanding at the atomistic and electronic scales.

References

1. Surendralal, S.; Todorova, M.; Neugebauer, J.: Phys. Rev. Lett. 126 (2021) 166802.
2. Surendralal, S.: Todorova, M.; Neugebauer, J.: Phys. Rev. Lett. 120 (2018) 246801.
3. Deißenbeck, F.; Freysoldt, C.; Todorova, M.; Neugebauer, J.; Wippermann, S.: Phys. Rev. Lett. 126 (2021) 136803.